

Evaporation and absorption of inkjet printed droplets with surfactants

Citation for published version (APA):

van Gaalen, R. T. (2022). *Evaporation and absorption of inkjet printed droplets with surfactants*. [Phd Thesis 1 (Research TU/e / Graduation TU/e), Mechanical Engineering]. Eindhoven University of Technology.

Document status and date:

Published: 27/01/2022

Document Version:

Publisher's PDF, also known as Version of Record (includes final page, issue and volume numbers)

Please check the document version of this publication:

- A submitted manuscript is the version of the article upon submission and before peer-review. There can be important differences between the submitted version and the official published version of record. People interested in the research are advised to contact the author for the final version of the publication, or visit the DOI to the publisher's website.
- The final author version and the galley proof are versions of the publication after peer review.
- The final published version features the final layout of the paper including the volume, issue and page numbers.

[Link to publication](#)

General rights

Copyright and moral rights for the publications made accessible in the public portal are retained by the authors and/or other copyright owners and it is a condition of accessing publications that users recognise and abide by the legal requirements associated with these rights.

- Users may download and print one copy of any publication from the public portal for the purpose of private study or research.
- You may not further distribute the material or use it for any profit-making activity or commercial gain
- You may freely distribute the URL identifying the publication in the public portal.

If the publication is distributed under the terms of Article 25fa of the Dutch Copyright Act, indicated by the "Taverne" license above, please follow below link for the End User Agreement:

www.tue.nl/taverne

Take down policy

If you believe that this document breaches copyright please contact us at:

openaccess@tue.nl

providing details and we will investigate your claim.

Evaporation and absorption of inkjet printed droplets with surfactants

Evaporation and absorption of inkjet printed droplets with surfactants
by R.T. van Gaalen
Technische Universiteit Eindhoven, 2022

Typeset: \LaTeX
Cover design: Egbert de Beer
Printed by: Gildeprint – Enschede

A catalogue record is available from the Eindhoven University of Technology Library.

ISBN: 978-90-386-5385-3.

Copyright ©2021 by R.T. van Gaalen. All rights reserved.



This work is part of an Industrial Partnership Programme of the Foundation for Fundamental Research on Matter (FOM), which is part of the Netherlands Organisation for Scientific Research (NWO). This research programme is cofinanced by Canon Production Printing, University of Twente, Eindhoven University of Technology, and the “Topconsortia voor Kennis en Innovatie (TKI)” allowance from the Ministry of Economic Affairs.

Evaporation and absorption of inkjet printed droplets with surfactants

PROEFSCHRIFT

ter verkrijging van de graad van doctor aan de Technische Universiteit Eindhoven, op gezag van de rector magnificus prof.dr.ir. F.P.T. Baaijens, voor een commissie aangewezen door het College voor Promoties, in het openbaar te verdedigen op donderdag 27 januari 2022 om 11:00

door

Ruben Thomas van Gaalen

geboren te Bussum

Dit proefschrift is goedgekeurd door de promotoren en de samenstelling van de promotiecommissie is als volgt:

voorzitter: prof.dr.ir. D.M.J. Smeulders
1e promotor: prof.dr. J.G.M. Kuerten
2e promotor: prof.dr.ir. H.M.A. Wijshoff
leden: prof.dr. F. Toschi
prof.dr. J.H. Snoeijer (Universiteit Twente)
prof.dr. D. Vollmer (Max Planck Institute for Polymer Research)
prof.dr.ir. E.H. van Brummelen
adviseur: dr. C. Diddens

Het onderzoek dat in dit proefschrift wordt beschreven is uitgevoerd in overeenstemming met de TU/e Gedragscode Wetenschapsbeoefening.

Summary

Inkjet printing involves several key challenges. An important aspect is the flow dynamics after deposition of an ink droplet onto a substrate. The drop will evaporate and – if the substrate is porous – absorb at the same time. Typically, this process also involves additional components like surfactants. Surfactants are molecules that adsorb onto interfaces, thereby reducing the local surface tension, which has significant ramifications for the droplet dynamics. The reduced interfacial tension can result in rich behavior, including circulatory flow patterns and accelerated absorption dynamics. It is therefore of no surprise that there are still many open questions regarding the mechanisms of surfactants in sessile droplets. In this thesis an attempt is made to answer some of these questions in a satisfactory way.

In order to gain insight into the dynamics of surfactant-laden droplets, a numerical model is employed. This model is based on lubrication theory, meaning that the assumption is made that the contact radius of the droplet has a significantly larger magnitude than the height. By making this assumption it becomes possible to describe the droplet evolution only in terms of a height profile, making lubrication theory an efficient and transparent modeling technique. With this model as a basis, several extensions are introduced of which the surfactant transport is the most prominent one. This transport is governed by several convection-diffusion-adsorption equations both at the interfaces and in the bulk of the fluid. Furthermore, absorption into the porous medium is modeled with Darcy's law and the evaporation field is calculated using an analytical solution.

First, the contact line dynamics of an evaporating droplet with insoluble surfactants are examined using two different methods: a precursor film model and a slip model. For pure droplets these models are shown to perform comparably with respect to literature data, but when surfactants are involved the precursor film model results in several problems, because it does not inherently distinguish between the droplet and the film. Therefore, surfactants can freely flow in and out of the precursor film, which is an issue that requires to be solved before this model can be used in the current context. The slip model, on the other hand, reveals that even if there is no explicit pinning force present, surfactants can still keep the contact line fixed. This is caused by the reduction in space on the interface during evaporation, which increases the surfactant concentration and decreases the surface tension accordingly. The result is a lower equilibrium contact angle, which slows down the contact line retraction as if actually pinning it.

Furthermore, the various regimes of the fluid flow in evaporating droplets with soluble surfactants are mapped. It is shown that with the inclusion of surfactants typically one out of two flow patterns exists: a circulatory flow, where there is the combination of an outward capillary flow in the bulk of the droplet and an inward Marangoni flow close to the interface (called the 'Marangoni regime'), and a purely outward flow, where there is only a capillary flow towards the contact line, while the flow at the interface nearly halts due to Marangoni effects (called the 'coffee-ring regime'). Surfactant properties that are found to typically promote the Marangoni regime over the coffee ring regime are fast sorption kinetics and high solubility, while for the droplet

conditions fast evaporation is a promoting factor.

Also, the absorption of droplets in porous media is modeled and the effects of surfactants on this process are analyzed. It is found that for pure droplets with both pinned and moving contact lines the penetration depth, being the deepest point where fluid has absorbed, evolves in a similar manner. However, for a moving contact line case the absorption process is much slower than for a pinned case, because the contact area shrinks over time. This also results in the wetted region having a more pointed shape after absorption in the moving contact line case. It is shown that surfactants can accelerate the absorption process, but only if the adsorption kinetics are not too fast compared to the absorption time scale. Otherwise, all surfactant adsorbs onto the pore walls before reaching the wetting front.

Lastly, a start is made with developing a model that describes particle transport during evaporation, both for small and large concentrations. For small concentrations, the colloidal dynamics can be described by a ‘tracer particle model’, where the particles are considered to be massless and passive. For the tracer particle model it is shown that the lubrication model does not describe the velocity field in the contact line region accurately. If a circulatory flow is present, particles still accumulate at the contact line as if there is only a capillary flow. Possible solutions to this issue lie in the introduction of correction terms that are otherwise neglected in lubrication theory or to use an altogether different model that fully incorporates the Navier-Stokes equation for viscous flows.

At higher concentrations, the particle dynamics can be described by a ‘two-phase model’, where the particles are considered as a distinct phase that affects the fluid dynamics. It is found that any two-phase particle model for evaporating droplets requires to take into account the maximum packing density of particles, since this concentration is already reached in the initial stages of the drying process. By introducing several ad-hoc corrections when the maximum packing density is reached, it is shown that reasonable results can be obtained. However, in order to make the model viable it also needs to take into account the underlying physics, which can possibly be achieved by modeling the transition from a Stokes regime flow to a Darcy regime flow at high particle fractions.

Contents

Summary	i
1. Introduction	1
2. Numerical model	5
2.1. Droplet evolution	5
2.2. Absorption model	9
2.3. Interfacial surfactant concentration	11
2.4. Bulk surfactant concentration	13
2.5. Pore surfactant concentration	14
2.6. Evaporation model	15
2.7. Adsorption model	16
2.8. Solute transport	18
2.9. Solution procedure	20
3. Evaporation of droplets with insoluble surfactants	23
3.1. Introduction	23
3.2. Mathematical model	25
3.3. Results and discussion	29
3.4. Conclusion	36
4. Flow in evaporating droplets with soluble surfactants	39
4.1. Introduction	39
4.2. Mathematical model	40
4.3. Results and discussion	47
4.4. Conclusion	56
5. Absorption of droplets with soluble surfactants	59
5.1. Introduction	59
5.2. Mathematical model	60
5.3. Results and discussion	66
5.4. Conclusion	73
6. Particle dynamics in evaporating droplets with soluble surfactants	77
6.1. Introduction	77
6.2. Mathematical model	78
6.3. Results and discussion	83
6.4. Conclusion	92
7. Conclusions	95
A. Input parameters	99
A.1. Input values in Chapter 4	99
A.2. Input values in Chapter 5	100
References	103

Acknowledgements	117
Curriculum Vitae	119
List of Publications & Conference contributions	121

1. Introduction

Inkjet printing is a technology with a wide range of applications. It can, amongst other things, be employed for the printing of graphics and text on paper, polymers, textile and other materials, but also for more specific purposes such as the manufacturing of microarray slides for medical applications and the printing of electronics. Consequently, it is unsurprising that the estimated worldwide value of the commercial printing market was about 420 billion USD in 2020 and is expected to grow in the coming years [76]. Furthermore, also in the scientific community inkjet printing is a growing topic in itself. For example, in the last two editions of the prominent international conference ‘Droplets’ (2019 and 2021) separate parallel sessions were scheduled, purely to discuss inkjet printing as a technology.

In the context of this broad scientific and industrial interest, the program ‘Fundamentals of Inkjet Printing’ (FIP), of which this thesis is a result, was set up. In a cooperation between an industrial partner (Canon Production Printing Netherlands b.v.), a governmental partner (Nederlandse Organisatie voor Wetenschappelijk Onderzoek) and two academic partners (Eindhoven University of Technology and University of Twente), a total number of twelve PhD tracks were defined and funded. As illustrated in Figure 1.1, each of these twelve projects considers a different aspect of the inkjet printing process, including acoustic jetting, satellite drop formation and drop coalescence.

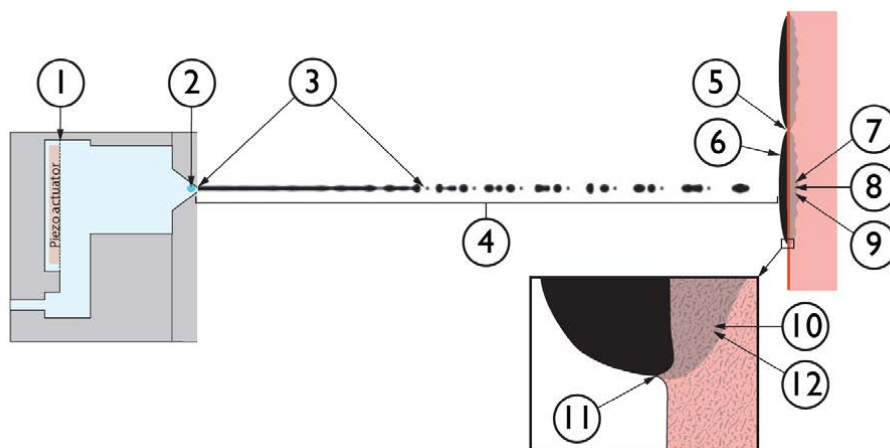


Figure 1.1.: Fundamentals of Inkjet Printing program (FIP) : This project is #10 in this large PhD program

The project of which this thesis is a result is number 10 in this program and it focuses on the evaporation and absorption of sessile droplets in the presence of surfactants. After an ink droplet has been jetted onto the substrate, it will evaporate and absorb into the paper over time, leaving behind a residue of the particles which are one of the constituents of ink. Often surfactants are added as a component to ink droplets in order to influence their dynamical behavior, such as the internal flow during evaporation

(e.g. Marangoni circulation [73]) and the absorption rate [169]. Because the exact mechanisms of surfactants in inkjet printing are still unclear, this project was set up as a method of increasing our understanding of this topic using numerical models.

The model that is used in this work employs lubrication theory, which is a way to describe the dynamics of a thin liquid film (including relatively flat droplets). The method hinges on the assumption that the typical height of the considered film is small compared to its typical width. Due to that assumption several terms in the Navier-Stokes equation can be neglected, resulting in a much simpler equation. This allows for a more transparent and computationally efficient model compared to more standard models employed in computational fluid dynamics.

Employing the lubrication model, the dynamics of surfactant-laden droplets under evaporation and absorption are to be investigated. The aspects that are examined in this thesis, are given in the following section.

Goals and Outline

The goals of this thesis involve the investigation of several aspects of the fluid dynamics of sessile droplets in the presence of surfactants.

First of all, it is of relevance to understand the contact line dynamics of an evaporating droplet when surfactants cover the interface. Besides the behavior if the contact line is pinned, it is also important to know how it moves in the presence of surfactants. Will the contact angle change over time and how does it compare to the dynamics of a pure droplet? Furthermore, what models can best be used to describe the motion of the contact line?

Besides that, also the internal flow dynamics in the droplet are of interest, one reason being that the flow determines the final deposition pattern of the ink particles. What kind of flow regimes can be distinguished? And how do surfactant properties, such as solubility, adsorption kinetics and diffusion rate, determine which flow pattern is dominant?

Regarding absorption due to capillary action, it is relevant to understand how the wetted region in the porous medium evolves, both with and without surfactants. The surfactant monomers will adsorb onto the pore walls and it is therefore important to consider how this would affect the capillary suction. How much surfactant will adsorb close to the wetting front, thereby changing the suction? What kind of effect will this have on the absorption dynamics and rate?

The last goal of this project is to investigate particle dynamics during drop evaporation. One of the key factors in inkjet printing is the final deposition pattern of the ink particles and therefore it is important to analyze how particles flow during evaporation, both with and without surfactants. Where do particles accumulate if surfactants are added, if anywhere? What effect do particles have on the fluid flow itself?

The outline of this thesis is the following. Chapter 2 treats the models and numerical procedures that are used to investigate droplet behavior. In Chapter 3 the effects of

insoluble surfactants on the contact line dynamics of evaporating droplets are considered and in Chapter 4 the influence of soluble surfactants on the internal fluid flow. In Chapter 5 it is analyzed how the absorption behavior of droplets changes when surfactants are involved and in Chapter 6 an attempt is made to create an accurate model for particle dynamics. In Chapter 7 the main conclusions of this thesis are summarized and recommendations are made for future research.

Reader guide

This thesis is written in such a way that each chapter (with the exception of the Introduction and the Conclusion) can be read independently. Therefore, however, some parts tend to repeat content that was already outlined before. If the reader wishes to read the thesis in its entirety, it is recommended to skip the second sections of Chapters 3 to 6, each entitled ‘Mathematical model’. This material is also considered in Chapter 2. Employing this strategy will likely save some of the reader’s valuable time.

2. Numerical model

This chapter introduces the relevant equations and their derivations. It is shown how under given assumptions the governing differential equations can be derived and how they are solved numerically.

In Section 2.1 the evolution equation of the droplet profile is derived both with and without a slipping contact line. Extra attention is given to the disjoining pressure, which is a pressure term that becomes relevant in the case that a precursor film is covering the substrate around the droplet. Furthermore, in Section 2.2 a derivation is made for a droplet absorption model, starting from Darcy's law. This is of relevance if the substrate is porous (see Chapter 5).

In Section 2.3 the transport equation of the surfactant at the liquid-air interface is derived and in Section 2.4 the transport equation of the surfactant in the bulk of the droplet, either in the form of monomers or as micelles. Similarly, in Section 2.5, a transport equation is given for the surfactant transport in the porous medium.

In Section 2.6 the evaporation model is explained and an analytical solution is given for the case of a spherical cap and in Section 2.7 the sorption models of the surfactant are given. Furthermore, in Section 2.8 the two solute transport models are covered and in Section 2.9 the numerical solution procedure is outlined.

2.1. Droplet evolution

In this section the evolution equation for the drop profile is derived (both with and without slip) and the relevant pressure terms are considered.

2.1.1. Basic derivation

The flow in the droplet is governed by the three-dimensional Navier-Stokes equation and the continuity equation for an incompressible Newtonian fluid with constant viscosity given, respectively, by

$$\rho \left(\frac{\partial \vec{U}}{\partial t} + \vec{U} \cdot \nabla \vec{U} \right) = -\nabla p + \mu \nabla^2 \vec{U} + \rho \vec{g}, \quad (2.1)$$

$$\nabla \cdot \vec{U} = 0. \quad (2.2)$$

Here, ρ is the mass density of the fluid, \vec{U} the fluid velocity vector, p the pressure, μ the dynamic viscosity and \vec{g} the gravitational acceleration vector.

The droplet has a typical height H , contact radius R and contact angle θ . Only small aspect ratios are considered, meaning $\epsilon = H/R \ll 1$. A small Reynolds number is assumed and also a small Bond number, $Bo = \frac{\rho g H^2}{\sigma_{sl}} \ll 1$, with g the magnitude of the

gravity and σ_{sl} the liquid-gas surface tension. The latter assumption means that gravity does not affect the shape of the droplet. A cylindrical coordinate system (r, α, z) is used, with the assumptions of no swirl (angular velocity $U_\alpha = 0$) and axisymmetry ($\frac{\partial}{\partial \alpha} = 0$).

All these model assumptions taken together, a dimensional analysis shows that the flow in the droplet is effectively driven by three equations [9, 39, 136]:

$$\frac{\partial p}{\partial r} = \mu \frac{\partial^2 u}{\partial z^2}, \quad (2.3)$$

$$\frac{\partial p}{\partial z} = 0, \quad (2.4)$$

$$\frac{1}{r} \frac{\partial}{\partial r}(ru) + \frac{\partial w}{\partial z} = 0. \quad (2.5)$$

Here, u and w are the radial and axial components of the velocity, respectively. At the liquid-air interface a shear stress is present if there is a surface tension gradient. This corresponds to a boundary condition given by

$$\mu \frac{\partial u}{\partial z} = \frac{\partial \sigma_{lg}}{\partial r}. \quad (2.6)$$

With the use of this boundary condition and the no-slip boundary condition $u|_{z=0} = 0$, twofold integration of Equation (2.3) over the vertical coordinate yields the radial velocity

$$\begin{aligned} u(r, z, t) &= \frac{1}{\mu} \int_0^z \left(-\frac{\partial p}{\partial r}(h - z') + \frac{\partial \sigma_{lg}}{\partial r} \right) dz' \\ &= \frac{1}{\mu} \left(-\frac{\partial p}{\partial r} \left(hz - \frac{1}{2}z^2 \right) + \frac{\partial \sigma_{lg}}{\partial r} z \right), \end{aligned} \quad (2.7)$$

where $h(r, t)$ is the local droplet height.

Substituting this expression for $u(r, z, t)$ in Equation (2.5) followed by integration over z , enables one to find an expression for $w(r, z, t)$:

$$\begin{aligned} w(r, z, t) &= - \int_0^h \frac{1}{r} \frac{\partial}{\partial r}(ru) dz \\ &= \frac{1}{\mu} \left(\frac{1}{r} \frac{\partial}{\partial r} \left(r \frac{\partial p}{\partial r} \right) \left(\frac{1}{2}hz^2 - \frac{1}{6}z^3 \right) + \frac{1}{2}z^2 \left(\frac{\partial h}{\partial r} \frac{\partial p}{\partial r} - \frac{1}{r} \frac{\partial}{\partial r} \left(r \frac{\partial \sigma_{lg}}{\partial r} \right) \right) \right). \end{aligned} \quad (2.8)$$

Here, the impenetrable-substrate-condition $w|_{z=0} = 0$ is used. If the substrate is actually porous and fluid is imbibed with an (axial) absorption velocity W_p , this velocity can simply be subtracted from Equation (2.8) as is done in Chapter 5.

The kinematic boundary condition is given by $\partial_t h = -(\partial_r h)u|_{z=h} + w|_{z=h} + w_e$, where ∂_a denotes a partial derivative with respect to variable a and w_e is the evaporative volume flux. The droplet evolution can subsequently be expressed as:

$$\frac{\partial h}{\partial t} = -\frac{\partial h}{\partial r}u|_{z=h} - \int_0^h \frac{1}{r} \frac{\partial}{\partial r}(ru) dz + w_e. \quad (2.9)$$

With the use of the Leibniz integral rule this can be rewritten as:

$$\begin{aligned}\frac{\partial h}{\partial t} &= -\frac{1}{r} \frac{\partial}{\partial r} \int_0^h r u dz + w_e \\ &= \frac{1}{r\mu} \frac{\partial}{\partial r} \left(\frac{r h^3}{3} \frac{\partial p}{\partial r} - \frac{r h^2}{2} \frac{\partial \sigma_{lg}}{\partial r} \right) + w_e.\end{aligned}\quad (2.10)$$

This is the height evolution equation valid in the lubrication approximation in the form that is used in this work. The boundary and initial conditions to which $h(r, t)$ is subjected are given by:

$$\left(\frac{\partial h}{\partial r} \right)_{r=0} = 0, \quad (2.11)$$

$$\left(\frac{\partial^3 h}{\partial r^3} \right)_{r=0} = 0, \quad (2.12)$$

$$h(R, t) = 0, \quad (2.13)$$

$$h(r, 0) = h_0(r). \quad (2.14)$$

These denote the symmetry condition at $r = 0$, the position of the contact line and the initial shape, respectively. In this work, these boundary conditions hold unless stated otherwise (e.g. in case there is a precursor film present).

2.1.2. Derivation with slip

If slip is allowed, boundary condition $u|_{z=0} = 0$ is replaced by the Navier slip condition

$$u(r, 0) = \beta \left(\frac{\partial u}{\partial z} \right)_{z=0}, \quad (2.15)$$

where β is the slip length. This results in a different expression for the radial velocity, given by:

$$u(r, z, t) = \frac{1}{\mu} \left(-\frac{\partial p}{\partial r} \left(h z - \frac{1}{2} z^2 + \beta h \right) + \frac{\partial \sigma_{lg}}{\partial r} (z + \beta) \right). \quad (2.16)$$

Substituting this expression for u in the kinematic boundary condition, along with the new formulation of w , results in a slightly different height evolution equation given by:

$$\frac{\partial h}{\partial t} = \frac{1}{r\mu} \frac{\partial}{\partial r} \left[r \left(\frac{h^3}{3} + \beta h^2 \right) \frac{\partial p}{\partial r} - r \left(\frac{h^2}{2} + \beta h \right) \frac{\partial \sigma_{lg}}{\partial r} \right] + w_e. \quad (2.17)$$

If the contact line is allowed to slip, a constitutive relation for R is required that describes the contact line velocity [168]. In this work, we use the relation:

$$\frac{dR}{dt} = \begin{cases} k \|\theta - \theta_{adv}\|^a & \text{if } \theta_{adv} \leq \theta \\ 0 & \text{if } \theta_{rec} < \theta < \theta_{adv} \\ -k \|\theta - \theta_{rec}\|^a & \text{if } \theta \leq \theta_{rec} \end{cases} \quad (2.18)$$

Here, k is a typical sensitivity of the contact line position to deviations of the contact angle θ from the receding contact angle θ_{rec} or the advancing contact angle θ_{adv} and a is a power-law index, which can range from 1 to 3. This relation is extensively used and experimentally validated in literature [12, 21, 28, 51, 58, 66, 166].

Note that with Equation (2.18) it is possible to model contact line hysteresis, since the contact line only moves for $\theta_{adv} \leq \theta \leq \theta_{rec}$. If this is not desired, one can simply set $\theta_{adv} = \theta_{rec}$ (see Chapter 3).

The actual contact angle θ can be calculated from the slope $\partial_r h$ at the contact line and, in case of surfactants, θ_e can be computed by means of Young's equation:

$$\theta = \cos^{-1} \left(\frac{1}{\sqrt{1 + (\partial_r h|_R)^2}} \right), \quad (2.19)$$

$$\theta_e = \cos^{-1} \left(\frac{\sigma_{lg}[\Gamma(R, 0)]}{\sigma_{lg}[\Gamma(R, t)]} \cos(\theta_0) \right). \quad (2.20)$$

Here, θ_0 is the initial contact angle.

2.1.3. Pressure in the droplet

The pressure p in the droplet is given by Derjaguin's equation [38, 165, 170]:

$$p = p_L - \Pi, \quad (2.21)$$

where p_L is the Laplace pressure and Π the disjoining pressure. Both these pressure terms are independent of z , which is in accordance with Equation (2.4) and means that results are more accurate for lower values of ϵ (see e.g. [71, 72]).

The Laplace pressure is given by

$$p_L = -\frac{1}{r} \frac{\partial}{\partial r} \left(\sigma_{lg} \frac{r \partial_r h}{\sqrt{1 + (\partial_r h)^2}} \right). \quad (2.22)$$

Contrary to the traditional formulation of the Laplace pressure, surface tension σ_{lg} is also part of the derivative in Equation (2.22), rather than that it is written outside the brackets. This is because σ_{lg} depends on the local surfactant concentration and thus on r . As shown by Thiele et al. [178] the surface tension is required to be part of the radial derivative in that case.

Apart from the slip model introduced in the previous section, an alternative way of modeling a moving contact line is by introducing a precursor film, which is a thin fluid layer that covers the substrate around the droplet. This effectively resolves the contact line singularity, because the drop height is no longer zero, but (approximately) equal to the precursor film height at the contact line. Therefore, there is no slip required for the contact line to move.

If a precursor film is present, a nonzero disjoining pressure Π is required to keep it stable. This pressure term accounts for the intermolecular forces and in this model it

is given by

$$\Pi = B \left(\left(\frac{h_s}{h} \right)^n - \left(\frac{h_s}{h} \right)^m \right). \quad (2.23)$$

Here, B , n and m are positive constants (with $n > m$) and h_s is the precursor film height for which Π equals zero. The height h_s does not necessarily correspond to the real precursor film height, but only represents the zero-pressure height.

This formulation of the disjoining pressure consists of an attractive and a repulsive component ($B(h_s/h)^m$ and $B(h_s/h)^n$ respectively), corresponding to the attractive and repulsive molecular forces that govern the physics of the precursor film [152]. In literature, one often encounters disjoining pressure formulations that only include the attractive forces (see e.g. Karapetsas et al. [86]). In these cases the droplet will spread indefinitely, because there is no equilibrium contact angle corresponding to this formulation.

The value of B can be related to the equilibrium contact angle θ_e . As shown by Starov and Velarde [171], the equilibrium contact angle θ_e can be approximated by

$$\cos \theta_e \approx 1 + \frac{1}{\sigma_{lg}} \int_{h_e}^{\infty} \Pi dh, \quad (2.24)$$

where h_e is the equilibrium precursor film height. If the disjoining pressure solely consists of attractive forces, the integral is positive, resulting in $\cos \theta_e > 1$, implying complete wetting. For Equations (2.23) and (2.24) however, the equilibrium contact angle is given by

$$\cos \theta_e \approx 1 + \frac{B}{\sigma_{lg}} \left(\frac{1}{n-1} \frac{h_s^n}{h_e^{n-1}} - \frac{1}{m-1} \frac{h_s^m}{h_e^{m-1}} \right) \quad (2.25)$$

which implies partial wetting, since $h_s \approx h_e$. Also, it follows that for a given σ_{lg} and θ_e an expression for B can be estimated (as done by Schwartz and Eley [152]):

$$B = \frac{1}{h_s} \frac{(n-1)(m-1)}{n-m} \sigma_{lg} (1 - \cos \theta_e). \quad (2.26)$$

For a case with surfactants, where surface tension $\sigma_{lg}[\Gamma(R, t)]$ and contact angle change, Equation (2.26) can be modified accordingly:

$$B = \frac{1}{h_s} \frac{(n-1)(m-1)}{n-m} (\sigma_{lg}[\Gamma(R, t)] - \sigma_{lg}[\Gamma(R, 0)] \cos \theta_0). \quad (2.27)$$

Here, θ_0 denotes the initial contact angle.

2.2. Absorption model

The droplet can be absorbed into the porous substrate as a result of capillary action. This flow can be modeled on a macroscopic level by applying Darcy's law, which is often used for the flow through porous media [2, 4, 5, 164].

Darcy's law gives a relation for the velocity field $\vec{u}_p = (u_p, w_p)$:

$$u_p = -\frac{\kappa}{\mu} \left(\frac{\partial p_p}{\partial r} \right); \quad (2.28)$$

$$w_p = -\frac{\kappa}{\mu} \left(\frac{\partial p_p}{\partial z} \right). \quad (2.29)$$

Here, κ is the permeability of the substrate and p_p the pressure in the wetted region. Depending on the structure of the porous material, a good measure for κ is given by the Carman-Kozeny equation [20, 90], which is a model for the flow through a packed bed of solid spheres with diameter d . The permeability is subsequently given by:

$$\kappa = \frac{\eta^3 d^2}{180(1-\eta)^2}, \quad (2.30)$$

with η the porosity of the porous medium.

Given mass conservation, it follows that the pressure field can be found by solving the Laplace equation:

$$\frac{1}{r} \frac{\partial}{\partial r} (r u_p) + \frac{\partial w_p}{\partial z} = \frac{1}{r} \frac{\partial}{\partial r} \left(r \frac{\partial p_p}{\partial r} \right) + \frac{\partial^2 p_p}{\partial z^2} = 0. \quad (2.31)$$

The boundary conditions which p_p is subjected to are given by:

$$p_p|_{z=0} = p(r, t) \quad \text{for } r < R; \quad (2.32)$$

$$\frac{\partial p_p}{\partial z}|_{z=0} = 0 \quad \text{for } r > R; \quad (2.33)$$

$$p_p|_{z=-h_p} = p_c. \quad (2.34)$$

Equation (2.32) describes the pressure that the droplet exerts on the substrate, Equation (2.33) is the no penetration condition at the substrate surface next to the droplet and Equation (2.34) is the capillary suction the fluid in the wetted region experiences at its interface, defined at $z = -h_p$. The corresponding capillary pressure p_c can be estimated by considering the capillary action in a single, round channel:

$$p_c = -\frac{4\sigma_{lg} \cos \theta_{adv}}{d}. \quad (2.35)$$

Here, θ_{adv} is the advancing contact angle. Note that the channel diameter used in the expression for p_c is assumed to be equal to the sphere diameter that is used for estimating κ .

With an expression for the velocity field, the evolution equation for h_p can be found, similar to Equation (2.10):

$$\frac{\partial h_p}{\partial t} = -\frac{1}{\eta r} \frac{\partial}{\partial r} \int_0^{h_p} r u_p dz + \frac{1}{\eta} W_p. \quad (2.36)$$

Suction velocity W_p is here equal to the axial porous velocity at the substrate level $W_p = w_p(r, z = 0)$. This velocity is also to be added to Equation (2.10).

Similar to the droplet, in the porous medium there are symmetry conditions at $r = 0$, specifically $\partial_r h_p = \partial_r p_p = \partial_r u_p = \partial_r w_p = 0$. Furthermore, initially there is a thin fluid film h^* in the porous medium, just below the area covered by the droplet, which is required to remove the incompatibility of Equations (2.32) and (2.34) for $h_p = 0$.

Darcy's law is chosen for its simplicity over other models, while still being sufficiently accurate [149] and able to deal with the boundary conditions that are involved. However, it would be possible to generalize Darcy's law by including Brinkman's extension [17, 117]. The pressure equation will then get the form:

$$u_p + \frac{\mu}{r} \frac{\partial}{\partial r} \left(r \frac{\partial u_p}{\partial r} \right) - \mu \frac{u_p}{r^2} + \mu \frac{\partial^2 u_p}{\partial z^2} = -\frac{\kappa}{\mu} \left(\frac{\partial p_p}{\partial r} \right); \quad (2.37)$$

$$w_p + \frac{\mu}{r} \frac{\partial}{\partial r} \left(r \frac{\partial w_p}{\partial r} \right) + \mu \frac{\partial w_p}{\partial z^2} = -\frac{\kappa}{\mu} \left(\frac{\partial p_p}{\partial z} \right). \quad (2.38)$$

Given the second order nature of this equation, this form is especially relevant for prescribing additional, non-pressure boundary conditions. For example, if a no-slip wall is present in the porous flow, the zero-velocity boundary condition can be imposed through Brinkman's extension, while this is not possible through the traditional form of Darcy's law. Other applications of Brinkman's extension include the flow through a porous medium in which the grains are porous themselves [98].

Nevertheless, given the boundary conditions that are involved in our problem, it is expected that Darcy's law is sufficiently accurate. However, Brinkman's extension should be used if additional boundary conditions are to be prescribed. In that case, the system of equations also would need to be solved for $u_p(r, z)$ and $w_p(r, z)$, rather than for $p_p(r, z)$ only.

2.3. Interfacial surfactant concentration

In this section the transport equation for surfactant at the interface is derived.

At any infinitesimal liquid-air interface patch a molar interfacial concentration of adsorbed surfactant Γ can exist. As given by Stone [173], the transport of surfactant is described by the convection-diffusion equation:

$$\frac{\partial \Gamma}{\partial t} + \vec{\nabla}_s \cdot (\Gamma \vec{u}_s) = D_\Gamma \vec{\nabla}_s^2 \Gamma, \quad (2.39)$$

where $\vec{\nabla}_s = \frac{1}{1+(\partial_r h)^2} (\vec{e}_r + \partial_r h \vec{e}_z) \frac{\partial}{\partial r} + \frac{1}{r} \vec{e}_\alpha \frac{\partial}{\partial \alpha}$ is the surface gradient operator, with \vec{e}_i the unit vector in direction i . Furthermore, \vec{u}_s is the interface velocity vector and D_Γ the surface diffusion coefficient. Note that all axial derivatives are dropped in $\vec{\nabla}_s$, since both Γ and \vec{u}_s are independent of z .

The formulation of Equation (2.39) is the conservative form of the standard surfactant transport equation. However, it is generally more practical to express it in non-conservative form as is often done in literature [48, 86, 178]. Then, the equation is formulated in terms of the evolution of the tangential interface velocity \vec{u}_t and normal

interface velocity \vec{u}_n . The equation becomes:

$$\frac{\partial \Gamma}{\partial t} = -\vec{\nabla}_s \cdot (\Gamma \vec{u}_t) - \Gamma U_n \vec{\nabla}_s \cdot \vec{n} + D_\Gamma \vec{\nabla}_s^2 \Gamma, \quad (2.40)$$

where $U_n = |\vec{u}_n| = \frac{\partial_t h}{\sqrt{1+(\partial_r h)^2}}$. It is possible to approximate the surface gradients in the tangential convection and the diffusion term as the non-surface gradient $\vec{\nabla} = \vec{e}_r \frac{\partial}{\partial r} + \frac{1}{r} \vec{e}_\theta \frac{\partial}{\partial \theta}$ and subsequently replacing the radial derivatives $\frac{\partial}{\partial r}$ with surface derivatives $\frac{\partial}{\partial s}$, which are given by $\frac{\partial}{\partial s} = \frac{1}{\sqrt{1+(\partial_r h)^2}} \frac{\partial}{\partial r}$.

$$\frac{\partial \Gamma}{\partial t} = -\frac{1}{r} \frac{\partial (r U_t \Gamma)}{\partial s} + \frac{\Gamma U_n}{\sqrt{1+(\partial_r h)^2}} \left(\frac{\partial^2 h}{\partial r^2} + \frac{1}{r} \frac{\partial h}{\partial r} \right) + \frac{D_\Gamma}{r} \frac{\partial (r \partial_s \Gamma)}{\partial s}. \quad (2.41)$$

Here, U_t is the tangential interface velocity, which is equal to the tangential fluid velocity at the interface. Thus, it can be found by taking the inner product between fluid velocity vector $\vec{u} = u \vec{e}_r + w \vec{e}_z$ and tangential unit vector $\vec{t} = (\vec{e}_r + \partial_r h \vec{e}_z) / \sqrt{1+(\partial_r h)^2}$.

Equation (2.41) generally gives good accuracy and similar results if the full surface gradients are calculated [58, 59, 60]. However, for relatively large slopes the surface gradients should be calculated completely. The tangential convection term in Equation (2.40) then becomes:

$$\vec{\nabla}_s \cdot (\Gamma \vec{u}_t) = \frac{1}{1+(\partial_r h)^2} \left(\frac{\partial}{\partial r} (u_t \Gamma) + \frac{\partial h}{\partial r} \frac{\partial}{\partial r} (w_t \Gamma) \right) + \frac{u_t \Gamma}{r}. \quad (2.42)$$

Here, u_t and w_t are the components of tangential interface velocity vector \vec{u}_t that is given by:

$$\vec{u}_t = (\vec{u} \cdot \vec{t}) \vec{t} = \left(\frac{u + w \partial_r h}{1+(\partial_r h)^2} \right) \vec{e}_r + \frac{\partial h}{\partial r} \left(\frac{u + w \partial_r h}{1+(\partial_r h)^2} \right) \vec{e}_z. \quad (2.43)$$

Similarly, the Laplacian in the diffusion term of Equation (2.40) can be calculated in full surface coordinates:

$$\begin{aligned} \vec{\nabla}_s^2 \Gamma &= \frac{1}{1+(\partial_r h)^2} \left(\frac{\partial}{\partial r} \left(\frac{1}{1+(\partial_r h)^2} \right) \frac{\partial \Gamma}{\partial r} + \frac{1}{1+(\partial_r h)^2} \frac{\partial^2 \Gamma}{\partial r^2} \right) + \\ &\quad \frac{\partial_r h}{1+(\partial_r h)^2} \left(\frac{\partial}{\partial r} \left(\frac{\partial_r h}{1+(\partial_r h)^2} \right) \frac{\partial \Gamma}{\partial r} + \frac{\partial_r h}{1+(\partial_r h)^2} \frac{\partial^2 \Gamma}{\partial r^2} \right) + \\ &\quad \frac{1}{1+(\partial_r h)^2} \frac{1}{r} \frac{\partial \Gamma}{\partial r}. \end{aligned} \quad (2.44)$$

In case of relatively large slopes an additional term needs to be introduced in the surfactant transport equation that compensates for the displacement of the surface coordinates that move along the normal of the surface. For large slopes this displacement is significant enough to cause a deviation of the surfactant mass at the surface coordinates in comparison to the global coordinate r . As Wong et al. [189] show, the relation between the surfactant concentration at the surface coordinates and at the global coordinates is given by:

$$\left[\frac{\partial \Gamma}{\partial t} \right]_s = \left[\frac{\partial \Gamma}{\partial t} \right]_g - \dot{\vec{X}} \cdot \vec{\nabla}_s \Gamma. \quad (2.45)$$

Here, s and g denote the surface and global coordinates respectively and the subscripts indicate which of the two is kept constant in the derivative. Furthermore, \vec{X} is the velocity vector with which the interface coordinates move along the global coordinates. In the considered case, it is desired to express Γ as a function of r . From this it follows that $\vec{X} = \partial_t h \vec{e}_z$, since this vector gives the displacement of the interface as a function of r . In terms of r the correction term is given by:

$$\vec{X} \cdot \vec{\nabla}_s \Gamma = -\frac{\partial h}{\partial t} \frac{\partial_r h}{1 + (\partial_r h)^2} \frac{\partial \Gamma}{\partial r}. \quad (2.46)$$

If slopes are small, it is acceptable within the approximation of the lubrication approach to neglect the coordinate transformation term. Adsorption and desorption terms can be added to Equation (2.46) where applicable.

2.4. Bulk surfactant concentration

In this section a transport equation is derived for the surfactant in the bulk of the droplet.

A thin, ring-shaped volume dV is considered at an arbitrary r -coordinate with some dissolved mass m in it. The change in mass due to transport dm over a time interval dt is given by:

$$dm = 2\pi \left((\phi \bar{u} h)_{r,r} - (\phi \bar{u} h)_{r+dr}(r+dr) \right) dt - 2\pi D_\phi \left(\left(\frac{d\phi}{dr} h \right)_r - \left(\frac{d\phi}{dr} h \right)_{r+dr} (r+dr) \right) dt. \quad (2.47)$$

Here, ϕ is the local concentration of the dissolved mass, \bar{u} the height-averaged radial fluid velocity, h the height of dV and D_ϕ the diffusion coefficient. The subscripts denote the radial coordinate at which a quantity is defined.

Now, a new variable $\psi(r, t) = \phi(r, t)h(r, t) = \frac{m(r, t)}{2\pi r dr}$ is introduced, which can be seen as the concentration projected on the substrate. It is preferable to use $\psi(r, t)$ rather than $\phi(r, t)$ as a variable, because $\psi(r, t)$ is independent of $h(r, t)$ [179]. Therefore, if $\psi(r, t)$ is used, any change in concentration as a result of a change in h , is automatically taken into account. If $\phi(r, t)$ would be used as variable for the bulk concentration, an additional term would be required, similar to Equation (2.45). The rate of change in $\psi(r, t)$ is given by:

$$\frac{d\psi}{dt} = \frac{1}{r dr} \left((\bar{u}\psi)_{r,r} - (\bar{u}\psi)_{r+dr}(r+dr) \right) - \frac{D_\phi}{r dr} \left(\left(\frac{d\phi}{dr} h \right)_r - \left(\frac{d\phi}{dr} h \right)_{r+dr} (r+dr) \right). \quad (2.48)$$

Letting $dt \rightarrow 0$ and $dr \rightarrow 0$ then yields:

$$\frac{\partial \psi}{\partial t} = \frac{1}{r} \frac{\partial}{\partial r} \left(-r\psi\bar{u} + D_\phi r h \frac{\partial \phi}{\partial r} \right). \quad (2.49)$$

The height-averaged radial velocity \bar{u} is found by calculating the average of Equation (2.7):

$$\bar{u} = \frac{1}{h\mu} \int_0^h dz \left(-\frac{\partial p}{\partial r} \left(hz - \frac{1}{2}z^2 \right) + \frac{\partial \sigma_{lg}}{\partial r} z \right) = \frac{1}{\mu} \left(-\frac{1}{3}h^2 \frac{\partial p}{\partial r} + \frac{1}{2}h^2 \frac{\partial \sigma_{lg}}{\partial r} \right). \quad (2.50)$$

Subsequently, substitution of \bar{u} in Equation (2.49) yields:

$$\frac{\partial \psi}{\partial t} = \frac{1}{r} \frac{\partial}{\partial r} \left(\frac{rh^2 \psi}{3\mu} \frac{\partial p}{\partial r} - \frac{rh\psi}{2\mu} \frac{\partial \sigma_{lg}}{\partial r} + D_\phi rh \frac{\partial \phi}{\partial r} \right). \quad (2.51)$$

This equation can be used to describe the transport of both monomers $\psi(r, t) = \phi(r, t)h(r, t)$ and micelles $\zeta(r, t) = M(r, t)h(r, t)$ in the bulk of the droplets. Source terms, like adsorption/desorption and micelle formation/decomposition can be added where appropriate.

2.5. Pore surfactant concentration

In contrast to the surfactant bulk concentration in the droplet, the bulk concentration in the porous medium $\phi_p(r, z, t)$ is also assumed to depend on the axial coordinate z . The reason for this is that the vertical dimension of the wetted region typically is of the same order of magnitude as the horizontal dimension. Furthermore, the pressure gradient has a significant component in axial direction. The evolution of $\phi_p(r, z, t)$ is thus to be described by an axisymmetric 3D convection-diffusion-adsorption equation:

$$\frac{\partial \phi_p}{\partial t} = -\frac{1}{r} \frac{\partial}{\partial r} \left(r \phi_p \frac{u_p}{\eta} \right) - \frac{\partial}{\partial z} \left(\phi_p \frac{w_p}{\eta} \right) + \frac{D_{\phi,p}}{r} \frac{\partial}{\partial r} \left(r \frac{\partial \phi_p}{\partial r} \right) + D_{\phi,p} \frac{\partial^2 \phi_p}{\partial z^2} - J_{\phi S}. \quad (2.52)$$

Here, $D_{\phi,p}$ is the diffusion coefficient in the pores and $J_{\phi S}$ accounts for the sorption between the bulk and the walls of the pores. This effect is not considered in the droplet itself, because there the total liquid-solid interface is much smaller. Furthermore, adsorption onto the solid-liquid interface does not directly influence the flow behavior (it cannot cause Marangoni flow) and will not change the contact angle of the droplet, because only pinned cases are considered when surfactants are involved. The concentration $\phi_p(r, z, t)$ is subject to the following boundary conditions:

$$\phi_p(r, 0, t)w_p(r, 0, t) = \phi(r, t)W_p(r, t); \quad (2.53)$$

$$\frac{\partial \phi_p}{\partial r} \Big|_{r=0} = 0. \quad (2.54)$$

Furthermore, surfactant cannot be transported outside the wetted region.

The reduction in energy at the solid-liquid interface σ_{sl} will affect the suction pressure, which is implied by Young's equation: $\sigma_{sg} - \sigma_{sl} = \sigma_{lg} \cos \theta_{adv}$, with solid-gas interfacial tension σ_{sg} . Substitution of the left-hand side of Young's equation in Equation (2.35) results in

$$p_c = -\frac{4(\sigma_{sg} - \sigma_{sl}(\bar{S}_{int}))}{d}. \quad (2.55)$$

Adsorbing surfactants will therefore increase the magnitude of the capillary suction pressure. The volume-averaged value of $S(r, z, t)$ at the interface, i.e. \bar{S}_{int} , is used for the calculation of p_c . This results in better stability, since p_c becomes more uniform.

The surfactant concentration at the liquid-air interface in the porous medium is not taken into account, because it does not affect p_c (as shown by [99, 100]). Furthermore, due to the adsorption kinetics $\psi h \gg \Gamma$, meaning that adsorption onto the liquid-air interface has no significant influence on the bulk concentration. This type of surfactant is typically called a 'penetrant' and is used to influence liquid absorption.

2.6. Evaporation model

The evaporative mass flux of water \dot{m}_w is given by:

$$\dot{m}_w = -\frac{D_{wa}M_w p_{sat,w}}{R_u T} \frac{\partial \hat{p}_w}{\partial n}, \quad (2.56)$$

with D_{wa} the water vapor diffusivity in air [93], M_w the molar mass, $p_{sat,w}$ the homogeneous saturation pressure, which is assumed to be constant, and $\hat{p}_w = \frac{p_w}{p_{sat,w}}$ with p_w the local vapor pressure [39]. Furthermore, R_u is the universal gas constant and T the temperature.

Regarding the vapor field, Deegan et al, [37] and Hu and Larson [70] showed that the vapor diffusion for single component droplets can be considered as instantaneous. Combined with the assumption of no air flow, this results in the following Laplace equation:

$$\nabla^2 \hat{p}_w = 0. \quad (2.57)$$

The corresponding boundary conditions of Equation (2.57) are:

$$\hat{p}_w|_{z=h} = 1 \quad \text{for } r < R; \quad (2.58)$$

$$\frac{\partial \hat{p}_w}{\partial z}|_{z=0} = 0 \quad \text{for } r > R; \quad (2.59)$$

$$\hat{p}_w = RH_w \quad \text{for } (r, z) \rightarrow \infty. \quad (2.60)$$

Equation (2.58) represents the saturated vapor at the liquid-air interface, Equation (2.59) the prohibition of vapor penetration in the substrate and Equation (2.60) the relative humidity in the surroundings (where RH_w is the relative humidity). For the precursor film model, the radial coordinate corresponding to R is defined to be the point where $h = 1.2h_s$, which results in the droplet having approximately the same effective radius as if it would have been a spherical cap.

The evaporation velocity w_e in Equation (2.10) can subsequently be calculated by:

$$w_e = -\frac{\dot{m}_w}{\rho} \sqrt{1 + \left(\frac{\partial h}{\partial r}\right)^2}. \quad (2.61)$$

Similarly to Equation (2.22), the argument of the square root makes the expression a better approximation for higher slopes than it would when approximated as unity.

It is possible to derive an analytical solution to the Laplace equation $\nabla^2 \hat{p}_l = 0$, as shown by Deegan et al. [37] and Popov [142]. This is done by converting the cylindrical coordinates to toroidal coordinates:

$$r = R \frac{\sinh \alpha}{\cosh \alpha - \cos \beta}, \quad z = R \frac{\sinh \beta}{\cosh \alpha - \cos \beta}. \quad (2.62)$$

The position of the interface then becomes defined at $0 \geq \alpha$ and $\beta = \beta_0 = \pi - \theta$, where θ denotes the contact angle. The drop apex (at $r = 0$) corresponds to $\alpha = 0$ and $r \rightarrow R$ as $\alpha \rightarrow \infty$.

Subsequently, given the boundary conditions $\hat{p}_l|_{\beta=\beta_0} = 1$ and $\hat{p}_l|_{\beta \rightarrow \infty} = RH$, the solution of the Laplace equation can be shown to be [102]:

$$\hat{p}_l = RH + (1 - RH)N(\alpha, \beta) \int_0^\infty d\tau K(\tau, \beta) C_\tau(\alpha) \frac{\cosh(\theta\tau)}{\cosh(\pi\tau)}, \quad (2.63)$$

with

$$N(\alpha, \beta) = \sqrt{2 \cosh \alpha - 2 \cos \beta}, \quad (2.64)$$

$$K(\tau, \beta) = \frac{\cosh((2\pi - \beta)\tau)}{\cosh((\pi - \theta)\tau)}, \quad (2.65)$$

$$C_\tau(\alpha) = P_{-1/2+i\tau}(\cosh \alpha). \quad (2.66)$$

Here, $P_{-1/2+i\tau}$ denotes Legendre functions of the first kind with a fractional complex index.

Subsequently, for the evaporation rate the normal derivative of the vapor field at the drop interface needs to be calculated, which is given by [142]:

$$\frac{\partial \hat{p}_l}{\partial n} = \frac{\cosh \alpha - \cos \beta}{R} \partial_\beta \hat{p}_l|_{\beta=3\pi-\theta}. \quad (2.67)$$

Substitution of Equation (2.63) in Equation (2.67) gives:

$$\frac{\partial \hat{p}_l}{\partial n} = \frac{1 - RH}{R} \left(\frac{\sin \theta}{2} + N'(\alpha) \int_0^\infty d\tau K'(\tau) C_\tau(\alpha) \frac{\cosh(\theta\tau)}{\cosh(\pi\tau)} \right), \quad (2.68)$$

with

$$N'(\alpha) = \sqrt{2}(\cosh \alpha + \cos \theta)^{3/2}, \quad (2.69)$$

$$K'(\tau) = \tau \tanh((\pi - \theta)\tau). \quad (2.70)$$

This can be rewritten into [107]:

$$\frac{\partial \hat{p}_l}{\partial n} = \frac{\pi(\cosh \alpha + \cos \theta)^{3/2}}{2R(\pi - \theta)^2} \int_\alpha^\infty dx \frac{\tanh\left(\frac{\pi x}{2(\pi - \theta)}\right)}{\cosh\left(\frac{\pi x}{2(\pi - \theta)}\right) \sqrt{\cosh x - \cosh \alpha}}. \quad (2.71)$$

The integral in this expression needs to be evaluated numerically. For a more detailed derivation, the reader is referred to Diddens et al., who carried it out both for single component and multi-component evaporation and showed the analytical solution to be similar in terms of accuracy to other numerical solution techniques for the vapor field [39].

2.7. Adsorption model

The transport between the interface and the bulk is by means of continuous adsorption and desorption of molecules that overall tends towards a dynamic equilibrium. Furthermore, there is a limited amount of space available at the interface for surfactants,

so as the interfacial concentration increases the adsorption rate tends to decrease, while the desorption rate increases. This behavior can be described by the following reaction equation [48, 85]:



Here, $S (= 1 - \frac{\Gamma}{\Gamma_\infty})$ indicates the fraction of available space at the interface, k_a^Γ is the interfacial adsorption coefficient, and k_d^Γ the interfacial desorption coefficient. Thus, the interfacial adsorption flux is given by:

$$J_{\Gamma\phi} = k_a^\Gamma \phi \left(1 - \frac{\Gamma}{\Gamma_\infty} \right) - k_d^\Gamma \Gamma. \quad (2.73)$$

In this equation it can indeed be recognized that the first, adsorption term increases as the bulk concentration increases and approaches zero as $\Gamma \rightarrow \Gamma_\infty$, while the second, desorption term becomes more negative as Γ increases. This behavior corresponds indeed to Equation (2.72).

The surface tension at the liquid-air interface is given by the Szyszkowski equation of state, also known as the Frumkin equation of state, which takes into account the repelling effect individual surfactant molecules have on each other [22]. This closure relation is typically valid up to intermediate interfacial concentrations that are not too close to the maximum concentration Γ_∞ . The Szyszkowski equation is given by:

$$\sigma_{lg} = \sigma_{lg,0} + R_u T \Gamma_\infty \ln \left(1 - \frac{\Gamma}{\Gamma_\infty} \right). \quad (2.74)$$

In this equation, $\sigma_{lg,0}$ denotes the liquid-gas surface tension for a surfactant-free liquid. For lower concentrations the equation reduces to the linear, dilute equation of state, given by:

$$\sigma_{lg} = \sigma_{lg,0} - R_u T \Gamma. \quad (2.75)$$

Note that surfactant adsorption onto the substrate surface is not taken in consideration here, because this will not have a direct effect on the internal flow. Marangoni flow can only occur as a result of a surface tension gradient at a free interface. Any indirect influences of substrate sorption on the flow – surfactant being removed or added to the bulk – are considered less significant.

Similar to Equation (2.72), a reaction equation can be written for the formation of micelles:



Here, k_a^M is the micelle formation coefficient and k_d^M the micelle decomposition coefficient. Furthermore, N denotes the preferred number of monomers in a micelle. It is assumed that only micelles of this size are formed, which is often the case in reality [75]. Equation (2.76) can subsequently be written into a micelle formation rate $J_{M\phi}$ [11, 48, 85]:

$$J_{M\phi} = k_a^M \phi^N - k_d^M M. \quad (2.77)$$

Given this equation, it is possible to approximate the reaction constants in terms of the critical micelle concentration (CMC), which is the monomer concentration at which

micelles start to form, and local concentrations. From Equation (2.77), it can be seen that the equilibrium concentrations are given by $\frac{k_a^M}{k_d^M} = \frac{M}{\phi^N}$. Now, if $\Phi (= NM + \phi)$ is the total concentration of surfactant monomers in the bulk, substitution of the initial total concentration Φ_0 results in:

$$\frac{k_a^M}{k_d^M} = \frac{\Phi_0 - CMC}{N(CMC)^N}. \quad (2.78)$$

Here, it should be noted that in equilibrium $\phi = CMC$, given that there are micelles present. Of course, it is still required to choose one of the reaction constants to define the time scales of the reactions.

The sorption term $J_{\phi S}$ in the porous medium is given by:

$$J_{\phi S} = \frac{4}{d} k_a^S \phi_p \left(1 - \frac{S}{S_\infty} \right) - k_d^S S, \quad (2.79)$$

with k_a^S and k_d^S the solid-liquid adsorption and desorption coefficient respectively, $S(r, z, t)$ the amount of adsorbed surfactant per unit of volume and S_∞ the maximum adsorbed surfactant concentration per unit of volume.

The $\frac{4}{d}$ prefactor is the area of the channel walls per unit of wetted volume [164]. A control volume V contains cylindrical channels with a total volume of $\eta V = L\pi/4d^2$ and a total channel wall area $A_p = L\pi d$, with L the total length of the channels. The area to volume ratio is therefore $\frac{A_p}{\eta V} = \frac{4}{d}$.

As an equation of state for the surface tension of the solid-liquid interface in the porous medium, σ_{sl} , a variant of the Sheludko equation [86, 160] is used:

$$\sigma_{sl} = \sigma_{sl,0} \left(1 + \frac{S}{S_\infty} ((\sigma_{sl,0}/\sigma_{sl,\infty}) - 1) \right)^{-3}. \quad (2.80)$$

Here, $\sigma_{sl,0}$ and $\sigma_{sl,\infty}$ are the surface tensions of a surfactant-free and fully covered interface respectively. Equation (2.80) is appropriate for surfactant concentrations that approach the maximum, which is the case in this work for the liquid-solid interface. Hence, this equation of state is used rather than e.g. the Szyszkowski equation that is used for the liquid-air interface (Equation (2.74)).

At $t = 0$ no surfactant has adsorbed on the pore walls ($S(r, z, 0) = 0$).

2.8. Solute transport

In this section two different methods are presented that can be employed to model the evolution of solutes in the droplet: as a passive concentration and as a distinct phase.

If the solute is a passive concentration $C(r, z, t)$, the evolution can simply be described by a convection-diffusion equation:

$$\frac{\partial C}{\partial t} = -\frac{1}{r} \frac{\partial}{\partial r} (rCu) - \frac{\partial}{\partial z} (Cw) + D_C \frac{1}{r} \frac{\partial}{\partial r} \left(r \frac{\partial C}{\partial r} \right) + D_C \frac{\partial^2 C}{\partial z^2}. \quad (2.81)$$

Here, D_C denotes the bulk diffusion coefficient of the solute. The corresponding boundary and initial conditions are:

$$\frac{\partial C}{\partial r}\Big|_{r=0} = 0; \quad (2.82)$$

$$\frac{\partial C}{\partial z}\Big|_{z=0} = 0; \quad (2.83)$$

$$-\frac{\partial h}{\partial r} \frac{\partial C}{\partial r}\Big|_{z=h} + \frac{\partial C}{\partial z}\Big|_{z=h} = 0; \quad (2.84)$$

$$C(r, z, 0) = C_0. \quad (2.85)$$

Here, C_0 is the initial (homogeneous) concentration. The boundary conditions denote the axisymmetry at $r = 0$ and the solute not being transported through any of the interfaces (liquid-air and liquid-solid). If the substrate is porous Equation (2.83) can be ignored.

For higher solute concentrations Equation (2.8) is insufficient however and the particles should be considered as a separate solid phase. Both the mass fractions of the liquid and the solid phase ($y_w(r, z, t)$ and $y_s(r, z, t)$ respectively) can then be described by (e.g. see [39, 143])

$$\rho \left(\frac{\partial y_a}{\partial t} + \vec{U} \cdot \nabla y_a \right) = \nabla \cdot (\rho D_{ls} \nabla y_a) - \dot{m}_a \delta_h. \quad (2.86)$$

Here, y_a denotes the considered mass fraction (with $a = w, s$, denoting water and solute), D_{ws} is the mutual diffusion coefficient between the phases, \dot{m}_a is the sink term as a result of evaporation and δ_h the interface delta function. Mass fraction y_a is subject to the same boundary conditions as C , so Equations (2.82) - (2.85) hold if C is substituted by y_a .

Given that the fluid properties are dependent on the local mass fractions, these become a function of time and space, $\rho(r, z, t)$, $\mu(r, z, t)$, $D_{ls}(r, z, t)$. Therefore, the lubrication equation (2.17) and surfactant transport equations (2.40) and (2.51) need to be generalized before they can be applied.

Carrying out the same derivation as before but with non-constant fluid properties yields the velocity field (also see [39]):

$$u(r, z, t) = \int_0^z \frac{(-\partial_r p(r, t))(h(r, t) - z') + \partial_r \sigma_{lg}(r, t)}{\mu(r, z', t)} dz'; \quad (2.87)$$

$$w(r, z, t) = \frac{1}{\rho(r, z, t)} \int_0^z \left(\frac{1}{r} \frac{\partial}{\partial r} (r \rho(r, z', t) u(r, z', t)) - \frac{\partial \rho(r, z', t)}{\partial t} \right) dz'. \quad (2.88)$$

Furthermore, the evolution equations for $h(r, t)$, $\Gamma(r, t)$ and $\psi(r, t)$ become:

$$\frac{\partial h}{\partial t} = \frac{1}{\rho|_{z=h}} \left(-\frac{1}{r} \frac{\partial}{\partial r} \int_0^h r \rho u dz - \int_0^h \frac{\partial \rho}{\partial t} dz \right) + w_e; \quad (2.89)$$

$$\frac{\partial \Gamma}{\partial t} = -\vec{\nabla}_s \cdot (\Gamma \vec{u}_t) - \Gamma U_n \vec{\nabla}_s \cdot \vec{n} + D_\Gamma \vec{\nabla}_s^2 \Gamma + \frac{\partial h}{\partial t} \frac{\partial_r h}{1 + (\partial_r h)^2} \frac{\partial \Gamma}{\partial r}; \quad (2.90)$$

$$\frac{\partial \psi}{\partial t} = \frac{1}{r} \frac{\partial}{\partial r} \left(-\frac{r \psi}{h} \int_0^h u dz + D_\phi r h \frac{\partial \phi}{\partial r} \right). \quad (2.91)$$

For lower and intermediate concentrations these equations can be used as they are given, but for concentrations closer to the maximum packing fraction $y_{s,max}$ additional amendments should be implemented. This will be considered in more depth in Chapter 6.

2.9. Solution procedure

The dependent variables in the droplet (drop height $h(r, t)$, interfacial surfactant concentration $\Gamma(r, t)$, bulk surfactant concentration $\psi(r, t)$ and micelle concentration $\zeta(r, t)$) are to be solved as functions of the independent variables radial coordinate r and time t . In order to do this, the system of equations is discretized and solved numerically. The dependent variables are defined on a staggered grid and the spatial discretization of the derivatives is done with a central difference scheme. The temporal discretization is done by a diagonally implicit Runge-Kutta scheme, which solves each time step in three stages. Within each stage, the dependent variables are calculated at the new time step by solving the equation:

$$\vec{G}^{(i+1)} = \vec{W}^{(i+1)} - \vec{W}^{(i)} - \Delta t_{stage} \vec{f}^{(i+1)} = 0, \quad (2.92)$$

where \vec{W} denotes the vector of dependent variables, Δt_{stage} the time step of the current stage and \vec{f} the vector of time-derivatives of the dependent variables. The superscripts indicate the discretized time step on which the quantities are calculated. $\vec{W}^{(i+1)}$ is then solved by means of Newton's method:

$$\vec{W}_{(j+1)} = \vec{W}_{(j)} - J_{\vec{G}_{(j)}}^{-1} \vec{G}_{(j)}, \quad (2.93)$$

where $J_{\vec{G}}$ is the Jacobian matrix of \vec{G} with respect to \vec{W} . The subscripts denote the iteration number of the scheme.

The evaporation rate is obtained by solving the vapor field as given by Equation (2.57). This equation can be solved by using the multigrid algorithm as described by Shapira [159] (see Chapter 3) or by numerically solving the integral in Equation (2.71) (see Chapters 4 and 6).

In the porous medium, there are three dependent variables that are to be solved as functions of spatial coordinates r (and in some cases also z) and time t : wetted area height $h_p(r, t)$, bulk surfactant concentration $\phi_p(r, z, t)$ and adsorbed surfactant concentration $S(r, z, t)$. These are calculated explicitly on each substep of the Runge-Kutta scheme. In order to calculate the velocity field in the pores, that is necessary for the calculation of h_p and ϕ_p , it is required to first find the pressure field. This is also done with the multigrid algorithm described by Shapira [159].

In case there is a solute present (either $C(r, z, t)$ or $y_w(r, z, t)$ and $y_s(r, z, t)$, see Subsection 2.8), it is updated every substep of the Runge-Kutta scheme using a simple explicit Euler scheme. Subsequently, for $C(r, z, t)$ the concentrations in the bulk and of the adsorbed mass are updated explicitly. For $y_w(r, z, t)$ and $y_s(r, z, t)$ the fractions are normalized to add up to one every substep.

For the cases with a slipping contact line, it is required to take into account the additional dependent variable $R(t)$, besides $h(r, t)$, $\Gamma(r, t)$, $\psi(r, t)$ and $\zeta(r, t)$. Then, R is added to \vec{W} and its time derivative to $\vec{f}^{(i+1)}$. Because $0 \leq r \leq R(t)$, the physical domain is mapped on a fixed computational domain $0 \leq r^* \leq 1$ defined as:

$$r^* = \frac{r}{R(t)}. \quad (2.94)$$

The evolution equations are then rewritten in terms of this new variable and become:

$$\left(\frac{\partial h}{\partial t}\right)_{r^*} = \left(\frac{\partial h}{\partial t}\right)_r + \frac{r^*}{R} \frac{\partial h}{\partial r^*} \frac{\partial R}{\partial t}; \quad (2.95)$$

$$\left(\frac{\partial \Gamma}{\partial t}\right)_{r^*} = \left(\frac{\partial \Gamma}{\partial t}\right)_r + \frac{\Gamma}{R} \left(\frac{(\partial_r h)^2}{1 + (\partial_r h)^2} - 2 \right) \frac{\partial R}{\partial t}; \quad (2.96)$$

$$\left(\frac{\partial \psi}{\partial t}\right)_{r^*} = \left(\frac{\partial \psi}{\partial t}\right)_r - 2 \frac{\psi}{R} \frac{\partial R}{\partial t}; \quad (2.97)$$

$$\left(\frac{\partial \zeta}{\partial t}\right)_{r^*} = \left(\frac{\partial \zeta}{\partial t}\right)_r - 2 \frac{\zeta}{R} \frac{\partial R}{\partial t}. \quad (2.98)$$

The second term in Equation (2.96) arises from the deformation of the interface on which Γ is defined. Realizing that on any infinitesimal interface patch the surfactant concentration is given by $\Gamma = \frac{N}{2\pi r dr \sqrt{1+(\partial_r h)^2}}$, with N the local number of moles of surfactant, allows one to derive this term. The second terms in Equations (2.97) and (2.98) are derived in a similar way, but without the effect of interface deformation, given that these are bulk quantities.

Equations (2.95) to (2.98) can be solved with the same method as without a slipping contact line.

3. Evaporation of droplets with insoluble surfactants

In this chapter¹ the effect of insoluble surfactants on evaporating droplets is considered. Using two different contact line models it is analyzed how the contact line dynamics change for a droplet if surfactants are added. The two contact line models are compared both quantitatively and qualitatively to each other and to experimental literature.

3.1. Introduction

Sessile droplets are a common phenomenon. It can rightly be said that these droplets are encountered in a broad spectrum of contexts, ranging from everyday situations, as raindrops on a window and coffee spilled over a table, to high-tech applications, as inkjet printing [44] and spray cooling [89]. Especially the technological significance of sessile droplets has aroused a widespread interest in the subject. Increasingly detailed experiments and models have allowed for a much better understanding of the physical behavior of droplets in many configurations and on different scales. However, several challenges and questions still remain, which require continued research.

One topic that is still actively investigated is the drying of sessile droplets. This drying process is typically controlled by the diffusion of vapor from the droplet interface to the environment, as was demonstrated by Deegan et al. [35, 37] and Popov [142]. As a result, a nonuniform evaporation rate is induced, with a singularity at the contact line if the contact angle is small. The wetting behavior of sessile droplets can be divided into partial wetting, for which the droplet has an associated equilibrium contact angle [171], and complete wetting, for which no equilibrium contact angle exists, which results in indefinite spreading of the droplet [50]. Grounded on these principles, numerous analytical and numerical studies have been carried out [7, 71, 148].

During evaporation, the contact line typically shows two different types of behavior: either the contact angle decreases while the contact line remains pinned or the contact line moves while the contact angle remains constant. Also, a combination of these two types can occur in the form of stick-slip behavior [186]. Pinning of the contact line can occur if the contact angle is small or if the substrate is relatively rough. This is the case in many practical applications [32, 36, 55]. Constant contact angle evaporation on the other hand, typically occurs if the substrate is smooth or the contact angle is large. Both modes of evaporation can be modelled with hydrodynamic equations, but if the contact line moves an additional description of the nanometer scale around the contact line is required to resolve the contact line singularity [74].

One possible way of dealing with the contact line singularity is by assuming a slip

¹This chapter is based on the article: ‘The evaporation of surfactant-laden droplets: a comparison between contact line models’ by van Gaalen et al. [58]

length, that allows for some flow parallel to the substrate [21, 28, 110]. This is both experimentally and numerically a well established method, but a drawback is that it only introduces a length scale and not an energy scale that describes the interaction with the substrate. Practically, this means that an additional boundary condition needs to be introduced for the microscopic contact angle to close the problem. This boundary condition is usually an equation that couples the contact line velocity to the contact angle. For more information on this subject, the reader is referred to the review by Snoeijer and Andreotti [168].

Another method of resolving the singularity is by introducing a precursor film that covers the substrate around the droplet. In that case, the contact line is defined on the free surface of the film, where slip is allowed, thus resolving the contact line singularity [61, 165, 171]. In order to keep the precursor film stable, a disjoining pressure is introduced, which accounts for the molecular interactions of the fluid with the substrate [38, 77, 141, 152]. An advantage of the precursor film model is that it effectively resolves the contact line singularity without the need for additional boundary conditions. A disadvantage however, is that precursor films are rarely encountered under partial wetting conditions [68, 137, 168].

Given these two contact line models, it is considered of interest to compare them in the context of evaporating droplets to see whether both models give rise to similar results. While some studies exist that compare these two models (e.g. [43, 151, 162] in the context of spreading and [104] for a flow driven by a surface tension gradient), a comparison has never been made for evaporating droplets. Depending on the outcome, such a comparison is relevant since it guides researchers in making a substantiated decision with regard to the applicability of these models.

Furthermore, besides comparing the two contact line models for pure droplets, it is also relevant to compare the models with the inclusion of insoluble surfactants. Surfactants decrease the local surface tension of an interface. In principle, all surfactants are to some extent soluble, which implies that there exists a surfactant concentration both at the free surface and in the bulk of the liquid. Between these concentrations surfactant is transferred through adsorption and desorption. However, for many practically relevant surfactants the bulk solubility is very small (e.g. oleic acid in water [47, 182]). For these surfactants the bulk concentration can be disregarded in which case one speaks of ‘insoluble surfactants’ [6].

While several numerical studies exist that consider pure, volatile droplet dynamics (e.g. [39, 165]) or the dynamics of nonvolatile droplets and surfactants (e.g. [11, 48, 188]), numerical studies that analyze both the evolution of evaporating droplets and surfactants are less common. This is only done in the work of Karapetsas et al. [86], who model the evaporation of a complete wetting droplet with insoluble surfactants. Thus, it is of great relevance to analyze the evaporation of surfactant-laden droplets under partial wetting conditions, especially given the wide application of surfactants.

In the present work, a comparison is made between the precursor film model and slip length model in the context of evaporating sessile droplets with insoluble surfactants. For both pure droplets and droplets with insoluble surfactants the volume, radial and contact angle evolution calculated by both models is analyzed and compared.

Also, both models are quantitatively compared with experiments for pure droplets (i.e. droplets without surfactants) and checked for consistency with experiments for droplets with insoluble surfactants.

It is hypothesized that for pure droplets both the precursor film model and slip model will yield similar results, because both involve evaporation with a mostly constant contact angle. Furthermore, it is expected that during the evaporation of surfactant-laden droplets the surfactant concentration will increase as a result of the decreasing interfacial area. This will decrease the contact angle as the surface tension decreases with increasing concentration. Because of the inherent dissimilarities in interface definitions between the models, it is foreseen that the degree with which the surfactant concentration increases differs per model.

This article is organized as follows: first, in Section 3.2 the applied numerical method is presented, which is based on lubrication theory. The droplet height evolution equation and interfacial surfactant transport equation are introduced and an evaporation model is derived. Extra attention is paid to the formulation of the involved pressure terms and to the boundary conditions in the slip length model. After that, in Section 3.3 the results of the numerical simulations are shown and the effects of both models on the volume, radial and contact angle evolution are analyzed and compared. In the final section, conclusions are drawn based on the found results.

3.2. Mathematical model

In this section the mathematical equations are introduced that model the evaporating droplet. First, the evolution of the height profile is presented and described and after that the convection-diffusion equation for the surfactants at the interface. Subsequently, a separate subsection is dedicated to the formulation of the pressure terms in the system, including the disjoining pressure that is related to the precursor film. Lastly, the slip model is outlined and the evaporation model is explained.

3.2.1. Lubrication equation

A sessile droplet is considered with mass density ρ , dynamic viscosity μ and (liquid-gas) surface tension σ_{lg} . For this study, only droplets much smaller than the capillary length $l_\sigma = (\sigma_{lg}/\rho g)^{1/2}$ are regarded. Therefore, the influence of gravity g can safely be neglected [61, 167]. Another consequence of the small length scales involved is a low Reynolds number. This results in a viscous flow where the inertia terms can be neglected. Lastly, cylindrical coordinates (r, α, z) are used with the assumption of axisymmetry ($\frac{\partial}{\partial \alpha} = 0$) and no swirl ($U_\alpha = 0$) and, most importantly, ‘flat’ droplets are assumed, which allows one to express the evolution equation of drop height $h(r, t)$ as a function of r :

$$\frac{\partial h}{\partial t} = \frac{1}{r\mu} \frac{\partial}{\partial r} \left(\frac{rh^3}{3} \frac{\partial p}{\partial r} - \frac{rh^2}{2} \frac{\partial \sigma_{lg}}{\partial r} \right) + w_e. \quad (3.1)$$

Here, p is the excess pressure in the droplet and w_e is defined as the height change rate due to evaporation. Both these parameters will be quantified later on, in Sub-

section 3.2.3 and Subsection 3.2.5, respectively. In the evolution equation, a pressure driven term can be recognized and a term driven by the surface tension gradient, which accounts for the Marangoni effect [153]. For a derivation of Equation (3.1), see Subsection S.1.1.

The boundary and initial conditions that $h(r, t)$ is subjected to are given by:

$$\left(\frac{\partial h}{\partial r}\right)_{r=0} = 0, \quad (3.2)$$

$$\left(\frac{\partial^3 h}{\partial r^3}\right)_{r=0} = 0, \quad (3.3)$$

$$h(R, t) = 0, \quad (3.4)$$

$$h(r, 0) = h_0(r). \quad (3.5)$$

Here, R is the radius of the droplet and h_0 is the initial droplet profile, which is obtained by setting $w_e = 0$ and relaxing the droplet to an equilibrium solution.

3.2.2. Surfactant transport equation

The evolution equation of the local surfactant concentration $\Gamma(r, t)$ can be expressed in radial coordinates as:

$$\frac{\partial \Gamma}{\partial t} = -\frac{1}{r} \frac{\partial(rU_t \Gamma)}{\partial s} + \frac{\Gamma \partial_t h}{1 + (\partial_r h)^2} \left(\frac{\partial^2 h}{\partial r^2} + \frac{1}{r} \frac{\partial h}{\partial r} \right) + \frac{D_s}{r} \frac{\partial(r \partial_s \Gamma)}{\partial s} + \frac{\partial h}{\partial t} \frac{\partial_r h}{1 + (\partial_r h)^2} \frac{\partial \Gamma}{\partial r}. \quad (3.6)$$

Here, U_t is the fluid velocity tangential to the liquid-air interface and D_s the surface diffusion coefficient. Furthermore, $\frac{\partial}{\partial s}$ denotes the partial derivative tangential to the interface in radial direction. The first term on the right-hand side accounts for convective transport tangential to the interface, the second term is a source-like term that takes into account deformation of the interface, the third term is a diffusion term and the last term compensates for the displacement of the surface coordinates that move along the normal of the surface. A derivation of Equation (3.6) is given in Section S.2.

Surfactant concentration $\Gamma(r, t)$ is subject to the following boundary and initial conditions:

$$\left(\frac{\partial \Gamma}{\partial r}\right)_{r=0} = 0, \quad (3.7)$$

$$\left(\frac{\partial \Gamma}{\partial r}\right)_{r=D} = 0, \quad (3.8)$$

$$\Gamma(r, 0) = \Gamma_0(r). \quad (3.9)$$

Here, D denotes the domain boundary for the surfactant, which is where $\partial_r h \approx 0$ for the precursor film model and $D = R$ for the slip model.

The surface tension equation of state used in this present work, is the dilute limit relation given by

$$\sigma_{lg} = \sigma_0 - \sigma_\Gamma \Gamma. \quad (3.10)$$

In this relation σ_Γ is the ‘efficiency’ of the surfactant which is defined as $\sigma_\Gamma = R_u T$ with R_u the universal gas constant and T the temperature.

3.2.3. Disjoining pressure and precursor film

The pressure p in the droplet is given by Derjaguin’s equation [38, 165, 170]:

$$p = p_L - \Pi, \quad (3.11)$$

where p_L is the Laplace pressure and Π the disjoining pressure. Both these pressure terms are independent of z , which is in accordance with Equation (S.4). The Laplace pressure is given by

$$p_L = -\frac{1}{r} \frac{\partial}{\partial r} \left(\sigma_{lg} \frac{r \partial_r h}{\sqrt{1 + (\partial_r h)^2}} \right). \quad (3.12)$$

Contrary to the traditional formulation of the Laplace pressure, surface tension σ_{lg} is also part of the derivative in Equation (3.12), rather than that it is written outside the brackets. This is because σ_{lg} depends on the local surfactant concentration and thus it depends on r . As shown by Thiele et al. [178] the surface tension is required to be part of the radial derivative in that case. Disjoining pressure Π is in this model given by

$$\Pi = B \left(\left(\frac{h_s}{h} \right)^n - \left(\frac{h_s}{h} \right)^m \right). \quad (3.13)$$

Here, B , n and m are positive constants (with $n > m$) and h_s is the precursor film height for which Π equals zero. The height h_s does not necessarily correspond to the real precursor film height, but only represents the zero-pressure height.

This formulation of the disjoining pressure consists of an attractive and a repulsive component ($B(h_s/h)^m$ and $B(h_s/h)^n$ respectively), corresponding to the attractive and repulsive molecular forces that govern the physics of the precursor film [152]. In literature, one often encounters disjoining pressure formulations that only include the attractive forces (see e.g. Karapetsas et al. [86]). In these cases the droplet will spread indefinitely, because there is no equilibrium contact angle corresponding to this formulation as shown by Starov and Velarde [171].

In this work, n and m are chosen to be 5 and 4 respectively. Higher values of n and m would require a finer grid without any significant changes in the drop profile, while lower values of n and m would cause significant deviations in the drop profile from the spherical cap shape. The value of B can be related to the equilibrium contact angle θ_e , which is elaborated in Section S.3.

3.2.4. Slip length model

Another way of solving the contact line singularity is by assuming a slip length (see e.g. [21]). The height evolution equation given by Equation (3.1) then becomes:

$$\frac{\partial h}{\partial t} = \frac{1}{r\mu} \frac{\partial}{\partial r} \left[r \left(\frac{h^3}{3} + \beta h^2 \right) \frac{\partial p}{\partial r} - r \left(\frac{h^2}{2} + \beta h \right) \frac{\partial \sigma_{lg}}{\partial r} \right] + w_e. \quad (3.14)$$

with β the slip length. For a derivation of Equation (3.14) see Subsection S.1.2. The introduction of β does remove the moving contact line singularity, but still requires a complementary constitutive relation that prescribes the contact line velocity [168]. In this study, the contact line velocity is obtained by means of the relation:

$$\frac{dR}{dt} = k(\theta - \theta_e)^a. \quad (3.15)$$

Here, θ is the current contact angle, a a power-law index with a range of 1-3 and k a typical sensitivity of the contact line position to deviations of the contact angle from equilibrium with the dimension of velocity. Increasing a typically results in a less constant contact angle during evaporation, since $\theta - \theta_e$ is generally smaller than unity (the units are radians). An increase of k results in a more constant contact angle, since the radius will respond faster to any deviations from θ_e . In this work, a is set to 1 and k is set to 1.3×10^{-5} m/s. These values are empirically determined by comparison with experimental data from Nguyen et al. [131]. This data is also used for validation of the numerical models in Subsection 3.3.1. Note that for small deviations from the equilibrium contact angle, Equation (3.15) with $a = 1$ is in agreement with the Cox-Voinov law.

The current contact angle θ can be calculated from the slope $\partial_r h$ at the contact line and, in case of surfactants, θ_e can be computed by means of Young's equation:

$$\theta = \cos^{-1} \left(\frac{1}{\sqrt{1 + (\partial_r h|_R)^2}} \right), \quad (3.16)$$

$$\theta_e = \cos^{-1} \left(\frac{\sigma_{lg}[\Gamma(R, 0)]}{\sigma_{lg}[\Gamma(R, t)]} \cos(\theta_0) \right). \quad (3.17)$$

Here, θ_0 is the initial contact angle.

3.2.5. Evaporation model

The evaporative mass flux of water \dot{m}_w is given by:

$$\dot{m}_w = - \frac{D_{wa} M_w p_{sat,w}}{R_u T} \frac{\partial \hat{p}_w}{\partial n}, \quad (3.18)$$

with D_{wa} the water vapor diffusivity in air [93], M_w the molar mass, $p_{sat,w}$ the homogeneous saturation pressure, which is assumed to be constant, and $\hat{p}_w = \frac{p_w}{p_{sat,w}}$ with p_w the local vapor pressure [39].

Regarding the vapor field, Deegan et al, [37] and Hu and Larson [70] showed that the vapor diffusion for single component droplets can be considered as instantaneous. Combined with the assumption of no air flow, this results in the following Laplace equation:

$$\nabla^2 \hat{p}_w = 0. \quad (3.19)$$

The corresponding boundary conditions of Equation (3.19) are:

$$\hat{p}_w|_{z=h} = 1 \quad \text{for } r < R; \quad (3.20)$$

$$\frac{\partial \hat{p}_w}{\partial z} \Big|_{z=0} = 0 \quad \text{for } r > R; \quad (3.21)$$

$$\hat{p}_w = RH_w \quad \text{for } (r, z) \rightarrow \infty. \quad (3.22)$$

Equation (3.20) represents the saturated vapor at the liquid-air interface, Equation (3.21) the prohibition of vapor penetration in the substrate and Equation (3.22) the relative humidity in the surroundings (where RH_w is the relative humidity). For the precursor film model, the radial coordinate corresponding to R is defined to be the point where $h = 1.2h_s$, which results in the droplet having approximately the same effective radius as if it would have been a spherical cap.

The evaporation velocity w_e in Equation (3.1) can subsequently be calculated by:

$$w_e = -\frac{\dot{m}_w}{\rho} \sqrt{1 + \left(\frac{\partial h}{\partial r}\right)^2}. \quad (3.23)$$

Similarly to Equation (3.12), the argument of the square root makes the expression a good approximation for higher slopes than it would when approximated as unity. An elaboration of the numerical method is given in Section 2.9.

3.3. Results and discussion

In this section the numerical results are shown and discussed. First, both the precursor film model and slip length model are compared to experimental results, all for pure water droplets. After that, the effects of insoluble surfactants on the results of these two cases are investigated and explained.

3.3.1. Pure droplets

First, the case of pure droplets is investigated. Simulations are carried out for 1.45 microliter water droplets. Furthermore, all physical properties of water are taken at 25°C and the relative humidity $RH_w = 0.55$. These parameters are chosen in order to compare the simulations with the experiments that were performed by Nguyen et al. [131]. They carried out experiments for water droplets on an atomically smooth Oct-Silicon substrate and published data both in the pinned contact line regime and constant contact angle regime. Precursor film height h_s is set equal to the height of one grid cell ($\approx 9.4 \mu\text{m}$) and slip length $\beta = 100 \text{ nm}$. Although physical values of these two parameters tend to be smaller, simulations and literature show that any smaller values result in negligible changes in the solution, but require a finer grid [165].

The initial contact angle was set at $\theta_0 = 35.0^\circ$ for both models. This yielded nearly identical height profiles as can be seen in Figure 3.1a ($\theta_0 = 31.5^\circ$ will be discussed later). For the precursor film model, the contact angle is defined as the contact angle of a spherical cap with the same height and volume (after subtraction of the volume of the precursor film). Calculating the contact angle directly from the height profile, for example from the highest slope, would result in an underestimation of the effective contact angle, since the drop blends into the precursor film around R .

As can be seen in Figure 3.2 both the precursor film model and the slip length model agree rather well with each other and with the experiments. The differences between both models are minute in terms of volumetric evolution and radial evolution and the dissimilarities that can be observed are likely caused by the fact that both models give slightly different drop shapes during evaporation. In Figure 3.1b it is shown that at $t = 600$ s the slip length model yields a flatter, lower contact angle drop than the precursor film model. This behavior can also be observed in Figure 3.2, especially in the contact angle evolution. The precursor film model predicts a nearly constant contact angle that only decreases at the end of the drying process, while the slip length model also predicts an initial decrease. This initial decrease can be explained by Equation (3.15), which shows that the change in R is proportional to the deviation from θ_e . As a result, the contact angle will keep decreasing due to evaporation, until $\partial_t R$ is large enough to maintain a quasi-steady, receding contact angle. This initial decrease in contact angle is also observed in the experiments.

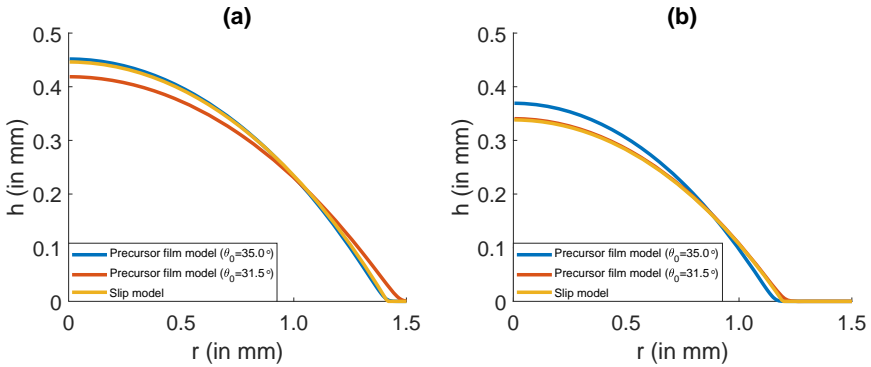


Figure 3.1.: Drop profile at (a) $t = 0$ s and (b) $t = 600$ s.

Compared with the experiments, two discrepancies can be distinguished in the volume evolution. Firstly, at the start the experimental results show a slight deviation from the model results. This deviation can be attributed to the transition between the pinned contact line regime, which occurs in the experiments before the initial time of the simulations and is not shown in the figure, and the moving contact line regime, which is actually shown in the figure. Because the radius is nearly constant during the transition, the evaporation occurs faster than it would for a moving contact line. The slip length model partially captures this effect, as can be seen in Figure 3.2c, but the precursor film model has a nearly constant contact angle until the end of the drying process. Therefore, more comparable results would be obtained for the precursor film model if the initial contact angle is set equal to the receding contact angle that is observed in the experiments ($\approx 31.5^\circ$). Therefore, it is decided to use $\theta_0 = 31.5^\circ$ for the precursor film model to obtain more representative and comparable results. This will cause the drop profiles to deviate in the beginning of the evaporation process, as can be seen in Figure 3.1a, but they will be more similar at later stages, as illustrated in Figure 3.1b.

The second discrepancy between the models and experiments can be seen at the end of the drying process (around $t = 1000$ s), where the experiments again show non-linear behavior. This nonlinear behavior can also be explained by the decrease of the

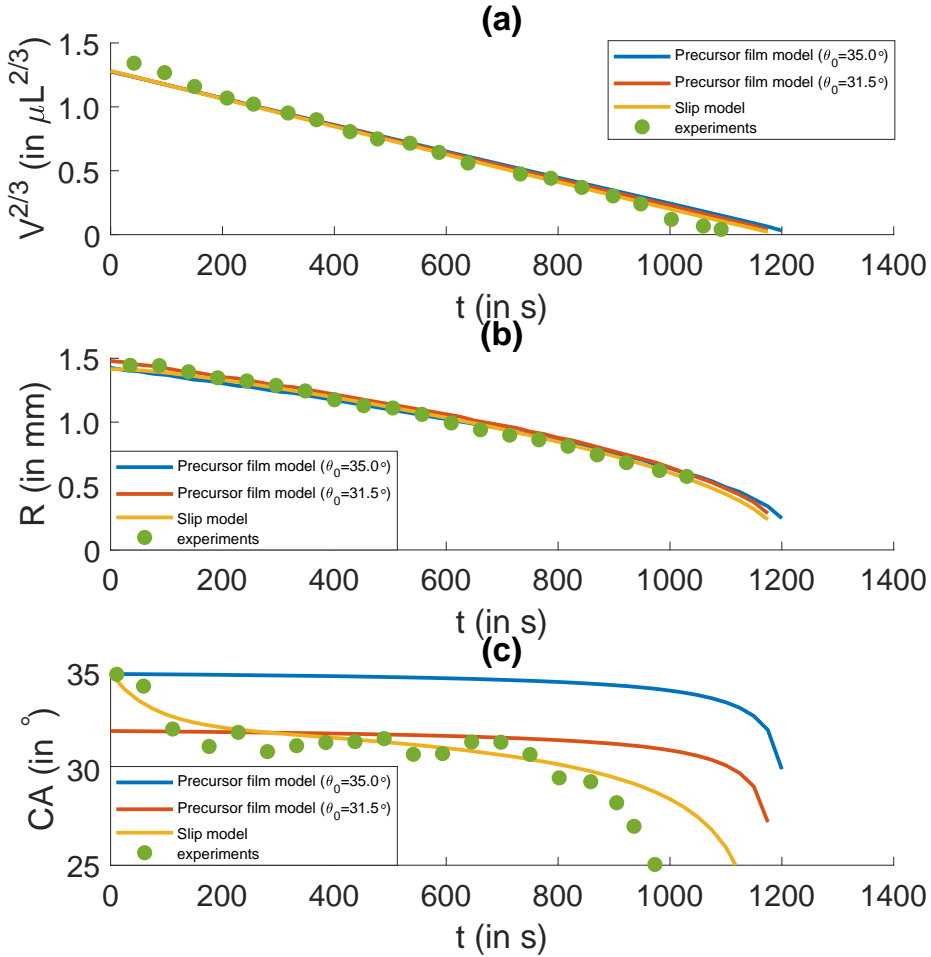


Figure 3.2.: Comparison of evaporation of a pure droplet with (a) droplet volume to the power 2/3 over time, (b) droplet radius over time and (c) contact angle over time. The experiments were performed by Nguyen et al. [131].

contact angle, which accelerates the drying process. Both models show qualitatively the same behavior, but predict that the contact angle is constant for a longer duration. Unfortunately, how large the difference in contact angle between the models and the experiments is after $t = 1000$ s cannot be said with certainty, since Nguyen et al. did not report any data for that time (probably because the contact angle measurements became increasingly less accurate when $\theta \rightarrow 0$).

In summary, it is concluded that both the precursor film model and the slip length model match the experiments reasonably, slightly favoring the slip model when it comes to contact angle evolution. Of course, it is duly noted that the agreement is

partly a result of fitting moving contact line parameters (n and m for the precursor film model, a and k for the slip model) to the experiments, as reported in Subsections 3.2.3 and 3.2.4.

3.3.2. Droplets with insoluble surfactants

In the previous subsection a pure water droplet was considered for a precursor film model and a slip length model. However, many applications involve surfactants, either intentionally or in the form of impurities. Therefore, in this subsection sessile droplets with insoluble surfactants are studied and again the two contact line models are compared.

Simulations are carried out for several initial surfactant concentrations Γ_0 , ranging from 1.0×10^{-7} to 5.0×10^{-6} mol/m². Surfactant efficiency $\sigma_\Gamma = R_u T$ is set to 2.48 kJ/mol, which corresponds to a temperature of 25°C, and surface diffusion coefficient D_s is set to 4.33×10^{-10} m²/s, which corresponds to 2D Einsteinian diffusion of a molecule with an effective radius of five times the Van der Waals radius of a carbon atom (850 pm) [52]. All simulated droplets have the same initial equilibrium contact angle (35.0° for the slip length model and 31.5° for the precursor film model), regardless of the initial surfactant concentration.

In Figure 3.3, it can be observed that for the slip length model the addition of surfactants has a significant influence on the drop evolution. Higher concentrations result in a shorter drying time (see Figure 3.3a), which is caused by the fact that the equilibrium contact angle decreases as the surfactant concentration increases due to the shrinking interface. This also results in apparent contact line pinning, as can be seen in the radial evolution: any evaporated volume results in an increased surfactant concentration, which subsequently reduces the contact angle accordingly, while keeping the radius nearly constant. Thus, it can be seen that for higher initial surfactant concentrations the contact angle decreases at a higher rate, while the radius tends to be more constant. This also causes a relatively higher concentration increase for the lower initial concentrations, since there the interfacial area shrinks faster due to the decreasing radius.

This ‘quasi-pinning’ behavior is consistent with results found in literature. As reported by Truskett and Stebe [183], pinning behavior is strongly promoted with the addition of surfactants. While this increased pinning can also be attributed to the fact that surfactants decrease the initial contact angle, which promotes pinning as well, the quasi-pinning observed in the simulations can be an additional relevant mechanism. Similar results have been reported for soluble surfactants by Dugas et al. [46], who show improved pinning by surfactants, and by Sefiane [154], who, besides increased pinning, also shows a decrease in contact line retraction rate with the addition of surfactants. Both these results are also consistent with the quasi-pinning behavior observed in the simulations, because the mechanism is essentially the same for soluble surfactants: a reduction in available space for surfactants results in a concentration increase, which subsequently results in a further reduced equilibrium contact angle.

The occurrence of quasi-pinning is also predicted by Semenov et al. [156]. They show both experimentally and analytically that the volume evolution of evaporating,

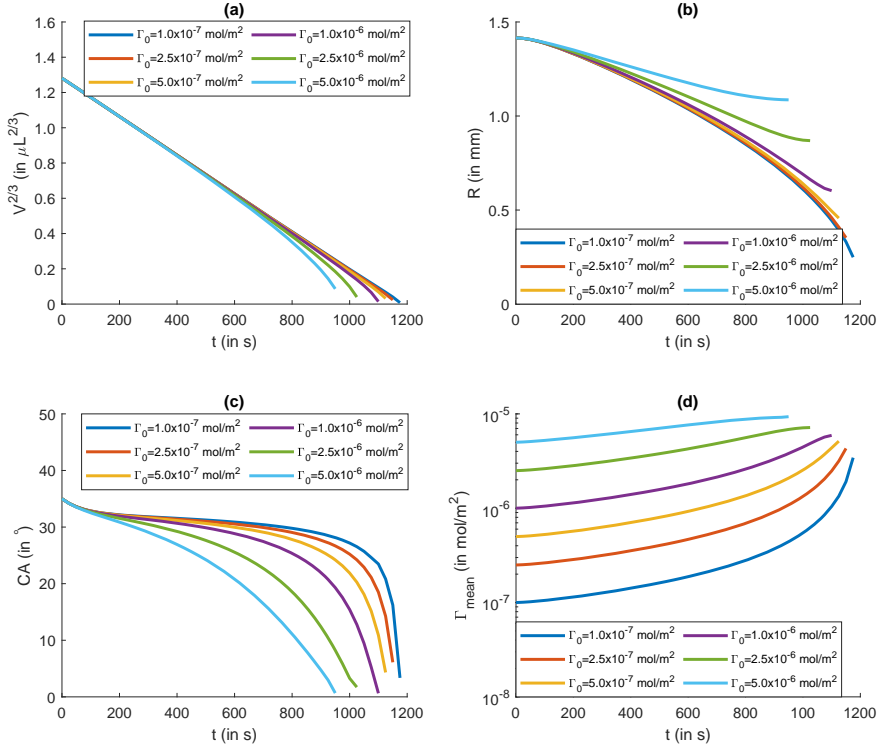


Figure 3.3.: Drop evolution of the slip model for different initial surfactant concentrations, with (a) the volume evolution, (b) the evolution of the drop radius, (c) the contact angle evolution and (d) the area-averaged surfactant concentration.

surfactant-laden droplets scales as $V^{2/3} \sim t$ for contact angles higher than approximately 45° , and predict that it accelerates for contact angles lower than 45° .

As a side note, it is not taken into account here that surfactants might also inhibit evaporation (e.g. as observed by [126], while not observed by [183]). However, this would only affect the time scale. The observed quasi-pinning of the contact line will not be affected by including a reduced evaporation rate, since the pinning is a result of the equilibrium contact angle being reduced by the increased surfactant concentration.

Another relevant observation is that in none of the simulations the typical circulating flow occurs, that is often caused by the Marangoni effect (e.g. see Figure 3.4a. Note that it is possible to model flow circulations with lubrication theory despite the small contact angle assumption [91]). In first instance, this may seem counterintuitive given the frequency with which surfactant-induced Marangoni vortices are reported in literature (e.g. see [42]). However, we will show that, in this case, the occurrence of a Marangoni vortex is physically impossible, regardless of the initial surfactant con-

centration.

The argument is the following. Given that evaporation is strongest at the contact line, there will be a higher curvature at the apex compared to the contact line. The corresponding pressure gradient causes the typical outward, ‘coffee-ring’ flow [30, 31]. Furthermore, because of the same curvature effect, the surfactant concentration increases most rapidly at the drop apex. This source-like effect is a direct result of the second term on the right-hand side of Equation (3.6). The movement of the contact line does not change this effect, as implied by Equation (S.25). Thus, the surfactant concentration at the apex can never be smaller than at the contact line due to shrinkage of the interface, although a positive concentration gradient towards the contact line is required for a circulating flow.

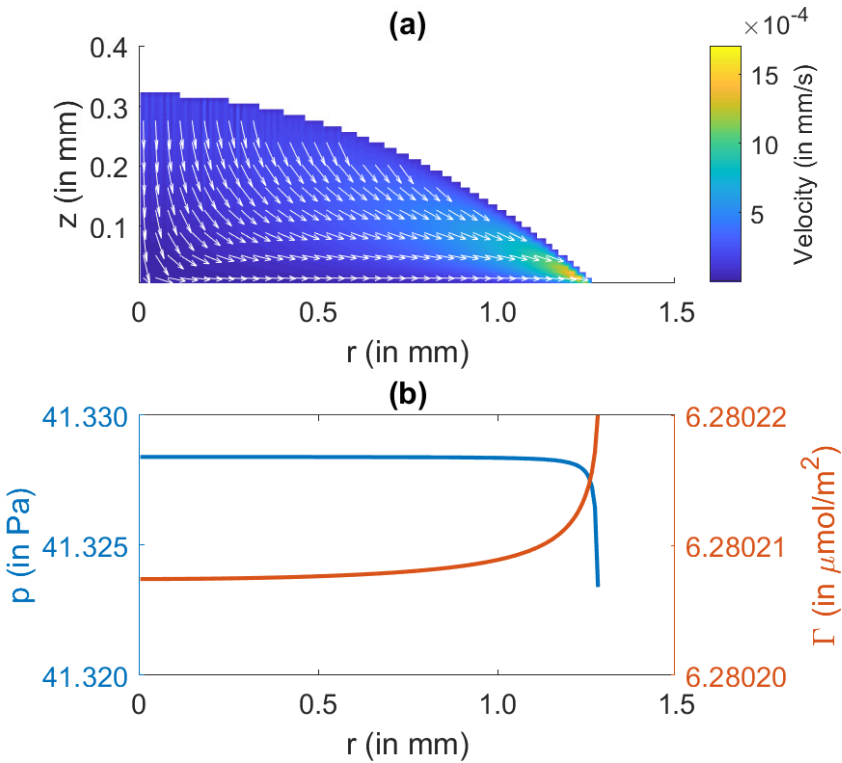


Figure 3.4.: Typical flow properties during evaporation ($\Gamma_0 = 5.0 \times 10^{-6} \text{ mol/m}^2$ and $t = 350 \text{ s}$), with (a) the flow field and (b) the pressure profile and surfactant distribution.

Thus, for Marangoni vortices to occur the required surface tension gradient should be caused by convective transport effects. If any surfactant is transported towards the contact line by the coffee-ring flow, a negative surface tension gradient could arise. However, this surface tension gradient can never be sufficient to cause a circulating flow, because as soon as it would be large enough for a negative interfacial velocity, it would cancel the outward flow at the interface. Subsequently, without an outward

flow, the concentration at the contact line will not increase anymore. Thus, it can be concluded that the surfactant tends to reduce the interfacial flow, but it can never cause a Marangoni vortex. Figure 3.4b is consistent with this conclusion: the negative pressure gradient induces an outward flow that is partly diminished due to the resulting concentration gradient.

For Marangoni vortices to occur, other physical effects need to be taken into account. For example, if the surfactant is soluble, it can also be transported through the bulk rather than only along the interface. Thus, circulations can then be caused by surfactant continuously flowing through the bulk towards the contact line, adsorbing at the interface, flowing along the interface towards the drop apex and desorbing into the bulk. Alternatively, if an additional driving force is involved, like spreading, circulations can occur with insoluble surfactants [86]. Lastly, temperature effects and other solutal effects can also cause Marangoni vortices [39].

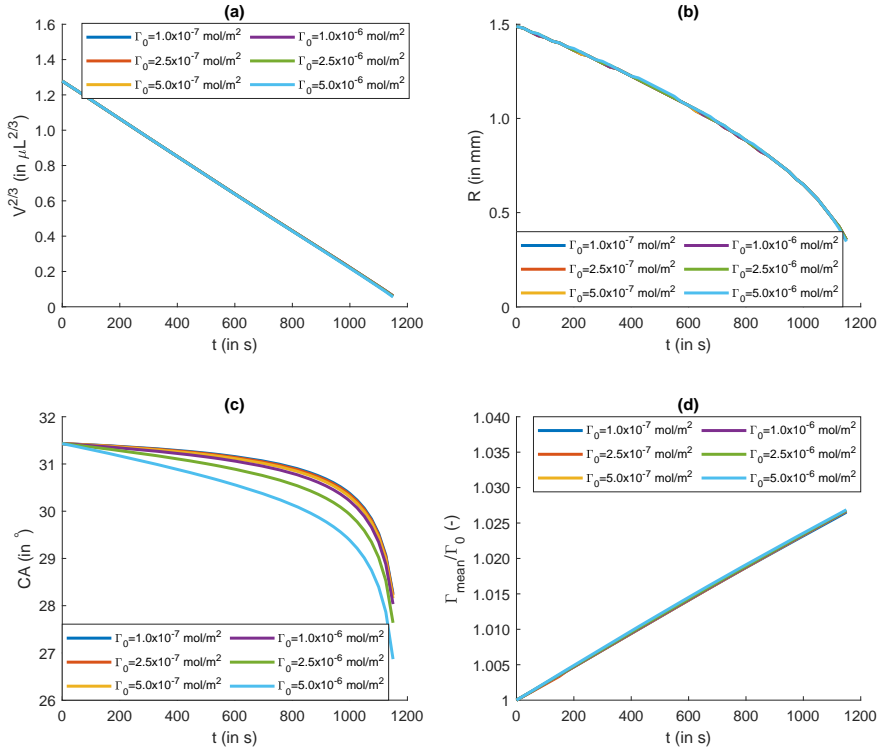


Figure 3.5.: Drop evolution of the precursor film model for different initial surfactant concentrations, with (a) the volume evolution, (b) the evolution of the drop radius, (c) the contact angle evolution and (d) the area-averaged surfactant concentration.

When observing the drop evolution as predicted by the precursor film model (Figure 3.5), a major flaw of this model is revealed. Addition of surfactants has effectively no

effect on the volume and radial evolution and higher surfactant concentrations hardly reduce the contact angle during evaporation. This is caused by the fact that the droplet is not well defined in the precursor film model and therefore there is no mechanism to keep the surfactant from flowing into the precursor film. Therefore, while the droplet shrinks, surfactant is either left behind in the precursor film or flows back into the precursor film to reduce the concentration gradient. This backflow gives rise to the tiny concentration increase that can be seen in Figure 3.5d.

This is not an issue that can easily be solved within the context of the precursor film model. An obvious way would be to introduce an artificial no-flux boundary condition at the same point where the evaporation is cut off. However, this only solves the problem of surfactant flowing out of the droplet, but does not cause the surfactant to move with the contact line. A more physical method would be to involve a penalty function that assigns a relatively high energetic cost to surfactant in the precursor film, for example as was done by Thiele et al. [180]. A major disadvantage of this method, however, is the resulting severe numerical instability. This makes penalty functions more suitable for equilibrium cases. An alternative strategy could be to introduce a source function that creates surfactant as the effective drop radius decreases. This would in principle solve the problem of too low concentration inside the droplet, but is of course highly unphysical.

In summary, the slip length model yields reasonable results that can be understood intuitively and are consistent with literature, while the precursor film model has some serious defects when surfactants are involved. Possibly, in future work methods will be derived that use disjoining pressure without precursor films as suggested by Colinet and Rednikov [29]. This would indeed solve the backflow problem associated with precursor films, but until then the slip length model is preferred.

3.4. Conclusion

A numerical model was developed using lubrication theory to simulate the evolution of evaporating droplets [9, 65, 136, 146]. Insoluble surfactants were included in the model by means of an interfacial convection-diffusion equation [139, 173, 178, 189]. In order to incorporate moving contact lines, both a precursor film model and a slip length model were implemented. For both models, the numerical results were compared to experimental results with pure liquids obtained by Nguyen et al. [131]. This showed reasonable agreement, slightly favoring the slip length model.

In case of insoluble surfactants, the slip length model showed that ‘quasi-pinning’ of the contact line can occur. This behavior is a direct result of the fact that a shrinking interface causes the surfactant concentration to increase, which subsequently reduces the equilibrium contact angle. Thus, at some point any evaporated volume results in a decreasing contact angle, effectively pinning the contact line. Quasi-pinning was found to be consistent with experimental results obtained by Truskett and Stebe [183], who show that insoluble surfactants promote pinning. Furthermore, similar experimental results were obtained for soluble surfactants by Dugas et al. [46] and by Sefiane [154]. The possibility of quasi-pinning was also inferred by Semenov et al. [156]. Besides quasi-pinning, it was also shown that surfactants tend to reduce

the bulk flow close to the interface, but will never cause the typical circulating flow pattern that is often observed when surfactants are involved.

The precursor film model, on the contrary, showed no significant differences in drop behavior with the inclusion of insoluble surfactants. This is a result of surfactant being left behind in the precursor film as the contact line moves and even surfactant flowing back from the droplet into the film. Several methods to counteract this unphysical behavior were discussed, but none are considered desirable or physical.

These results agree with the hypothesis that was made, namely that both contact line models would produce similar results for pure droplets, but different results when surfactants are included. Furthermore, the contact angle indeed decreases over time as surfactants are included, especially for higher initial concentrations.

From the perspective of progress and innovation the relevance of the findings is twofold. First, from the comparison between contact line models it is concluded that in the context of pure, evaporating, sessile droplets both models perform nearly equal, slightly favoring the slip length model in comparison with experiments. Furthermore, with the inclusion of surfactants the slip length model is preferable over the precursor film model given the current state of the art. Also, the pinning-like behavior exhibited by the surfactant-laden drop is of potential use as a mechanism for controlling the final drop radius in technologies such as inkjet printing, pesticide sprays, the fabrication of DNA/RNA microarrays and many more. This may be possible by fine tuning the initial surfactant concentration with regard to the desired final radius.

Previous comparisons between contact line models only included nonvolatile droplet dynamics [43, 104, 151, 162], so a numerical comparison for volatile droplets is a welcome addition to the existing literature, especially given the increasing interest in evaporating droplets with moving contact lines [39, 128, 165, 177]. Preceding numerical studies about surfactant dynamics mostly involved nonvolatile drops [10, 11, 21, 28, 48, 64, 79, 85, 188, 190, 191], while only one numerical study known to the authors considers both surfactant and volatile droplet dynamics (Karapetsas et al. [86]). Since the latter treats droplets under complete wetting conditions the results of the present work, which considers partial wetting conditions, can be seen as complementary.

Further research opportunities lie in the modeling of contact angle hysteresis. It is generally known that during evaporation, water droplets first tend to go through a pinned contact line regime until the contact angle equals a receding contact angle θ_r . Only then will the contact line start moving, while keeping a constant contact angle, until it passes through a third and final regime where both the contact radius and contact line decrease [131, 155]. In this work, only the latter two regimes are considered, so it may be of interest to modify the contact line models to include the pinning regime as well. For the slip length model, this can be done by setting $\partial R/\partial t = 0$ for $\theta > \theta_r$ and for the precursor film model, it might be possible to introduce a prefactor B that depends on θ . An illustration of drop evaporation with contact line hysteresis is shown in Figure 3.6. Surfactants could be included by making θ_r dependent on surfactant concentration Γ .

Regarding evaporating droplets with surfactants in general, a fitting next step is an extension of the model to soluble surfactants, micelles and adsorption on the substrate,

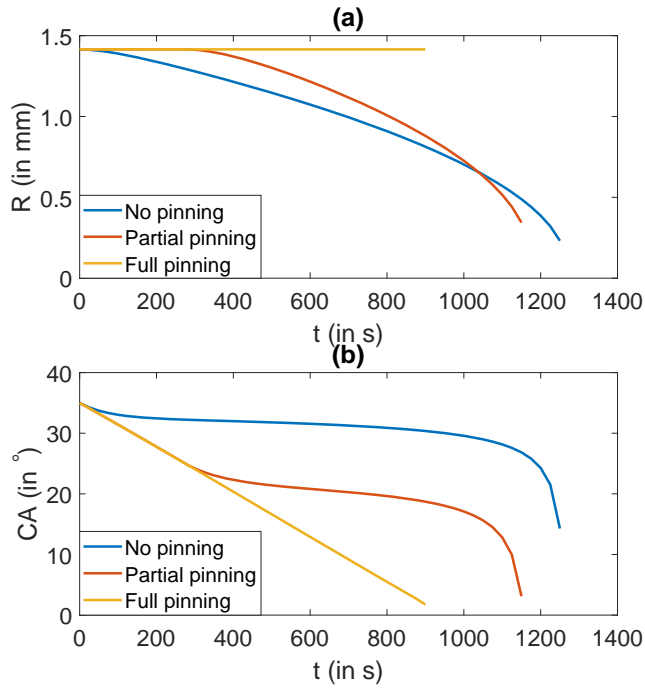


Figure 3.6.: Drop evolution for unpinned, partially pinned and completely pinned contact lines as given by the slip model. (a) is the evolution of the drop radius and (b) the contact angle evolution.

similar to the work of Karapetsas et al. [85]. This will render the models increasingly relevant and more open to comparison with experiments.

4. Flow in evaporating droplets with soluble surfactants

In this chapter¹ the effect of surfactants on the flow in evaporating droplets is examined. Surfactant-induced Marangoni flow can result in circulating flow patterns and in this chapter it is analyzed under what circumstances this flow type occurs. The results are compared qualitatively to literature and are used to explain certain experimental trends.

4.1. Introduction

The evaporation of sessile droplets is a phenomenon that has a broad practical relevance. From applications like spray cooling [89] and cleaning/drying of semiconductor surfaces [103] it can be seen that many modern technologies involve sessile droplets. In some technologies the aim is to leave a homogeneous deposition pattern of particles after evaporation of the volatile components from sessile droplets. Examples of this are inkjet printing [122, 138, 163], pesticide spraying [64, 69] and manufacturing DNA/protein microarray slides [46].

A common issue hindering the formation of a homogeneous deposition pattern is the occurrence of the coffee-stain effect: preferential evaporation at the contact line causes a strong, outward flow resulting in a ring-like deposition pattern (given a pinned contact line) [35, 36, 37]. Clearly, this coffee ring is the complete opposite of a homogeneous deposition pattern. Several methods of counteracting the coffee-ring effect can be found in literature (e.g. unpinned contact lines [165], oil menisci [106], ellipsoidal particles [194]) of which an important one is what is defined here as ‘Marangoni circulation’. A surface tension gradient results in an interfacial flow (the Marangoni effect), which – if the surface tension gradient is negative towards the contact line – can result in a circulating flow. This Marangoni vortex is able to suppress the coffee-stain effect [73, 112, 172].

The surface tension gradient required for Marangoni circulation to occur, can generally have two possible origins. First, the surface tension can become non-uniform due to thermal effects, such as evaporative cooling [150] or heated substrates [62, 161]. Second, the surface tension can become non-uniform as a result of non-homogeneous changes in composition. This happens for example during the drying of multicomponent droplets [39, 177] or droplets with surfactants [86, 115]. Although these causes are fairly well established, it cannot be predicted straight-forwardly whether Marangoni circulation will occur or not [53].

In this present work the focus lies on the occurrence of Marangoni circulation in evaporating droplets with soluble surfactants. It is hypothesized that using dimensionless

¹This chapter is based on the article: ‘Marangoni circulation in evaporating droplets in the presence of soluble surfactants’ by van Gaalen et al. [59]

numbers, regime plots can be composed that indicate whether Marangoni vortices can be expected or not. As a result, it may be possible to identify which parameters are relevant and what tuning they require to promote Marangoni circulation and hence a more homogeneous deposition pattern. This is done both below and above the critical micelle concentration (CMC), where surfactant monomers cluster and form micelles.

Previous numerical studies focused primarily on the evaporation of droplets without surfactants [39, 40, 41, 87, 165] or on the evolution of nonvolatile, surfactant-laden droplets [10, 11, 21, 28, 48, 64, 79, 85, 188, 191]. Only a few numerical studies combined evaporation and surfactants. Using lubrication theory, Van Gaalen et al. [58] and Karapetsas et al. [86] both considered evaporating droplets with insoluble surfactants under partial and complete wetting conditions, respectively. Furthermore, Jung et al. [82] studied the formation of coffee rings in evaporating droplets with soluble surfactants, using a lattice gas model. However, they did not consider the underlying fluid dynamics. The present work is the first numerical study to analyze the evolution of evaporating droplets with soluble surfactants. Besides, while the number of experimental studies on evaporating droplets with surfactants is growing [45, 46, 154, 156, 172, 183, 190], only limited actual flow visualisations have been made [115, 157]. In this respect, the numerical work presented here is a useful addition to the small number of flow visualisations.

Results are obtained by means of a numerical model based on lubrication theory. Here, by assuming a relatively thin droplet, the Navier-Stokes equations can be simplified into a 1D height evolution equation. By combining this evolution equation with surfactant transport equations at the interface and in the bulk, velocity profiles can be calculated. Counter-intuitively to what one would expect, lubrication theory is able to capture flow topologies, such as circulation, rather well [65, 121, 192]. This unexpected, empirical overperformance has mathematically been validated by Krechetnikov [91].

This article is organized as follows: first, in Section 4.2, the numerical model is presented and explained. The lubrication equation and surfactant transport equations are introduced and the evaporation model is presented. Then, in Section 4.3, the numerical results are shown and analyzed. For several dimensionless parameters regime plots are composed and shown in which it is distinguished whether Marangoni circulation occurs or not. The results are compared with literature. In the final section, conclusions are drawn from the obtained results.

4.2. Mathematical model

In this section, the mathematical equations are introduced that describe the droplet evolution and surfactant transport.

4.2.1. Drop evolution

A droplet that is deposited on a substrate is considered. The contact angle θ is assumed ‘small’ ($\theta \leq 40^\circ$ as shown by Hu and Larson [71, 72]) and the density ρ and dynamic viscosity μ are taken constant. Also, the typical drop height $H \leq 10^{-3}$ m, which implies that the Bond number $Bo = \frac{\rho g H^2}{\sigma_{lg}} \ll 1$ (with gravitational acceleration g and surface tension σ_{lg}). Thus, the effects of gravity can be disregarded [61, 167]. Note that this assumption only holds, because there are no possible effects of buoyancy in a single component droplet. For multicomponent droplets, gravity cannot be neglected as shown by Edwards et al. [49] and Li et al. [105]. The Reynolds number is much smaller than unity and a cylindrical coordinate system (r, α, z) is used with the assumptions of no swirl (angular velocity $U_\alpha = 0$) and axisymmetry ($\frac{\partial}{\partial \alpha} = 0$).

Given this case, the Navier-Stokes equations can be rewritten into a 1D evolution equation for the height $h(r, t)$ as a function of radial coordinate r and time t [39]:

$$\frac{\partial h}{\partial t} = \frac{1}{r\mu} \frac{\partial}{\partial r} \left(\frac{rh^3}{3} \frac{\partial p}{\partial r} - \frac{rh^2}{2} \frac{\partial \sigma_{lg}}{\partial r} \right) + w_e. \quad (4.1)$$

Here, p denotes the pressure inside the droplet and w_e the evaporative volume flux, which is negative. From this equation it can be recognized that fluid in a higher pressure region will tend to flow towards a lower pressure region, while fluid in a lower surface tension region will tend to flow towards a higher surface tension region (the Marangoni effect). Furthermore, any evaporation of fluid will accordingly result in a decrease in local drop height. For a derivation of Equation (4.1) and the velocity field (u, w) , see Subsection 2.1.

The pressure in the droplet is dominated by surface tension effects. Therefore, the pressure p can be given by the Laplace pressure:

$$p = -\frac{1}{r} \frac{\partial}{\partial r} \left(\sigma_{lg} \frac{r \partial_r h}{\sqrt{1 + (\partial_r h)^2}} \right). \quad (4.2)$$

Substituting the Laplace pressure in Equation (4.1) shows that the droplet will tend toward a spherical cap shape. If there is no evaporation ($w_e = 0$) a droplet will tend towards an equilibrium, constant curvature shape ($\frac{\partial p}{\partial r} = \frac{\partial \sigma_{lg}}{\partial r} = 0$). Note that σ_{lg} is also part of the derivative in Equation (4.2), because it is not necessarily constant in the presence of surfactants. Thus, rather than writing σ_{lg} outside the derivative as is usually done (e.g. see [165]), it should be included in it as shown by Thiele et al. [178]. Note that Equation (4.2) is beyond the lubrication limit, because of the square root in the denominator. In traditional lubrication theory, this term is approximated as unity.

The boundary and initial conditions that $h(r, t)$ is subjected to are given by:

$$\left(\frac{\partial h}{\partial r}\right)_{r=0} = 0, \quad (4.3)$$

$$\left(\frac{\partial^3 h}{\partial r^3}\right)_{r=0} = 0, \quad (4.4)$$

$$h(R, t) = 0, \quad (4.5)$$

$$h(r, 0) = h_0(r). \quad (4.6)$$

Here, R is the drop radius and h_0 is the initial drop profile, given by the previously mentioned spherical cap shape. The considered cases involve a contact line that is pinned rather than one that moves [23, 158]. This means the drop radius will remain constant during evaporation, while the contact angle decreases, as opposed to a decreasing radius with a constant contact angle. Contact line pinning typically occurs for relatively small contact angles and rough substrates and is also promoted by the presence of surfactants [46, 58, 154, 183].

4.2.2. Interfacial surfactant transport equation

At the liquid-air interface of the droplet a surfactant concentration $\Gamma(r, t)$ can be defined, which can be used to describe the transport of adsorbed surfactant molecules along the interface. As shown by Wong et al. [189], the surfactant transport equation is given by:

$$\begin{aligned} \frac{\partial \Gamma}{\partial t} = & -\frac{1}{r} \frac{\partial(rU_t \Gamma)}{\partial s} + \frac{\Gamma \partial_t h}{1 + (\partial_r h)^2} \left(\frac{\frac{\partial^2 h}{\partial r^2}}{1 + (\partial_r h)^2} + \frac{1}{r} \frac{\partial h}{\partial r} \right) + \\ & \frac{D_\Gamma}{r} \frac{\partial(r \partial_s \Gamma)}{\partial s} + \frac{\partial h}{\partial t} \frac{\partial_r h}{1 + (\partial_r h)^2} \frac{\partial \Gamma}{\partial r} + J_{\Gamma\phi}. \end{aligned} \quad (4.7)$$

Here, U_t is the fluid velocity tangential to the liquid-air interface, D_Γ the surface diffusion coefficient and $J_{\Gamma\phi}$ is the rate with which surfactant is exchanged with the bulk through adsorption and desorption. Note that $J_{\Gamma\phi}$ can be either positive and negative. The derivative $\frac{\partial}{\partial s}$ is the surface derivative which can be written as $\frac{\partial}{\partial s} = \frac{1}{\sqrt{1 + (\partial_r h)^2}} \frac{\partial}{\partial r}$.

The first term on the right-hand side of Equation (4.7) accounts for convective transport tangential to the interface and the second term for transport normal to the interface, which in practice boils down to a source- or sink-like effect as the interfacial curvature decreases or increases respectively. The third term denotes diffusion, the fourth term corrects for the displacement of the surface coordinates that move along the normal of the surface and the last term is the adsorption/desorption of surfactant from the bulk onto the interface and vice versa. For a derivation of Equation (4.7), see Subsection 2.3.

The surfactant concentration $\Gamma(r, t)$ is subjected to the following boundary conditions

and initial condition:

$$\left(\frac{\partial \Gamma}{\partial r}\right)_{r=0} = 0, \quad (4.8)$$

$$\left(\frac{\partial \Gamma}{\partial r}\right)_{r=R} = 0, \quad (4.9)$$

$$\Gamma(r, 0) = \Gamma_0. \quad (4.10)$$

These denote the symmetry condition, no-flux condition and initial (homogeneous) surfactant concentration Γ_0 respectively.

Since surfactants adsorbed at the interface decrease the surface tension, an equation of state for σ_{lg} is required to close the problem. In this work, the Frumkin equation is used, which is analogous to the Langmuir isotherm and considers that surfactant molecules occupy a finite amount of space at the interface [22]. The Frumkin equation is given by:

$$\sigma_{lg} = \sigma_0 + R_u T \Gamma_\infty \ln \left(1 - \frac{\Gamma}{\Gamma_\infty}\right). \quad (4.11)$$

Here, σ_0 is the surface tension of the pure liquid, R_u is the universal gas constant, T the temperature (which is assumed constant) and Γ_∞ the maximum possible surfactant concentration. Note that for $\Gamma \ll \Gamma_\infty$ the equation can be approximated by a linear, dilute equation of state.

Given this equation of state for surface tension and the radial velocity (as defined by Equation (2.7) in the Subsection 2.1) a typical Marangoni velocity can be defined as $u_{Mar} = \frac{H R_u T \Gamma_0}{\mu R}$. This typical velocity is used in Subsection 4.2.6 to define several relevant dimensionless numbers.

4.2.3. Bulk surfactant transport equation

Besides surfactant being adsorbed onto the interface, there is also surfactant dissolved in the bulk of the droplet. The bulk monomer concentration ϕ is considered to be a function of r and t and independent of z , which is allowed as rapid vertical diffusion is assumed (as outlined by [78, 85]). In order to let the concentration be independent of $h(r, t)$, the evolution of the bulk monomer concentration is described as a function of $\psi(r, t) = \phi(r, t)h(r, t)$, as introduced by Thiele et al. [179]. The transport equation can then be written as:

$$\frac{\partial \psi}{\partial t} = \frac{1}{r} \frac{\partial}{\partial r} \left(\frac{r h^2 \psi}{3\mu} \frac{\partial p}{\partial r} - \frac{r h \psi}{2\mu} \frac{\partial \sigma_{lg}}{\partial r} + D_\phi r h \frac{\partial \phi}{\partial r} \right) - J_{\Gamma\phi} \sqrt{1 + (\partial_r h)^2} - J_{M\phi} N. \quad (4.12)$$

In this equation, three terms can be distinguished. The first term is a transport term (with D_ϕ the diffusion coefficient of surfactant monomers in the bulk), which takes into account convective and diffusive transport, the second term is the adsorption/desorption of surfactant from the bulk onto the interface and vice versa, including a factor that compensates for the interface geometry, and the third term is the micelle formation rate $J_{M\phi}$ multiplied with the preferred number of surfactant monomers N which form a single micelle.

When the bulk surfactant concentration exceeds a certain threshold, it becomes energetically more favorable for the molecules to cluster together and form micelles. This threshold is called the critical micelle concentration (CMC). In practice, the number of surfactant monomers that form a single micelle tends to strongly prefer a single value N , which is also assumed in this work [75].

Similarly to the monomer bulk concentration ϕ , the micelle bulk concentration M is given in terms of $\zeta(r, t) = M(r, t)h(r, t)$:

$$\frac{\partial \zeta}{\partial t} = \frac{1}{r} \frac{\partial}{\partial r} \left(\frac{rh^2 \zeta}{3\mu} \frac{\partial p}{\partial r} - \frac{rh \zeta}{2\mu} \frac{\partial \sigma_{lg}}{\partial r} + D_M r h \frac{\partial M}{\partial r} \right) + J_{M\phi}. \quad (4.13)$$

Here, D_M is the diffusion coefficient of micelles. Note that it is assumed here that micelles do not adsorb directly onto the interface. This is a common assumption in literature [11, 48, 85], that follows from the fact that surfactant monomers need to dissociate from micelles before they can be adsorbed onto the interface [133]. Since the micelle formation/decomposition process is modelled as a single step, it is consistent to only allow individual monomers to adsorb onto the interface. Future models, however, could include multi-step models.

The bulk concentrations $\psi(r, t)$ and $\zeta(r, t)$ are subject to the following boundary conditions and initial conditions:

$$\left(\frac{\partial \psi}{\partial r} \right)_{r=0} = \left(\frac{\partial \zeta}{\partial r} \right)_{r=0} = 0, \quad (4.14)$$

$$\left(\frac{\partial \psi}{\partial r} \right)_{r=R} = \left(\frac{\partial \zeta}{\partial r} \right)_{r=R} = 0, \quad (4.15)$$

$$\psi(r, 0) = \phi_0 h(r, t), \quad (4.16)$$

$$\zeta(r, 0) = M_0 h(r, t). \quad (4.17)$$

Similarly to the boundary and initial conditions of Γ , these denote the symmetry condition, the no-flux condition at the contact line and the initial, constant bulk concentrations ϕ_0 and M_0 respectively. All initial surfactant concentrations (Γ_0 , ϕ_0 and M_0) are always chosen to be in equilibrium, so initially $J_{\Gamma\phi} = J_{M\phi} = 0$. A derivation of both Equations (4.12) and (4.13) is given in Subsection 2.4.

4.2.4. Surfactant adsorption

The transport between the interface and the bulk is a continuous adsorption and desorption of molecules that overall tends towards a dynamic equilibrium. Furthermore, there is a limited amount of space available at the interface for surfactants, so as the interfacial concentration increases the adsorption rate tends to decrease, while the desorption rate increases. This behavior can be described by the following reaction equation [48, 85]:



Here, $S (= 1 - \frac{\Gamma}{\Gamma_\infty})$ indicates the fraction of available space at the interface, k_a^Γ is the interfacial adsorption coefficient, and k_d^Γ the interfacial desorption coefficient. Thus,

the interfacial adsorption flux is given by:

$$J_{\Gamma\phi} = k_a^\Gamma \phi \left(1 - \frac{\Gamma}{\Gamma_\infty} \right) - k_d^\Gamma \Gamma. \quad (4.19)$$

In this equation it can indeed be recognized that the first, adsorption term increases as the bulk concentration increases and approaches zero as $\Gamma \rightarrow \Gamma_\infty$, while the second, desorption term becomes more negative as Γ increases. This behavior corresponds indeed to Equation (4.18).

Note that surfactant adsorption onto the substrate is not taken under consideration here, because this will not have a direct effect on the internal flow. Marangoni flow can only occur as a result of a surface tension gradient at a free interface. Any indirect influences of substrate sorption on the flow – surfactant being removed or added to the bulk – are considered less significant.

Similar to Equation (4.18), a reaction equation can be written for the formation of micelles:

$$N\phi \xrightleftharpoons[k_d^M]{k_a^M} M. \quad (4.20)$$

Here, k_a^M is the micelle formation coefficient and k_d^M the micelle decomposition coefficient. This reaction equation can subsequently be written into a micelle formation rate $J_{M\phi}$ as well [11, 48, 85]:

$$J_{M\phi} = k_a^M \phi^N - k_d^M M. \quad (4.21)$$

Given this equation, it is possible to approximate the reaction constants in terms of the CMC and concentrations. It can be seen that the equilibrium concentration is given by $\frac{k_a^M}{k_d^M} = \frac{M}{\phi^N}$. Now, if $\Phi (= NM + \phi)$ is the total concentration of surfactant monomers in the bulk, substitution of the initial total concentration Φ_0 results in:

$$\frac{k_a^M}{k_d^M} = \frac{\Phi_0 - CMC}{N(CMC)^N}. \quad (4.22)$$

Here, it should be noted that in equilibrium $\phi = CMC$, given that there are micelles present. Of course, it is still required to choose one of the reaction constants to define the time scales of the reactions.

4.2.5. Evaporation

The evaporative volume flux w_e is given by:

$$w_e = \frac{D_v M_l p_{sat,l}}{\rho R_u T} \frac{\partial \hat{p}_l}{\partial n} \sqrt{1 + \left(\frac{\partial h}{\partial r} \right)^2}. \quad (4.23)$$

Here, D_v is the vapor diffusivity in air, M_l the molar mass of the liquid, $p_{sat,l}$ the liquid saturation pressure, which is assumed constant, and $\hat{p}_l = \frac{p_l}{p_{sat,l}}$, with p_l the local vapor pressure. The derivative $\frac{\partial}{\partial n}$ is the spatial derivative along the normal vector (pointing outwards) [39].

In order to calculate $\frac{\partial \hat{p}_l}{\partial n}$, it is required to describe the vapor field. As shown by Deegan [37] and Hu and Larson [70], vapor diffusion can be considered instantaneous. Together with the assumption of no convection, this implies that the vapor field can be described by the Laplace equation:

$$\nabla^2 \hat{p}_l = 0. \quad (4.24)$$

The corresponding boundary conditions are given by:

$$\hat{p}_l|_{z=h} = 1 \quad \text{for } r < R; \quad (4.25)$$

$$\frac{\partial \hat{p}_l}{\partial z}|_{z=0} = 0 \quad \text{for } r > R; \quad (4.26)$$

$$\hat{p}_l = RH \quad \text{for } (r, z) \rightarrow \infty. \quad (4.27)$$

Here RH is the relative humidity. These equations represent saturated vapor at the droplet surface, no vapor penetration at the substrate and ambient relative humidity far away from the droplet. An analytical solution to Equation (4.24) is derived in Subsection 2.6.

4.2.6. Dimensionless parameters

In order to analyze when Marangoni circulation occurs, it is helpful to define dimensionless parameters that describe the droplet characteristics. To this purpose, Table 4.1 can be compiled, which gives the ratio between several important scales. Typical numerical values of variables used for the dimensionless numbers are given in Section A.1 of the appendix.

One may note that the traditional capillarity number $Ca = \mu w_e / \sigma_0$ is not listed in Table 4.1. This dimensionless number is omitted, because for any physically relevant case $Ca \ll 1$. Varying Ca therefore has negligible effect on the drop evolution and internal flow field, because surface tension forces always dominate over viscous drag forces, resulting in little deviations from the spherical cap shape. Simulations show that changing Ca by a factor 10^3 only results in a 0.0067% change in total pressure gradient from the drop center toward the contact line.

Name	Symbol	Definition	Expression
Evaporation number	Ev	$\frac{\text{Evaporation velocity}}{\text{Marangoni velocity}}$	$\frac{2 \mu D_v p_{sat, l} M_l (1 - RH)}{\pi H (R_u T)^2 \Gamma_0 \rho}$
Transport number	Tr	$\frac{\text{Desorption rate}}{\text{Marangoni velocity}}$	$\frac{k_d^\Gamma R^2 \mu}{R_u T \Gamma_0 H}$
Desorption number	De	$\frac{\text{Desorption rate}}{\text{Adsorption rate}}$	$\frac{k_d^\Gamma R}{k_a^\Gamma}$
Surface Péclet number	Pe _s	$\frac{\text{Marangoni velocity}}{\text{Surface diffusion rate}}$	$\frac{\Gamma_0 R_u T H}{D_r \mu}$
Bulk Péclet number	Pe _b	$\frac{\text{Marangoni velocity}}{\text{Bulk diffusion rate}}$	$\frac{\Gamma_0 R_u T H}{D_o \mu}$
Micelle transport number	Tr _M	$\frac{\text{Micelle decomposition rate}}{\text{Marangoni velocity}}$	$\frac{k_d^M R^2 \mu}{R_u T \Gamma_0 H}$
Micelle decomposition number	De _M	$\frac{\text{Micelle decomposition rate}}{\text{Micelle formation rate}}$	$\frac{k_d^M (CMC)^{1-N}}{k_a^M}$
Micelle Péclet number	Pe _M	$\frac{\text{Marangoni velocity}}{\text{Micelle diffusion rate}}$	$\frac{\Gamma_0 R_u T H}{D_M \mu}$

Table 4.1.: Relevant dimensionless parameters

4.3. Results and discussion

In this section, the effect of changes in several dimensionless parameters on the occurrence of Marangoni circulation during droplet evaporation with soluble surfactants is analyzed. First, cases without micelles and diffusion are analyzed and subsequently surface and bulk diffusion are taken into account. After that, cases with micelles are considered.

4.3.1. Below CMC without diffusion

Simulations are carried out for various ranges of the dimensionless parameters. The numerical procedure is outlined in Subsection 2.9. The initial contact angle θ_0 is always set to 25° and the contact line is pinned. During each simulation, at least 200 time steps are calculated ($\sim 5\%$ of the drying time), after which the velocity field is analyzed.

Only the initial stage of the evaporation process is considered, because this allows one to capture a ‘snapshot’ of the flow dynamics. It is still required to allow the internal flow dynamics to evolve sufficiently, ensuring that the initial state has no significant effect on the flow field. If the full evaporation process would be taken into account, this would give a skewed perspective on the flow dynamics, because the considered dimensionless numbers change over time. For example, the height decreases over time and the interfacial surfactant concentration increases over time. Also, the bulk concentration may exceed the CMC at some point in time. Analysis of the entire evaporation process is outside the scope of this paper and can be considered in future work. Nevertheless, the results of this work can still be used to predict flow patterns during the entire evaporation process, as long as the relevant dimensionless numbers can be estimated.

Visual analysis of the velocity field has led to the definition of three separate regimes: the ‘coffee-ring regime’, where the flow field looks similar to pure droplet evaporation, the ‘Marangoni regime’, where a clear Marangoni eddy can be distinguished, and the ‘transition regime’, which shows behavior of both the coffee-ring and Marangoni regime. Representative velocity plots of the three regimes are shown in Figure 4.1. In all three velocity regimes an outward, capillary flow can be distinguished, that is caused by selective evaporation at the contact line. However, for the Marangoni regime (and in some degree for the transition regime) there is a backflow close to the interface that convects adsorbed surfactant towards the center, where it desorbs into the bulk again. All three regimes have a zero-fluid velocity at both the liquid-air and liquid-solid interface at $r=0$, which is in accordance with the ‘Hairy ball theorem’ (Poincaré-Brouwer theorem). This theorem predicts that there necessarily exists at least one zero-velocity point on the surfaces of compressible liquids and interfaces allowing mass, energy and momentum transport [14].

Calculating the mean, dimensionless vorticity ω over the middle area where the Marangoni vortex tends to appear (around $R/2 < r < 5/6R$) shows that $\omega \leq -1.2 \cdot 10^{-4}$ corresponds to the Marangoni regime, $-1.2 \cdot 10^{-4} < \omega \leq -0.8 \cdot 10^{-4}$ to the transition regime and $\omega > -0.8 \cdot 10^{-4}$ to the coffee-ring regime. Here, the time scale $t_d = R^2/D_v$ is used

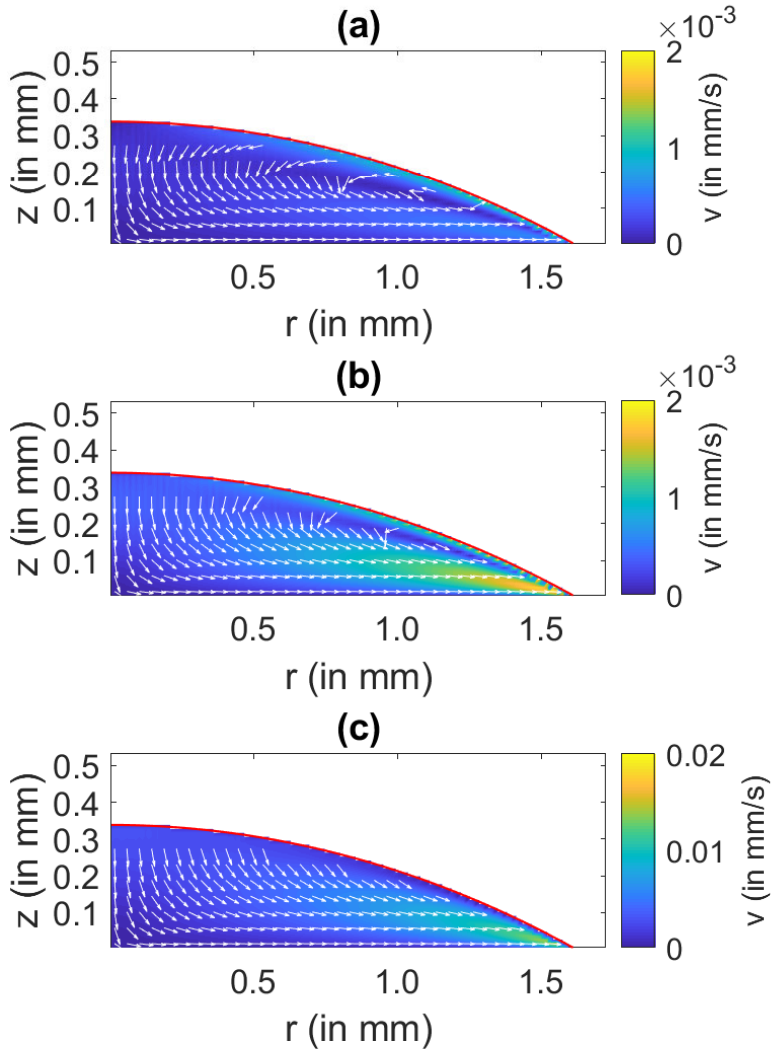


Figure 4.1.: Flow regime classifications: (a) Marangoni regime, (b) Transition regime and (c) Coffee-ring regime. The red line indicates the position of the interface, given by $h(r)$.

to make the vorticity dimensionless.

Alternatively, as a cross-validation the resulting velocity fields can be classified by calculating the fraction of velocity vectors opposing the typical coffee-ring flow. Here, numerical analysis shows that the Marangoni regime corresponds to more than 24% of the radial velocity vectors and more than 9% of the axial velocity vectors pointing

to the center and upward respectively. Similar, the transition regime corresponds to velocity fields that are not in the Marangoni regime with more than 22% of the radial velocity vectors and more than 6% of the axial velocity vectors pointing to the center and upward respectively. If a lower proportion of the velocity vectors points centerwise or upwards, the velocity field is considered to be in the coffee-ring regime. This gives similar results to the classification with vorticity and small variations of the values do not yield significantly different classification results. Further classification of regimes in this paper is made through the mean vorticity with frequent, random visual checks for extra verification.

Figure 4.2 shows the regime charts for simulations without diffusion and without micelles. As can be seen in Figure 4.2a, for $Tr < 1$, both $1/Ev$ and Tr have very similar effects on the occurrence of Marangoni flow. This makes sense, because as $1/Ev$ decreases, the evaporative velocity starts to dominate over the Marangoni velocity. The evaporative effects are thus too strong for the Marangoni effect to counter, resulting in a coffee-ring regime flow. Similarly, as Tr decreases, the effects of adsorption and desorption become less significant (given that De remains constant). This will result in behavior as if the surfactant is insoluble, which is described by the coffee-ring regime [58]. Because the relative strength of the Marangoni effect increases, the interfacial concentration is kept homogeneous since the fluid velocity close to the interface is reduced and the concentration increase at the drop apex due to curvature effects becomes more dominant. At the same time less adsorption is taking place, so the increased bulk concentration close to the contact line will not result in enough interfacial adsorption to cause a positive concentration gradient. That increasing Tr tends to promote Marangoni circulation is also found by Jung et al., who used a lattice-gas model [82].

For $Tr > 1$, the occurrence of Marangoni circulation becomes mostly limited by $1/Ev$. Only if a certain threshold value of $1/Ev$ is exceeded, Marangoni vortices can be formed. At the same time, Tr is largely irrelevant, because the desorption kinetics are no longer dominated by the Marangoni velocity and thus are not a limiting factor anymore. That $1/Ev$ still is a limiting factor however, is not surprising. Decreasing surfactant concentration Γ_0 or increasing the evaporation rate (e.g. through an increase in D_v) will eventually always result in a coffee-ring flow, because either the droplet can be considered pure or the evaporation becomes too dominant.

It is important to note that a correct interpretation of Tr involves not only the desorption rate, but also the adsorption rate. If Tr is varied by changing k_d the value of k_a changes accordingly, given that De should remain constant. Increasing Tr thus does not only mean that interfacial desorption of surfactants becomes more dominant with respect to the Marangoni velocity, but interfacial sorption in general becomes more dominant.

Another relevant observation is that the dimensionless numbers do not necessarily give information about the strength of the Marangoni vortex. As an illustration, Tr can be modified by changing Γ_0 and by changing k_d . An increase in Γ_0 results in a proportional increase in the absolute velocity however, while a decrease in k_d will generally not have that influence. This becomes especially relevant when other physical effects are involved, such as thermal Marangoni flow or the deposition of a solute. For example, Jung et al. conclude that increasing the initial surfactant concentration tends

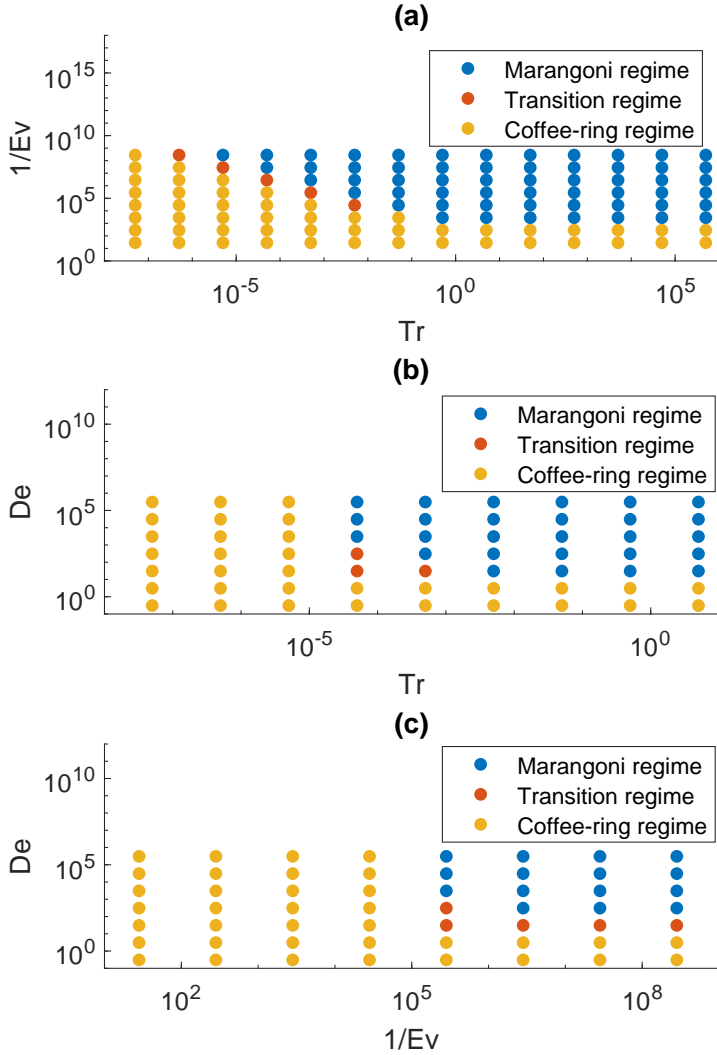


Figure 4.2.: Marangoni circulation regimes without diffusion or micelles: (a) Evaporation number vs. Transport number ($De = 3.08 \times 10^3$), (b) Desorption number vs. Transport number ($1/Ev = 2.82 \times 10^6$) and (c) Desorption number vs. Evaporation number ($Tr = 5.0 \times 10^{-4}$).

to increase the Marangoni strength, thus suppressing the formation of coffee-ring deposits [82]. With respect to Figure 4.2a this can only be explained by also considering the absolute velocity rather than only relative to other time scales.

In Figure 4.2b the influence of the Desorption number De is shown. An increase of

Tr still tends to promote Marangoni circulation, but this only holds approximately for $De > 10$. As the value of De decreases, the contribution of adsorption becomes increasingly similar in magnitude to desorption. As a result, Marangoni circulation is increasingly suppressed. The reason for this suppression is that De effectively is the solubility of the surfactant. As De decreases, the surfactant solubility also decreases and the surfactant increasingly starts to behave as insoluble. This effectively means that the bulk concentration becomes relatively small with respect to the interfacial concentration. As a consequence, adsorption onto the interface, resulting from concentration increases in the bulk, will become less significant. Therefore, positive interfacial concentration gradients towards the contact line will no longer arise. On the contrary, the interfacial concentration gradient will tend to be negative towards the contact line as a result of the interface shrinking fastest at the drop apex. The result is a flow in the coffee-ring regime. The flow close to the interface is here reduced by the Marangoni effect to counter any positive surfactant gradients. This flow behavior was previously found by van Gaalen et al. [58] for insoluble surfactants.

The behavior of Figure 4.2a and 4.2b is reflected in Figure 4.2c: if evaporation becomes more dominant the flow tends to transition to the coffee-ring regime. Similar, as the desorption number is decreased Marangoni circulation will not appear anymore some point.

The results in Figure 4.2 are consistent with experiments performed by Marin et al. [115]. They performed experiments both below and above CMC with the surfactants polysorbate 80 (P80) and sodium dodecyl sulfate (SDS). P80, is a large, slow surfactant, with low solubility ($CMC=0.012$ mM [26]), while SDS is a small, fast surfactant, with higher solubility ($CMC=8.2$ mM [127]).

For P80 Marin et al. reported a suppression of thermal Marangoni flow and a severe reduction of the interfacial flow strength. This is also predicted by the numerical model, given the physical properties of P80. Slow adsorption kinetics correspond to a low Tr and low solubility to a low De . In all three subfigures of Figure 4.2 it can be seen that these low values would predict a coffee-ring flow and not a solutal Marangoni flow. Furthermore, a low De also results in a reduced interfacial velocity and thus suppression of any thermal Marangoni flow, which is consistent with the experimental results.

For SDS, on the other hand, Marin et al. reported completely opposite behavior. SDS tends to increase the strength of Marangoni circulation. The fast adsorption kinetics of SDS correspond to a high Tr and the high solubility to a high De . This would place SDS in the Marangoni regime, as can be seen in Figure 4.2. Consequently, it is not surprising to see an increase in Marangoni circulation, since SDS increases the magnitude of the already negative thermal surface tension gradient.

From these two examples it becomes clear how two different surfactants can have opposite effects on the flow in drops and thus it underlines the explanatory power of the numerical model.

4.3.2. Below CMC with diffusion

Given the results in Subsection 4.3.1, additional degrees of freedom can be introduced by setting the bulk and surface diffusion coefficients to a nonzero value. In this way, two different regime plots can be drawn: one with surface diffusion, but without bulk diffusion, and one with bulk diffusion, but without surface diffusion. The result are displayed in Figure 4.3.

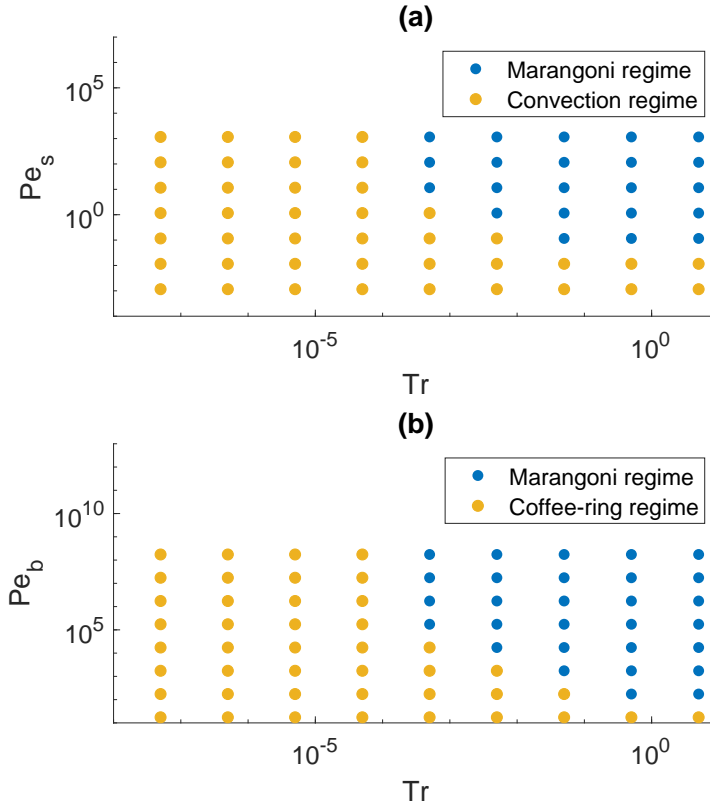


Figure 4.3.: Marangoni circulation regimes with diffusion, without micelles ($1/Ev = 2.82 \times 10^6$, $De = 3.08 \times 10^3$): (a) Surface Péclet number vs. Transport number ($Pe_b = \infty$) and (b) Bulk Péclet number vs. Transport number ($Pe_s = \infty$).

As can be seen in Figure 4.3a, decreasing the surface Péclet number tends to suppress Marangoni circulation. This makes sense, because as the effect of surface diffusion increases, a smaller Marangoni flow is required to counter any interfacial concentration gradient. Adsorption from the bulk causes a surface tension gradient, but this gradient is increasingly counteracted by surfactant diffusion at the interface. The result tends increasingly towards a coffee-ring-regime flow as Pe_s decreases to and becomes smaller than unity.

Similar behavior can be distinguished when the bulk Péclet number is varied. As Pe_b is decreased, Marangoni circulation tends to be suppressed, because the bulk concentration increases less sharply. This way, adsorption of surfactant from the bulk onto the interface occurs over a larger area at the contact line, resulting in a flattening of the surface tension gradient. Since at the same time the surfactant concentration increases towards the drop apex due to the shrinking of available interface, a nearly constant interfacial surfactant concentration arises. Thus, the flow will tend towards the coffee-ring regime as the influence of bulk diffusion increases. Interestingly enough, the transition from the Marangoni regime to the coffee-ring regime already starts to occur for $Pe_b < 10^5$, which is a factor 10^4 higher than the surface Péclet number at which this transition happens. This implies that bulk diffusion has a larger influence than surface diffusion.

4.3.3. Above CMC without monomer diffusion

As the bulk concentration increases, at some point it becomes energetically more favorable for surfactant molecules to cluster together in the form of micelles rather than as separate monomers. This will influence the internal droplet dynamics, since as the local monomer concentration increases in the bulk, only part of the surfactant monomers will adsorb onto the interface and another part will form micelles. In Figure 4.4 the effect of micelles on the internal flow patterns is shown. In the simulations the initial bulk concentration starts at CMC.

Figure 4.4a shows that as the micelle transport number Tr_M increases, and thus the rates with which micelles are formed and decompose increase, Marangoni circulation seems to become increasingly suppressed. This suppression can be explained by the fact that the formation of micelles reduces the absorption of bulk monomers onto the interface, because the bulk concentration is now also reduced through an additional mechanism. Both adsorption onto the interface and formation of micelles can now reduce a high bulk concentration. Since less surfactant is absorbed onto the interface than without micelle formation, the surface tension gradient becomes less pronounced, which increasingly results in suppression of Marangoni circulation.

Regarding the micelle decomposition number, it is shown in Figure 4.4b that for $De_M < 1$ the value of De_M is largely irrelevant. The transition from coffee-ring regime to Marangoni regime is at that point only dependent on Tr . For $De_M > 1$ however, a shift of the critical Tr to the left is observed. This shift can be explained by reformulating the definition of De_M . Substitution of Equation (4.22) in the definition of De_M yields:

$$De_M = \frac{k_d^M (CMC)^{1-N}}{k_a^M} = \frac{N \cdot CMC}{c_0 + M_0 N - CMC} = \frac{CMC}{M_0}. \quad (4.28)$$

Here, it is used that $c_0 = CMC$. Given this reformulation it becomes clear that varying the initial micelle concentration M_0 has a proportional effect on De_M and vice versa. A high value of De_M (e.g. larger than unity) would thus correspond to a relatively low value of M_0 , which implies that the shift in Figure 4.4b is a transitional effect: the flow dynamics have not fully transitioned from below CMC to above CMC for $De_M > 1$.

In Figure 4.4c it can be seen that the micelle Péclet number Pe_M has a similar effect on

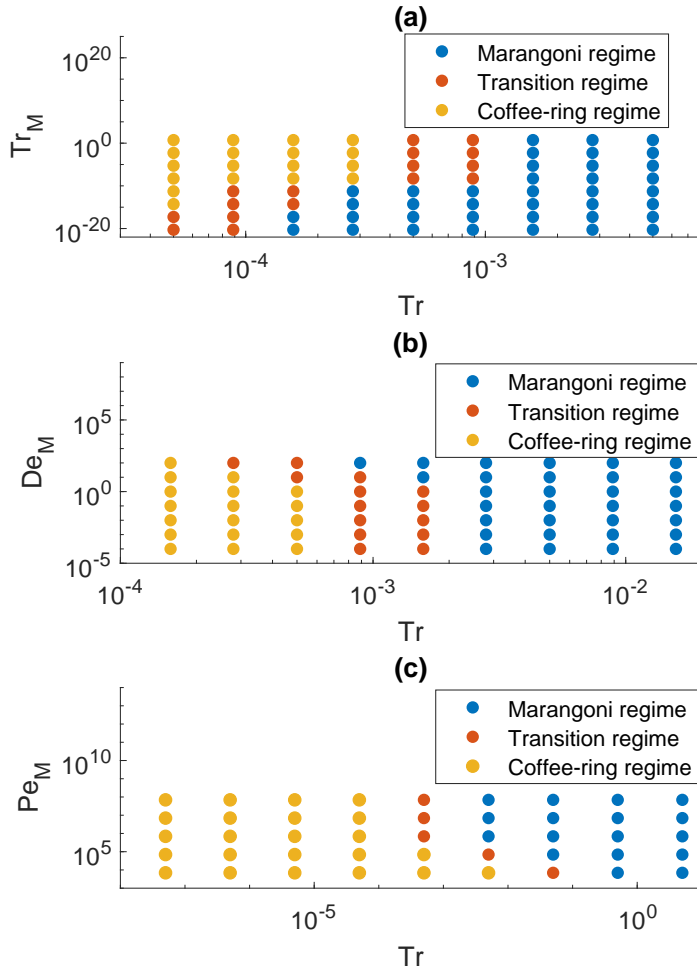


Figure 4.4.: Marangoni circulation regimes without monomer diffusion, with micelles ($1/Ev = 2.82 \times 10^6$, $De = 3.08 \times 10^3$, $Pe_s = Pe_b = \infty$): (a) Micelle transport number vs. Transport number ($Pe_M = 6.96 \times 10^7$, $De_M = 10$), (b) Micelle decomposition number vs. Transport number ($Pe_M = 6.96 \times 10^7$, $Tr_M = 5.25 \times 10^{-3}$) and (c) Micelle Péclet number vs. Transport number ($De_M = 10$, $Tr_M = 5.25 \times 10^{-3}$).

the flow dynamics as Pe_s and Pe_b . As Pe_M is reduced, the transition from coffee-ring regime to Marangoni regime shifts to a higher Tr . This is caused by micelles being transported inward as a result of diffusion. There, they decompose into surfactant monomers, effectively reducing the bulk concentration gradient. Subsequently, the interfacial concentration gradient is also reduced, counteracting Marangoni circulation.

To summarize, the simulations predict that for concentrations above CMC Marangoni circulation becomes more suppressed than below CMC, although this effect is minor. In experiments however, the influence of surfactants tends to increase even more beyond the CMC. For example, Marin et al. [115] reported that for experiments with P80 above CMC the surface velocity is even more reduced than below CMC and for very high concentrations even reversed. Furthermore, they show that for SDS the Marangoni circulation becomes even stronger above CMC than below CMC and even report several Marangoni vortices at once. Similarly, Sempels et al. [157] reported for Triton X-100 an increased strength of the Marangoni flow as the surfactant concentration is increased, while it is already above the CMC.

These differences between simulations and experiments can possibly be explained by physical effects that have not been taken into account in the numerical model. For example, micelles may adsorb directly onto the interface, without the need to first decompose into bulk monomers. Models used in literature (including this work) usually assume a single step monomer adsorption model [11, 48, 85], but in reality the adsorption process is more complex, especially when micelles are involved [133]. This is even more the case for high deviations from equilibrium. Direct adsorption of micelles would indeed explain why the experiments show an increased Marangoni flow above CMC: for fast surfactants (e.g. SDS) there is more adsorption/desorption resulting in higher surface tension gradients.

However, this would not explain the even further reduced and reversed surface velocity for P80 and the dual vortices for SDS. This may possibly be attributed to other adsorption and transport effects, such as adsorption onto the substrate (or even micelle formation on the substrate [97]) and transport of surfactant from the substrate to the interface through the contact line [85]. This may have significant influence on the flow.

An alternative factor that could play a role in the experiments, is the influence of micelles on the fluid properties of the droplet. As an illustration, it is well known that particles (like micelles) tend to increase the viscosity of a fluid [8, 92]. Especially if larger, more complex aggregates are formed [77], this may play a significant role. Also, the shape of the particles can play a major role. For example, while spherical particles do not tend to influence the flow significantly, ellipsoidal particles tend to aggregate at the interface in loosely packed structures [15, 19, 108, 111]. This can either increase [194] or decrease [109] the surface tension and keep the particles from flowing towards the contact line. A possible way of modeling this, would be to allow adsorption-like behavior for the micelles, combined with an equation of state for surface tension. The self-assembly could then be modeled through a concentration-dependent resistance to flow and increased ‘adsorption’ with surface concentration.

Nevertheless, it can be concluded that while the model is consistent with experiments below CMC, it deviates above CMC. This shows the need for models that capture surfactant kinetics above CMC in a more detailed way than the standard models that are used in this work and in literature [11, 48, 85].

4.4. Conclusion

A numerical model was developed to predict the flow in evaporating droplets with soluble surfactants. The drop evolution and flow behavior have been modeled with lubrication theory and the surfactants were implemented by means of coupled convection-diffusion-adsorption equations. Simulations were carried out for variations in several dimensionless parameters, over a broad range. The discovered changes in flow characteristics were compared with both experimental and numerical results from literature.

Below CMC, three parameters (Tr , Ev , De) were analyzed for cases without diffusion and two additional parameters (Pe_s , Pe_b) were considered for cases with diffusion. The effects of these parameters on the internal flow patterns were explained and found to be consistent with experimental and numerical results from literature [82, 115].

Above CMC, three additional parameters (Tr_M , De_M , Pe_M) were analyzed. Although these results could be explained intuitively, they were found to differ from experimental results from literature. In experiments, the effect of surfactants on the flow properties tends to become increasingly more dominant as the surfactant concentration increases and even results in different qualitative behavior [115, 157], while in the simulations the influence of micelles tends to be rather small. These differences can possibly be explained by more complex adsorption and transport mechanisms, such as micelle formation on the substrate [97], and fluid properties changing due to micelles, both effects that have not been taken into account in the model. This shows that more detailed models are needed to capture all relevant dynamics of micelles. These effects are not considered in current state-of-the-art models [11, 48, 85].

Nevertheless, the results agree with the hypothesis that was made, namely that using dimensionless numbers regime plots can be drawn to predict whether Marangoni vortices will arise. This was done both below and above CMC and the qualitative agreement with experiments is quite good below CMC.

The relevance of these findings lies first of all in the ability to explain experimental results. The numerical model shows why surfactants can have opposite influences on flow dynamics in evaporating droplets. Furthermore, this paper shows the predictive power of the model. The results can be used to predict and understand the flow dynamics in a surfactant-laden droplet. For example, surfactants that are larger and slower than P80 can be assumed to reduce the interfacial flow, while surfactants that are smaller and faster than SDS will only accelerate the Marangoni circulation. Also, it is shown that increasing the surfactant concentration will generally not increase the likelihood of encountering flow circulation (except for very low concentrations as can be seen in Figure 4.2a). This counter-intuitive phenomenon is also implied by the results of Marin et al., where they show that an increase in P80 only slows the interfacial velocity further.

The explanatory and predictive power of the model is relevant in a broad range of applications. Evaporating sessile droplets are applied in various technologies, such as inkjet printing [122, 138], pesticides [64, 69], surface patterning [67] and spray cooling [89]. Close to all of these technologies involve surfactants, either on purpose or through contamination. It is thus of crucial importance to have a deep understanding

of the effect of this component, in order to control the internal flow and deposition pattern.

Most preceding numerical studies focused either on the evaporation of droplets without surfactants [39, 40, 41, 87, 165] or on the evolution of nonvolatile droplets with surfactants [10, 11, 21, 28, 48, 64, 79, 85, 188, 191]. Only a few previous numerical studies involved both evaporation and surfactants [58, 82, 86]. However, this study is the first to numerically analyze the evolution of evaporating droplets with soluble surfactants and the corresponding internal flow patterns. Furthermore, various experimental studies consider the evaporation of droplets with surfactants [45, 46, 154, 156, 172, 183, 190], but actual flow visualisations are rare [115, 157]. Numerical work, like this study, can therefore be an attractive alternative.

Future research opportunities lie in expansion of the micelle model. The current model [11, 48, 85] is not able to fully explain the experimental results [115, 157] and thus additional physical effects need to be added. For example, direct adsorption of micelles onto the interface and monomer adsorption onto the substrate may be able to explain experimental results above CMC. Furthermore, it may also be useful to investigate the full evaporation process of the droplet, including moving contact lines, to be able to analyze drying patterns. This will enable the control of the final deposition in technologies as inkjet printing.

5. Absorption of droplets with soluble surfactants

In this chapter¹ the effect of surfactants on the absorption behavior of droplets is analyzed. If surfactants tend to adsorb onto solid-liquid interfaces they can potentially accelerate the capillary imbibition of droplets into porous media. However, it is not always clear when surfactants have this effect and how the effect scales with respect to parameters as the surfactant concentration. The numerical results are compared to experimental literature both quantitatively and qualitatively.

5.1. Introduction

Porous media are encountered everywhere. The soil in which seeds are planted, the paper that is used for books and even the human skin are all permeable solids. Despite this widespread occurrence, the flow through porous media is not trivial to understand. Because of the thousands of tiny, twisting, interconnected channels it is complex to track a fluid flow in a porous medium, both numerically and experimentally. Nevertheless, research into this topic is valuable: understanding the flow through porous media allows one to develop or improve a broad range of technologies, such as inkjet printing [24, 101, 164], irrigation [181], oil recovery [123, 174] and even medical treatments [25, 88, 185].

In several of these applications, liquid droplets absorb into the porous medium (e.g. [25]). Although the effect of several factors on this wetting process has been extensively studied (porosity, permeability, contact angle, gravity, suction pressure etc.) [2, 3, 33, 34, 57, 144, 145, 164, 193], others received less attention.

One of these uninvestigated factors is the dynamics of the contact line of an absorbing sessile droplet on top of the porous medium. In case of partial wetting, dynamic contact line behavior can be roughly categorized into two modes: pinning behavior, where the contact angle changes over time, while the contact radius remains constant, and slipping behavior, where the contact radius changes over time, while the contact angle remains constant [36]. Typical factors that promote slipping behavior over pinning behavior are smoother substrates [13], higher contact angles and increasing deviations from the equilibrium contact angle [135]. Apart from the two extreme possibilities, also a combination is often encountered, called stick-slip behavior, in which the contact line is intermittently pinned and slipping [186].

If the contact line is allowed to slip, the total contact area of the droplet will decrease over time during the absorption process. It is therefore hypothesized that droplets with moving contact lines absorb more slowly than droplets with pinned contact lines. Furthermore, it can be expected that for unpinned contact lines the wetted volume

¹This chapter is based on the article: 'Absorption of surfactant-laden droplets into porous media: a numerical study' by van Gaalen et al. [60]

will have a different shape than for pinned contact lines. This is valuable information given that parameters as absorption rate and penetration depth are important in several technologies. For example, in case of inkjet printing slow absorption can cause smudging and shallow penetration may reduce the lifetime of the product.

Another factor in droplet absorption that has not been fully investigated, is the composition of the fluid. Especially the effects of surfactants on droplet absorption have received only limited attention in the experimental literature [80, 81] and next to none in numerical articles. This is despite the fact that surfactants are known to be able to ‘enhance’ (i.e. accelerate) the absorption process, in case a liquid reservoir is absorbed into a porous medium (1D absorption), which was demonstrated both experimentally [123, 129, 134, 147, 174] and theoretically [169]. It is therefore expected that surfactants can cause a similar enhancement to droplet absorption, which is of relevance given the wide usage of surfactants in droplet technology.

In this work the effects of contact line dynamics and surfactants on the absorption of droplets into porous media are considered. Results are obtained with an axisymmetric 3D numerical model that is based on a combination of lubrication theory and Darcy’s law. By assuming a relatively small contact angle, an efficient yet accurate model can be developed to simulate droplet dynamics [71, 72]. The surfactant transport is modelled by several convection-diffusion-adsorption equations [59, 179].

The article has the following structure: first, in Section 5.2, the equations are introduced that describe the problem and the numerical procedure is outlined. The droplet model and the absorption model are presented and an explanation is given for the surfactant transport equations and the corresponding closure relations. After that, in Section 5.3, the numerical results are analyzed and validated by comparison with experimental literature. The differences in absorption of a droplet with a pinned and a moving contact line are discussed and the effect of surfactants is considered both qualitatively and quantitatively for various pore sizes. Lastly, in a concluding section, the results are summarized and an evaluation is given of the current state of the art and potential future research.

5.2. Mathematical model

In this section, the equations that describe the system are given and explained.

5.2.1. Drop evolution

A sessile droplet on a porous substrate is considered. The droplet initially has a height H at its center, a contact line radius R and a contact angle θ . The fluid the droplet consists of is nonvolatile, incompressible and isothermal. Thus, no evaporation occurs and mass density ρ and dynamic viscosity μ remain constant. Only cases are assumed for which H is smaller than the capillary length $l_c = \sqrt{\frac{\sigma_{lg}}{(\rho - \rho_g)g}}$, where σ_{lg} denotes the surface tension between the liquid-gas interface, ρ_g the mass density of the gas and g the gravitational acceleration. This means that the effects of gravity can be neglected.

The Reynolds number is much smaller than unity and a cylindrical coordinate system (r, α, z) is used to describe the system. The problem is considered axisymmetric, which implies that $\frac{\partial}{\partial \alpha} = 0$ and it is assumed that there is no swirl ($U_\alpha = 0$). The contact angle θ is relatively small (about $\theta < 40^\circ$), meaning that lubrication theory ($\epsilon = H/R \ll 1$) can be applied, as shown by [71, 72].

Given lubrication theory, an evolution equation for the droplet height profile $h(r, t)$ can be derived [58]:

$$\frac{\partial h}{\partial t} = \frac{1}{r\mu} \frac{\partial}{\partial r} \left[r \left(\frac{h^3}{3} + \beta h^2 \right) \frac{\partial p}{\partial r} - r \left(\frac{h^2}{2} + \beta h \right) \frac{\partial \sigma_{lg}}{\partial r} \right] - W_p. \quad (5.1)$$

Here, β is the Navier slip length, which is an indicator for the degree of slip that is allowed, p denotes the pressure and W_p the volume flux into the substrate, caused by capillary suction. This volume flux is equal to the vertical fluid velocity w_p at $z = 0$, which will be derived later on. The boundary and initial conditions that define the droplet evolution are given by:

$$\left(\frac{\partial h}{\partial r} \right)_{r=0} = 0; \quad (5.2)$$

$$\left(\frac{\partial p}{\partial r} \right)_{r=0} = 0; \quad (5.3)$$

$$\left(\frac{\partial \sigma_{lg}}{\partial r} \right)_{r=0} = 0; \quad (5.4)$$

$$h(R, t) = 0; \quad (5.5)$$

$$h(r, 0) = h_0(r). \quad (5.6)$$

These equations denote the symmetry conditions at $r = 0$ (for h, p and σ_{lg}), the contact line position at $r = R$ (where $h = 0$) and the initial drop profile h_0 , which is a spherical cap. Given that the droplet is considered under partial wetting conditions, there is an associated equilibrium shape (a spherical cap) with a corresponding equilibrium contact angle. This as opposed to complete wetting conditions, where there is no equilibrium associated and the droplet spreads out indefinitely. The equilibrium contact angle can be anywhere between the advancing and receding contact angle of the liquid, depending on the degree of hysteresis. Since in the considered cases the spherical cap shape is formed nearly instantaneously compared to the absorption process ($t_{cap} \sim \mu R / \sigma_{lg} \approx 10^{-5} s \ll t_{abs} \approx 1 - 10^{-2} s$) and the contact angle equilibrates nearly instantaneously (numerical experiments typically show $t_\theta = t_{abs}/100$), it can be assumed that the droplet is initially in quasi-equilibrium, i.e. the equilibrium shape as if the substrate is nonpermeable (also see [33, 34]).

The contact line can be either pinned, for which $\beta = 0$ and R remains constant, or moving, for which $\beta > 0$ and a constitutive relation for R is required that describes the contact line velocity [168]. In this work, we use the relation:

$$\frac{dR}{dt} = \begin{cases} k|\theta - \theta_{adv}|^a & \text{if } \theta_{adv} \leq \theta \\ 0 & \text{if } \theta_{rec} < \theta < \theta_{adv} \\ -k|\theta - \theta_{rec}|^a & \text{if } \theta \leq \theta_{rec} \end{cases} \quad (5.7)$$

Here, k is a typical sensitivity of the contact line position to deviations of the contact angle θ from the receding contact angle θ_{rec} or the advancing contact angle θ_{adv} and a is a power-law index, which can range from 1 to 3. This relation is extensively used and experimentally validated in literature [12, 21, 28, 51, 58, 66, 166]. In this work, unpinned contact lines are only considered for pure droplets, because surfactants have a strong tendency to pin the contact line [46, 58, 154, 156, 183].

The pressure in the droplet is dominated by curvature effects of the surface. This means that p can be given by the Laplace pressure:

$$p = -\frac{1}{r} \frac{\partial}{\partial r} \left(\sigma_{lg} \frac{r \partial_r h}{\sqrt{1 + (\partial_r h)^2}} \right). \quad (5.8)$$

Here, ∂_r denotes the partial derivative with respect to r . Note that p only depends on r and is independent of z . This is a consequence of the lubrication approximation, meaning that results are more accurate for lower values of ϵ (see e.g. [71, 72]).

5.2.2. Absorption model

The droplet is absorbed into the porous substrate as a result of capillary action. This flow can be modeled on a macroscopic level by applying Darcy's law, which is often used for the flow through porous media [2, 4, 5, 164]. This model is chosen for its simplicity over other models, while still being sufficiently accurate [149] and able to deal with the boundary conditions that are involved (e.g. for an impermeable boundary Brinkman's extension would be required [17, 117]).

Darcy's law gives a relation for the velocity field $\vec{u}_p = (u_p, w_p)$:

$$u_p = -\frac{\kappa}{\mu} \left(\frac{\partial p_p}{\partial r} \right); \quad (5.9)$$

$$w_p = -\frac{\kappa}{\mu} \left(\frac{\partial p_p}{\partial z} \right). \quad (5.10)$$

Here, κ is the permeability of the substrate and p_p the pressure in the wetted region. A good measure for κ_p can be given by the Carman-Kozeny equation [20, 90], which is a model for the flow through a packed bed of solid spheres with diameter d . The permeability is subsequently given by:

$$\kappa = \frac{\eta^3 d^2}{180(1 - \eta)^2}, \quad (5.11)$$

with η the porosity of the porous medium.

Given mass conservation, it follows that the pressure field can be found by solving the Laplace equation:

$$\frac{1}{r} \frac{\partial}{\partial r} (r u_p) + \frac{\partial w_p}{\partial z} = \frac{1}{r} \frac{\partial}{\partial r} \left(r \frac{\partial p_p}{\partial r} \right) + \frac{\partial^2 p_p}{\partial z^2} = 0. \quad (5.12)$$

The boundary conditions which p_p is subjected to are given by:

$$p_p|_{z=0} = p \quad \text{for } r < R; \quad (5.13)$$

$$\frac{\partial p_p}{\partial z}\Big|_{z=0} = 0 \quad \text{for } r > R; \quad (5.14)$$

$$p_p|_{z=-h_p} = p_c. \quad (5.15)$$

Equation (5.13) describes the pressure that the droplet exerts on the substrate, Equation (5.14) is the no penetration condition at the substrate surface next to the droplet and Equation (5.15) is the capillary suction the fluid in the wetted region experiences at its interface, defined at $z = -h_p$. The corresponding capillary pressure p_c can be estimated by considering the capillary action in a single, round channel:

$$p_c = -\frac{4\sigma_{lg} \cos \theta_{adv}}{d}. \quad (5.16)$$

Here, θ_{adv} is the advancing contact angle. Note that the channel diameter used in the expression for p_c is assumed to be equal to the sphere diameter that is used for estimating κ . With an expression for the velocity field, the evolution equation for h_p can be found, similar to Equation (5.1):

$$\frac{\partial h_p}{\partial t} = -\frac{1}{\eta r} \frac{\partial}{\partial r} \int_0^{h_p} r u_p dz + \frac{1}{\eta} W_p. \quad (5.17)$$

In the porous medium there are also symmetry conditions at $r = 0$, specifically $\partial_r h_p = \partial_r p_p = \partial_r u_p = \partial_r w_p = 0$. Furthermore, there initially is a thin fluid film h^* in the porous medium, just below the area covered by the droplet, which is required to remove the incompatibility of Equations (5.13) and (5.15) for $h_p = 0$.

5.2.3. Surfactant in the droplet

At the liquid-air interface of the droplet a surfactant concentration $\Gamma(r, t)$ is defined. The transport equation for $\Gamma(r, t)$ is given by [189]:

$$\begin{aligned} \frac{\partial \Gamma}{\partial t} = & -\frac{1}{r} \frac{\partial(r U_t \Gamma)}{\partial s} + \frac{\Gamma \partial_t h}{1 + (\partial_r h)^2} \left(\frac{\frac{\partial^2 h}{\partial r^2}}{1 + (\partial_r h)^2} + \frac{1}{r} \frac{\partial h}{\partial r} \right) + \\ & \frac{D_\Gamma}{r} \frac{\partial(r \partial_s \Gamma)}{\partial s} + \frac{\partial h}{\partial t} \frac{\partial_r h}{1 + (\partial_r h)^2} \frac{\partial \Gamma}{\partial r} + J_{\Gamma \phi}. \end{aligned} \quad (5.18)$$

Here, U_t is the fluid velocity tangential to the liquid-air interface, D_Γ is the surface diffusion coefficient and $J_{\Gamma \phi}$ is the sorptive transport between the interface and the bulk. The fraction $\frac{\partial}{\partial s} = \frac{1}{\sqrt{1 + (\partial_r h)^2}} \frac{\partial}{\partial r}$ denotes the surface derivative. The right-hand side of Equation (5.18) consists of several terms of which each corresponds to a specific transport contribution. The first term denotes the convective fluid transport tangential to the surface, the second term is the change rate in concentration as a result of changes in curvature, the third term is the diffusion rate and the fourth term corrects for the transformation of the surface coordinates to the cylindrical coordinates [58, 59].

Similarly, a transport equation for the surfactant bulk concentration $\phi(r, t)$ can be given. This concentration is assumed to be independent of z , meaning that any vertical concentration gradient is considered insignificant. This is a generally used assumption in literature when the lubrication approximation is used [59, 78, 85]. The

transport equation is defined in terms of $\psi(r, t) = \phi(r, t)h(r, t)$, because in that case the dependent variable becomes independent of $h(r, t)$ [179]:

$$\frac{\partial \psi}{\partial t} = \frac{1}{r} \frac{\partial}{\partial r} \left(\frac{r h^2 \psi}{3\mu} \frac{\partial p}{\partial r} - \frac{r h \psi}{2\mu} \frac{\partial \sigma_{lg}}{\partial r} + D_\phi r h \frac{\partial \phi}{\partial r} \right) - J_{\Gamma\phi} \sqrt{1 + (\partial_r h)^2} - \phi W_p - \frac{2D_\phi}{h} (\phi - \phi_p|_{z=0}). \quad (5.19)$$

Here, D_ϕ denotes the bulk diffusion coefficient and $\phi_p(r, z, t)$ is the bulk surfactant concentration in the pores. The first term on the right-hand side consists of three parts: a pressure-driven convection part, a part that accounts for the Marangoni effect and a diffusion part. The second term is the sorptive exchange with the liquid-air interface, including a factor that takes into account the slope of the interface ($\frac{\partial s}{\partial r}$). The third term is the convective transport flux with the porous medium and the last term is the diffusive exchange with the porous medium.

The concentrations $\Gamma(r, t)$ and $\phi(r, t)$ are subject to the following boundary conditions and initial conditions:

$$\left(\frac{\partial \Gamma}{\partial r} \right)_{r=0} = \left(\frac{\partial \psi}{\partial r} \right)_{r=0} = 0; \quad (5.20)$$

$$\left(\frac{\partial \Gamma}{\partial r} \right)_{r=R} = \left(\frac{\partial \psi}{\partial r} \right)_{r=R} = 0; \quad (5.21)$$

$$\Gamma(r, 0) = \Gamma_0; \quad (5.22)$$

$$\psi(r, 0) = \phi_0 h(r, 0). \quad (5.23)$$

The boundary conditions denote the symmetry condition and the no-flux condition at the contact line.

The surfactants at the interface $\Gamma(r, t)$ tend to reduce the liquid-gas surface tension σ_{lg} , meaning that an equation of state is required to close the problem. In this work, the Szyszkowski equation of state is chosen for this purpose, which takes into account the repelling effect individual surfactant molecules have on each other [22]. This closure relation is typically valid for intermediate interfacial concentrations that are not too close to the maximum concentration Γ_∞ . For lower concentrations the equation reduces to the linear, dilute equation of state. The Szyszkowski equation is given by:

$$\sigma_{lg} = \sigma_{lg,0} + R_u T \Gamma_\infty \ln \left(1 - \frac{\Gamma}{\Gamma_\infty} \right). \quad (5.24)$$

In this equation, $\sigma_{lg,0}$ denotes the liquid-gas surface tension for a surfactant-free liquid, R_u is the universal gas constant and T the temperature.

The sorptive exchange depends on both the bulk concentration $\phi(r, t)$ and the interfacial concentration $\Gamma(r, t)$ and on the available space at the interface [48, 59, 85]. Thus, the following equation for $J_{\Gamma\phi}$ can be assumed:

$$J_{\Gamma\phi} = k_a^\Gamma \phi \left(1 - \frac{\Gamma}{\Gamma_\infty} \right) - k_d^\Gamma \Gamma. \quad (5.25)$$

Here, k_a^Γ and k_d^Γ are the adsorption and desorption coefficients of the liquid-air interface respectively. In this equation it can be recognized that the positive adsorption

term increases for higher bulk concentrations and lower interfacial concentrations, while the negative desorption term only depends on Γ [48].

5.2.4. Surfactant in the porous medium

In contrast to the surfactant bulk concentration $\phi(r, t)$ in the droplet, the bulk concentration in the porous medium $\phi_p(r, z, t)$ is also assumed to depend on the axial coordinate z . The reason for this is that the vertical dimension of the wetted region typically is of the same order of magnitude as the horizontal dimension. Furthermore, the pressure gradient has a significant component in axial direction. The evolution of $\phi_p(r, z, t)$ is thus to be described by an axisymmetric 3D convection-diffusion-adsorption equation:

$$\frac{\partial \phi_p}{\partial t} = -\frac{1}{r} \frac{\partial}{\partial r} \left(r \phi_p \frac{u_p}{\eta} \right) - \frac{\partial}{\partial z} \left(\phi_p \frac{w_p}{\eta} \right) + \frac{D_\phi}{r} \frac{\partial}{\partial r} \left(r \frac{\partial \phi_p}{\partial r} \right) + D_\phi \frac{\partial^2 \phi_p}{\partial z^2} - J_{\phi S}. \quad (5.26)$$

Here, $J_{\phi S}$ accounts for the sorption between the bulk and the walls of the pores. This effect is not considered in the droplet itself, because there the total liquid-solid interface is much smaller. Furthermore, adsorption onto the solid-liquid interface does not directly influence the flow behavior (it cannot cause Marangoni flow) and will not change the contact angle of the droplet, because only pinned cases are considered when surfactants are involved. The concentration $\phi_p(r, z, t)$ is subject to the following boundary and initial conditions:

$$\phi_p(r, z, 0) = \phi_{p,0}; \quad (5.27)$$

$$\phi_p(r, 0, t) w_p(r, 0, t) = \phi(r, t) W_p(r, t); \quad (5.28)$$

$$\frac{\partial \phi_p}{\partial r} \Big|_{r=0} = 0. \quad (5.29)$$

Furthermore, surfactant cannot be transported outside the wetted region.

The sorption term $J_{\phi S}$ is given by:

$$J_{\phi S} = \frac{4}{d} k_a^S \phi_p \left(1 - \frac{S}{S_\infty} \right) - k_d^S S, \quad (5.30)$$

with k_a^S and k_d^S the solid-liquid adsorption and desorption coefficient respectively, $S(r, z, t)$ the amount of adsorbed surfactant per unit of volume and S_∞ the maximum adsorbed surfactant concentration per unit of volume. The $\frac{4}{d}$ prefactor originates from the expression for the area of the channel walls A_p for a given control volume $V = A_p d / (4\eta)$ (see [164] for a derivation). At $t = 0$ no surfactant has adsorbed on the pore walls ($S(r, z, 0) = 0$).

As an equation of state for the surface tension of the solid-liquid interface σ_{sl} a variant of the Sheludko equation [86, 160] is used:

$$\sigma_{sl} = \sigma_{sl,0} \left(1 + \frac{S}{S_\infty} \left((\sigma_{sl,0} / \sigma_{sl,\infty}) - 1 \right) \right)^{-3}. \quad (5.31)$$

Here, $\sigma_{sl,0}$ and $\sigma_{sl,\infty}$ are the surface tensions of a surfactant-free and fully covered interface respectively. Equation (5.31) is appropriate for surfactant concentrations that

approach the maximum, which is the case in this work for the liquid-solid interface. Hence, this equation of state is used rather than e.g. the Szyszkowski equation that is used for the liquid-air interface.

The reduction in interfacial tension will affect the suction pressure, which is implied by Young's equation: $\sigma_{sg} - \sigma_{sl} = \sigma_{lg} \cos \theta_{adv}$, with solid-gas interfacial tension σ_{sg} . Substitution of the left-hand side of Young's equation in Equation (5.16) results in

$$p_c = -\frac{4(\sigma_{sg} - \sigma_{sl}(\bar{S}_{int}))}{d}. \quad (5.32)$$

Adsorbing surfactants will therefore increase the magnitude of the capillary suction pressure. The volume-averaged value of $S(r, z, t)$ at the interface, i.e. \bar{S}_{int} , is used for calculation of p_c . This results in better stability, since p_c becomes more uniform.

The surfactant concentration at the liquid-air interface in the porous medium is not taken into account, because it does not affect p_c (as shown by [99, 100]). Furthermore, due to the adsorption kinetics $\psi \gg \Gamma$, meaning that adsorption onto the liquid-air interface has no significant influence on the bulk concentration. This type of surfactant is typically called a 'penetrant' and is used to influence liquid absorption.

The numerical procedure that is employed to solve the equations outlined in this section, is given in Subsection 2.9.

5.3. Results and discussion

In this section the results of the simulations are presented and discussed. First, pure droplets with both pinned and moving contact lines are considered and quantitatively compared with experimental literature. After that, droplets with surfactants are examined and results are shown to be consistent with literature as well.

5.3.1. Pure droplets

Droplets with both a pinned contact line and a moving contact line can be absorbed by a porous substrate. This results in different shapes of the absorbed wetted region as can be seen in Figure 5.1. In the pinned case (5.1a) the depth profile in the porous medium propagates with a flat front and the wetted region also tends to expand in radial direction. In the unpinned cases (5.1b, c, d), however, the wetting front becomes increasingly parabolic in shape and the 'contact line' in the porous medium behaves as if it were pinned. This behavior seems to be independent of initial contact angle, although the final shape becomes flatter as the initial contact angle is decreased, because of the change in aspect ratio of the droplet.

Note that decreasing the initial contact angle can be done in two ways: changing the initial radius, while keeping the initial volume constant (Figure 5.1c) and changing the initial volume, while keeping the initial radius constant (Figure 5.1d). Regardless of the way in which the initial contact angle is reduced, the qualitative behavior remains the same: a relatively flatter wetted region.

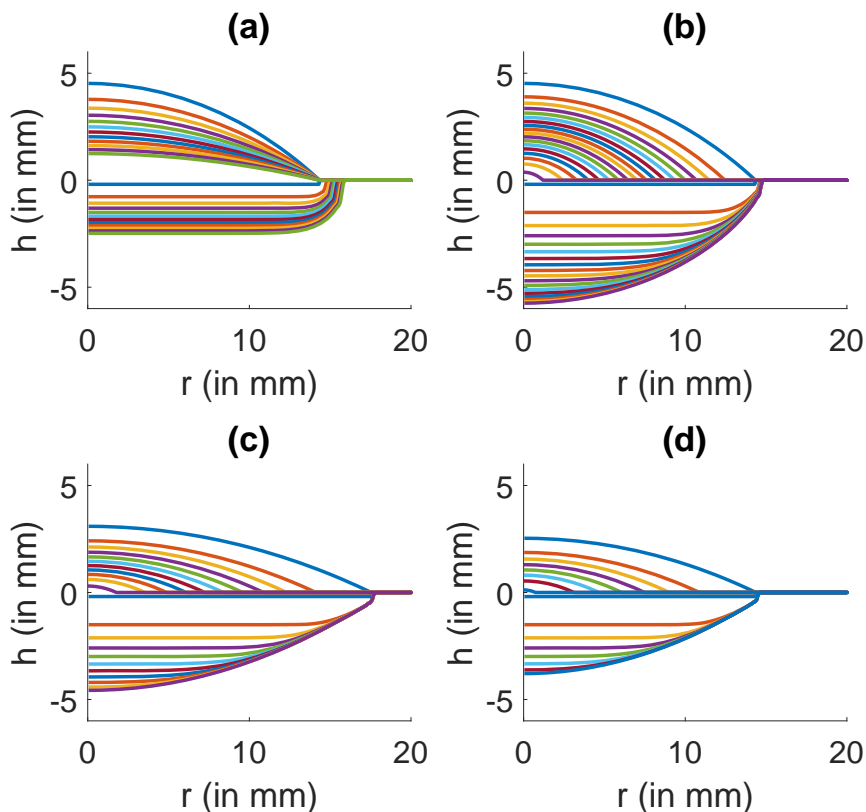


Figure 5.1.: Typical height profile evolution for (a) a pinned contact line with $\theta_0 = 35^\circ$ and moving contact lines (b) with $\theta_0 = 35^\circ$, (c) with $\theta_0 = 20^\circ$ while keeping the initial volume the same as for $\theta_0 = 35^\circ$ and (d) with $\theta_0 = 20^\circ$ while keeping the initial radius the same as for $\theta_0 = 35^\circ$. In (a) the largest (blue) drop profile depicts $t = 0$ and each subsequent, smaller drop profile indicates a time interval of $0.5s$ up to $5.5s$ for the smallest drop. Similarly, in (b,c,d) each smaller drop profile indicates a time interval of $2s$ up to $34s$, $20s$ and $14s$, respectively. Note that for the smallest drop profile the wetted region is largest.

An explanation for these differences and similarities can be found by analyzing the pressure in the porous medium, as for example given by Figure 5.2. The pressure right underneath the droplet is equal to the Laplace pressure in the droplet ($\sim O(1)$ Pa) and from there decreases towards the edge of the wetted region, where the pressure equals the capillary pressure. The vertical gradient towards the horizontal wetting front is more or less identical for all cases, while the horizontal gradient towards the side of the wetted region is different, because of the differences in contact radii. Since for the moving contact line cases, the droplet contact line moves away from the wetted region contact line, there is barely any radial expansion. This is not the situation for the pinned contact line case, because there the droplet contact line remains close to

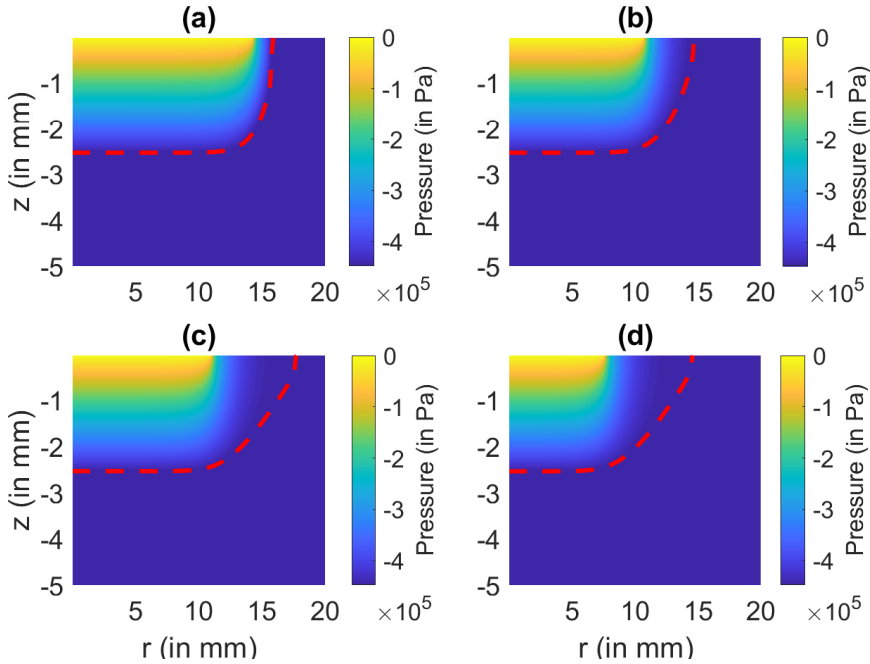


Figure 5.2.: Typical pressure plots for (a) a pinned contact line with $\theta_0 = 35^\circ$ and moving contact lines (b) with $\theta_0 = 35^\circ$, (c) with $\theta_0 = 20^\circ$ while keeping the initial volume the same as for $\theta_0 = 35^\circ$ and (d) with $\theta_0 = 20^\circ$ while keeping the initial radius the same as for $\theta_0 = 35^\circ$. Note the differences in shape of the wetted volume and in pressure on the side. The red dashed lines indicate the position of the wetting front.

the wetted region contact line, giving it the opportunity to expand in radial direction as well. The same mechanism also explains the differences in shape of the wetted regions: as the contact area shrinks for the moving contact line cases, an increasing proportion of the wetted region stops expanding, because it is too far away from the droplet in radial direction.

This behavior can also be observed in the depth and volume evolution of the wetted region. As can be seen in Figure 5.3 the penetration depth H_p , defined as the deepest point of the wetted region, evolves nearly identical for both the pinned and unpinned cases. However, the final penetration depth tends to be larger for the unpinned cases, because of the shape of the wetted region. Since for the unpinned cases the contact area shrinks over time, the result is a more pointed shape than for the pinned case (also see Figure 5.1) and a relatively slower volume evolution, as seen in Figure 5.3b. It also shows that decreasing the initial contact angle generally increases the absorption rate: for the constant initial volume because the total contact area becomes larger and for the constant initial radius because the total volume to be absorbed becomes smaller.

Note that the pinned contact line case seems to have a smaller final absorbed volume than the other moving contact line cases with the same initial drop volume. This is, however, a result of the simulations being cut off for different remaining drop volumes.

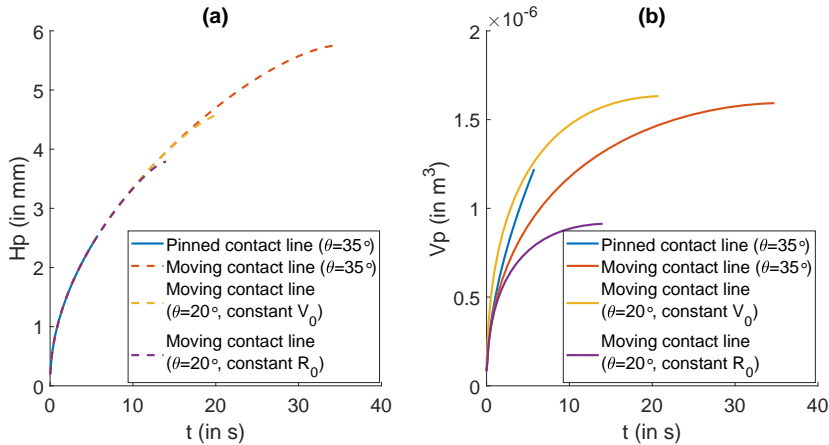


Figure 5.3.: Typical evolution plots for (a) penetration depth H_p and (b) volume of the wetted region V_p .

The pinned contact line case tends to be less stable than the moving contact line cases, because its aspect ratio changes more severely. Therefore the simulations with pinned contact lines are stopped when the remaining drop volume is larger than the drop volume that remains when the simulations with moving contact lines are stopped. The input parameters that were used for Figures 5.1, 5.2 and 5.3 are given in Section A.2 of the appendix.

The implication of these findings is that the evolution of the penetration depth is mostly independent of the shape of the liquid reservoir on the surface. However, the final penetration depth and the volume evolution do depend on this shape. These trends have not been noted before to the knowledge of the authors. A practical consequence of this is that the simulations can be compared to experiments that involve droplets, but also to experiments that use a container filled with fluid as a reservoir (1D absorption). This is illustrated in Figure 5.4, where simulation results are compared to droplet experiments by Nees (2011) [130, 164] and container experiments by Starov et al. (2004) [169].

The experiments by Nees (2011) involve a $10 \mu\text{L}$ droplet that absorbs into a porous substrate that is made by melting glass beads together. There is some spread in the experimental data, which is explained by the inhomogeneities in the porous medium. The droplet experiments agree with the predictions made by the numerical model, as can be seen in Figure 5.4a.

The experiments by Starov et al. (2004) are performed by submerging a bound nitrocellulose membrane in a liquid-filled bath, resulting in a uniform, onedimensional evolution of the liquid front. They do this for both pure water and SDS solution. As can be seen in Figure 5.4b, the droplet simulations agree well with the experiments. Note that the experimental results that are shown in Figure 5.4b were actually performed with a small SDS concentration. Starov et al. (2004) show however that in this case the results with surfactant are the same as without surfactants. Since these

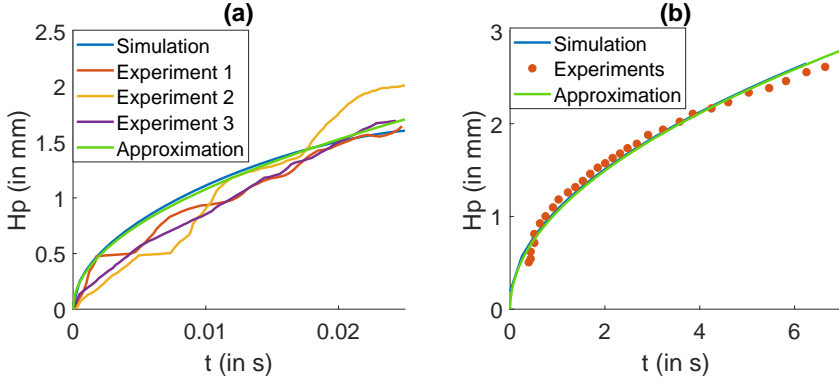


Figure 5.4.: Time evolution of penetration depth; comparison of unpinned and pinned contact line droplets, respectively, with experimental results by (a) Nees (2011) and (b) Starov et al. (2004). The input parameters that were used for the simulations are given in Section A.2 of the appendix.

were the only time-dependent results that were given in the article, they are used for this comparison with pure droplets and can safely be assumed appropriate.

In all cases the evolution of H_p can be approximated by a $H_p \sim \sqrt{t}$ relation. This follows from the fact that $\frac{\partial H_p}{\partial t} \approx \frac{\kappa}{\eta\mu} \frac{\partial p}{\partial z} \approx -\frac{\kappa}{\eta\mu} \frac{p_c}{H_p}$. Applying separation of variables and integrating both sides, shows that H_p evolves according to:

$$H_p^2 \approx -\frac{2\kappa p_c}{\eta\mu} t. \quad (5.33)$$

This approximation follows both the simulations and experiments rather well, as can be seen in Figure 5.4. As a consequence, it is possible to derive parameters (κ , p_c , η) from results by fitting a square root function to it. Subsequently, a single, unknown parameter (in this work κp_c) can be extracted from the fitted prefactor. This method will be applied in the next subsection.

5.3.2. Droplets with surfactants

When surfactants are added to the droplet, this can influence the absorption process. As surfactant molecules adsorb onto the pore walls, the capillary pressure has a tendency to increase (as implied by Equations (5.31) and (5.32)), which potentially accelerates the absorption. As for example illustrated in Figure 5.5, adding surfactants results in a faster evolution of the penetration depth H_p and absorbed volume V_p . This is indeed confirmed by literature [16, 18, 27, 169, 187]. The magnitude of the acceleration depends on the adsorbed surfactant concentration at the liquid front and is mainly limited by surface energy effects, i.e. σ_{sg} and the range of σ_{sl} (which ranges from $\sigma_{sl,0}$ to $\sigma_{sl,\infty}$). High values of σ_{sg} and low values of $\sigma_{sl,0} - \sigma_{sl,\infty}$ will typically diminish the potential for accelerated absorption by surfactants, because they decrease the relative effect of adsorbed surfactant on p_c .

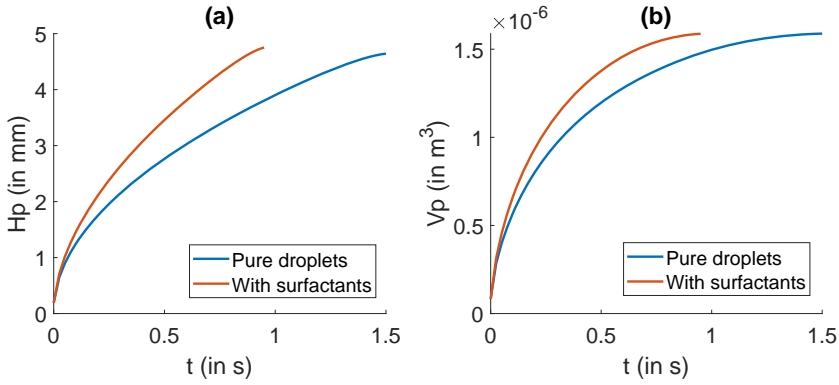


Figure 5.5.: Comparison of absorption between a pure droplet and a 50 mM surfactant solution droplet. (a) shows the evolution of the penetration depth H_p and (b) the evolution of the absorbed volume V_p . The pore diameter is $3.0 \mu\text{m}$ for all cases.

The adsorption kinetics of the surfactant also determine whether the absorption process accelerates. As illustrated in Figure 5.6, a relatively fast adsorption causes all surfactant to be consumed before it reaches the wetting front. In Figure 5.6a there is

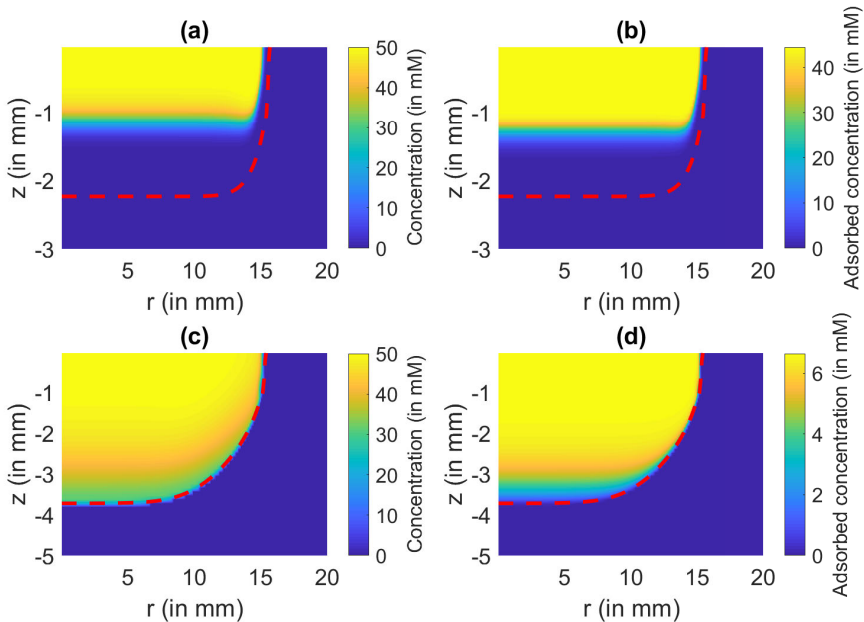


Figure 5.6.: Comparison of surfactant concentration fields between (a,b) pore diameter $d = 0.45 \mu\text{m}$ and (c,d) pore diameter $d = 3.0 \mu\text{m}$. The red dashed lines indicate the position of the wetting front.

only a significant surfactant concentration present in the top part of the wetted region,

i.e. close to the droplet, which functions as a surfactant source. However, since the adsorption kinetics are relatively fast compared to the liquid absorption, only surfactant is adsorbed in the upper part of the wetted region (see Figure 5.6b). As a result, there is no surfactant left to adsorb in the bottom part. The result is that the surfactant has no influence on the wetting properties of the liquid, because the capillary pressure is the same as for a pure liquid.

If the pore diameter is larger, however, the droplet absorbs faster, meaning that the adsorption and absorption processes have similar time scales. Furthermore, for larger pore diameters the specific surface area is smaller, hence a smaller amount of surfactant can be adsorbed. As a result, the surfactant can get closer to the wetting front before being adsorbed. This can be seen in Figure 5.6c, where the surfactant concentration is nearly uniformly distributed over the wetted region, except close to the interface, where it is smaller. Naturally, a similar concentration distribution can be found for the adsorbed concentration S (see Figure 5.6d). This causes the absorption process to accelerate, because the magnitude of the capillary pressure - and thus the pressure gradient in the wetted region - increases.

An effective way of actually quantifying the absorption process is through the value of κp_c (the product of the permeability and the capillary pressure). As shown by Equation (5.33), this product mainly determines the evolution velocity of H_p and is not known beforehand if surfactants are involved. It can be seen as the effective driving force the fluid experiences during absorption (it possesses the physical unit of a force). The value of κp_c can be found by fitting a line along H_p^2 and determining the slope.

As can be seen from Figure 5.7, the value of κp_c indeed increases with $\phi_{p,0}$ for larger pore diameters, while it remains constant for smaller pore diameters. As shown before in Figure 5.6, smaller adsorption rates (small pore diameters) will cause all surfactant to adsorb before reaching the wetting front, while larger adsorption rates (large pore diameters) result in an increase of the magnitude of p_c by surfactant. For the latter case the amount of surfactant adsorbing at the wetting front naturally increases as the surfactant concentration increases, which can be seen for $d = 3.0 \mu\text{m}$ in Figure 5.7.

This is useful data, because it shows that increasing the amount of surfactant in a solution does not necessarily accelerate the absorption. If the surfactant has adsorption kinetics that are simply too fast, it will never affect the absorption dynamics. Therefore, this could, for example, guide engineers to use a slower surfactant if an enhanced droplet absorption is desired.

Similar behavior was also found for 1D absorption by Starov et al. (2004) [169]. They performed experiments on the absorption of aqueous SDS solutions into dry nitrocellulose membranes and theoretically predicted the existence of a critical pore diameter under which surfactant does not influence the absorption process anymore. Their experiments confirmed the existence of this critical pore diameter as does this numerical work. In the case of an SDS solution on a nitrocellulose substrate this critical pore diameter is between $0.45 \mu\text{m}$ and $3.0 \mu\text{m}$, which is also found for the parameters used in this article.

As a final note, κp_c at $\phi_{p,0} = 0$ increases linearly with d , which is what would be expected from Equations (5.11) and (5.16).

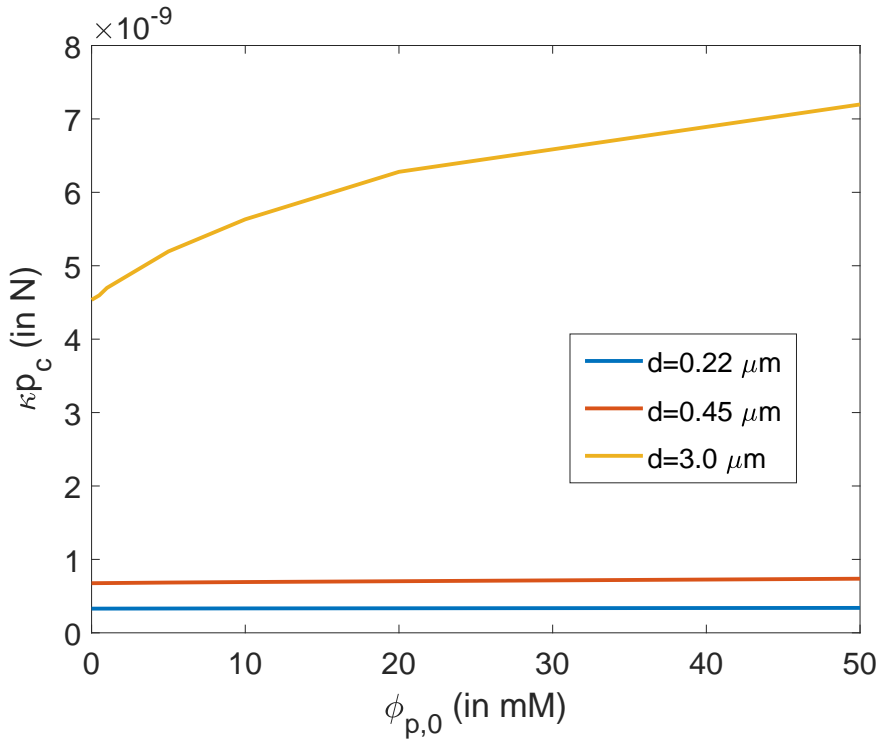


Figure 5.7.: κp_c as a function of initial surfactant concentration $\phi_{p,0}$ for several values of pore diameter d . The input parameters that were used for the simulations are given in Section A.2 of the appendix.

5.4. Conclusion

In this work a numerical model was created for the absorption of surfactant-laden sessile droplets into porous media. The droplet was modeled using axisymmetric lubrication theory and the absorption process using mass conservation and Darcy's law. In the droplet, the surfactants were considered both at the liquid-air interface and in the bulk using convection-diffusion-adsorption equations and in the porous medium the surfactants were modeled in the bulk through another convection-diffusion-adsorption equation and at the pore walls through an adsorption-equation.

The contact line of the droplet was considered for both a pinned case and an unpinned case with a slip model. It was shown that if the contact line is pinned, the droplet absorbs with a mostly flat wetting front, which also expands in radial direction. On the other hand, for a slipping contact line, the wetting front becomes increasingly parabolic in shape and the 'contact line' of the wetted region remains nearly pinned. This results in similar evolution of the penetration depth for both contact line models, while the volume of the wetted region evolves more slowly for the slip model. Therefore, the final penetration depth tends to be larger for an unpinned contact line. The evolution of the penetration depth was validated by quantitative comparison with

experimental results from literature. It was also found that a reduced initial contact angle results in faster absorption and a flatter – although still parabolic – shape of the wetted region, which is a result of the relatively larger contact area and flatter droplet.

When surfactants are involved, it was shown that there is a potential for the absorption process to accelerate. Whether this acceleration occurs depends on the time scale of the adsorption kinetics of the surfactants compared to the time scale of absorption of the droplet. Small absorption rates (small pore sizes) result in surfactant adsorbing on the pore walls before reaching the wetting front. Thus, in that case the absorption process of the surfactant-laden droplet will be indistinguishable from the absorption of a pure droplet. If the absorption process is fast (for large pore sizes), however, surfactant does adsorb at the wetting front, resulting in more suction. As a consequence, the absorption rate will increase with initial surfactant concentration if the pore size is large enough. These results are in agreement with 1D experimental and analytical results by Starov et al. (2004) [169].

These findings agree with the hypothesis that was made before, namely that a moving contact line slows down the absorption process and that surfactants can be used to accelerate the absorption. This acceleration only happens if the absorption – before taking into account surfactants – is fast enough.

Possible applications lie in the ability to control the absorption rate, final penetration depth and final shape of the wetted region. For example, if the wetted region requires a final shape that is mostly flat, it helps to add components that promote pinning, such as surfactants that reduce the contact angle [58, 156]. Furthermore, if the absorption needs to be accelerated, it is important to choose a surfactant that does not adsorb too fast (typically larger surfactants) and that have a tendency to adsorb onto the liquid-solid interface. These type of methods for control can be employed in several technologies that involve porous media, such as inkjet printing, irrigation and medical treatments that involve absorption through the skin.

Previous numerical studies often employed 1D absorption models [118, 119, 120, 169] rather than 2D or 3D and although there are several articles on 2D or 3D droplet absorption models [2, 3, 33, 34, 57, 144, 145, 193], none considered the effect of the contact line dynamics and/or involved surfactants. Furthermore, while a significant number of experimental studies on surfactant-enhanced liquid absorption has been carried out [123, 129, 134, 147, 174], it tends to be rather difficult to actually visualize the flow, let alone to quantify properties as pressure and surfactant concentration. Therefore, numerical studies, like this one, are a valuable contribution to the field.

Further research opportunities lie in additional parametric analysis of the relevant surfactant properties and comparison with experiments. While extensive analysis has been done on the effect of several dimensionless numbers on the absorption of pure droplets (e.g. [2, 164]), this has not been done for surfactants. This article has made a first step in that direction. Furthermore, experimental studies that systematically consider the effect of different surfactants on absorption are rare. This would be a requirement for validating potential numerical results.

Also, Molecular Dynamics (MD) simulations can help to increase the accuracy of our model. In the initial stages of the absorption process and for nanoscale pores the

current hydrodynamic model tends to be less valid. For both these limits, MD simulations can offer corrections to the equations (e.g. see [116, 175, 176]). Furthermore, MD models can be employed to get better insight into the adsorption kinetics of surfactants and the factors that influence this process. This way, it becomes possible to compare our model quantitatively with experiments, because real-life surfactants can be implemented if their adsorption parameters are known [54, 184].

An additional suggestion for improving the model is to define a local capillary pressure rather than one that is averaged over the wetting front. This would allow one to capture more details of the flow. The corresponding numerical instabilities may be solved by employing a different, 2D method to define the interface position, since in the current model this is done by a 1D height profile $h_p(r)$. Also, in many cases porous substrates swell as a result of the absorbed liquid (e.g. paper, see [118, 119, 120]), which can be modeled as well. Furthermore, the consideration of volatile fluids, i.e. simultaneous evaporation and imbibition, is of relevance and can be taken into account in future studies.

6. Particle dynamics in evaporating droplets with soluble surfactants

In this chapter it is explored how particles can be implemented as a solute in a droplet and how the particle dynamics are affected by the fluid flow. Several methods are introduced and their limitations are analyzed. Furthermore, the particle dynamics as given by the lubrication model are considered both with and without soluble surfactants. It is shown that lubrication theory is limited when it comes to the velocity field and particle dynamics close to the contact line.

6.1. Introduction

Many applications involve particle-laden droplets. Technologies like inkjet-printing [138], micro-arrays [140], coatings [63] and detection of drugs [195] all involve drying colloidal suspensions in the form of droplets. Here, the final deposition of the solute after evaporation is of key importance, because the deposition pattern is often nonhomogeneous due to the coffee-stain effect. As shown by Deegan et al. [35, 36, 37], the evaporation of a sessile droplet on an amphiphilic substrate occurs fastest close to the contact line. Furthermore, because the droplet tends to a spherical cap shape, a constant flow towards the contact line occurs that results in ring formation.

Various promising attempts have been made to counteract the coffee-stain effect. It has been stated that factors as Marangoni flow [73, 112], the wettability of the substrate [124], the particle-substrate adherence [125], the particle shape [194] and the particle electric charge [132] are all of relevance in counteracting the coffee-stain effect.

In order to get better insight in the nature of the underlying particle dynamics during drop evaporation and to control it, accurate models are of great importance. The advantage of models is that they are transparent and show details that experiments generally cannot provide. Also, models are easier and cheaper to do large parameter sweeps.

In this chapter several models are introduced for particle dynamics in droplets in the framework of lubrication theory. Each of these methods is evaluated in terms of suitability and consistency. For the most simple model of the two, which considers the particles as passive tracers, two different cases are analyzed: (1) a pure droplet where there is only flow towards the contact line and thus the coffee-stain effect should occur and (2) a surfactant-laden droplet where there is Marangoni circulation [59] and thus the coffee-stain effect should at least be slightly suppressed. For the more complex model of the two, which considers the particles as a distinct phase besides the fluid, it is explored how to deal with concentrations close to the maximum packing fraction.

In Section 6.2 the mathematical model is covered. First, the droplet evolution model is introduced and then the surfactant transport equations. After that, the two solute

models are outlined. In Section 6.3 the tracer particle model is considered first for both a pure droplet case and for a case where a droplet contains surfactants. It is examined how the calculation of the velocity field can be improved to describe the actual particle fluxes better. After that, the two-phase particle model is analyzed and it is explored how it can deal with concentrations up to and including the maximum packing fraction. Lastly, this chapter finishes with a conclusion in Section 6.4.

6.2. Mathematical model

In this section the mathematical model for the droplet, the surfactants and evaporation are covered. Furthermore, the two different particle models are introduced.

6.2.1. Droplet evolution

Consider a relatively flat droplet with radius R , height H and contact angle θ that sits on an amphiphilic substrate ($\theta < 90^\circ$ and $\epsilon = H/R \ll 1$). The droplet consists of a fluid with mass density ρ , dynamic viscosity μ and (liquid-air) surface tension σ_{lg} and it has a Bond/Eötvös number much smaller than one ($Bo = \frac{\rho g H^2}{\sigma_{lg}} \ll 1$), meaning that gravity has no significant effect on its shape.

A cylindrical coordinate system (r, α, z) is used for the equations and it is assumed that the droplet has an axisymmetric geometry ($\frac{\partial}{\partial \alpha} = 0$) and that no swirl occurs (angular velocity $U_\alpha = 0$). Furthermore, isothermal conditions are assumed, meaning that fluid properties will not change due to temperature variations. The contact line is pinned since one of the main interests in this chapter is the coffee-stain effect, which generally only occurs in combination with a constant contact radius R [113].

Since the aspect ratio of the droplet ϵ is small, the droplet evolution can be described using lubrication theory. As derived in Section 2.1, the shape is then given by a height profile $h(r, t)$ and the corresponding velocity field by:

$$u(r, z, t) = \frac{1}{\mu} \left(-\frac{\partial p}{\partial r} \left(hz - \frac{1}{2} z^2 \right) + \frac{\partial \sigma_{lg}}{\partial r} z \right); \quad (6.1)$$

$$w(r, z, t) = \frac{1}{\mu} \left(\frac{1}{r} \frac{\partial}{\partial r} \left(r \frac{\partial p}{\partial r} \right) \left(\frac{1}{2} h z^2 - \frac{1}{6} z^3 \right) + \frac{1}{2} z^2 \left(\frac{\partial h}{\partial r} \frac{\partial p}{\partial r} - \frac{1}{r} \frac{\partial}{\partial r} \left(r \frac{\partial \sigma_{lg}}{\partial r} \right) \right) \right). \quad (6.2)$$

Applying the kinematic boundary condition $\partial_t h + (\partial_r h)u|_{z=h} = w|_{z=h} + w_e$ the evolution over time can be found:

$$\frac{\partial h}{\partial t} = \frac{1}{r\mu} \frac{\partial}{\partial r} \left(\frac{r h^3}{3} \frac{\partial p}{\partial r} - \frac{r h^2}{2} \frac{\partial \sigma_{lg}}{\partial r} \right) + w_e. \quad (6.3)$$

Here, w_e is the evaporation volume flux and p the pressure in the droplet. Evaporation flux w_e is given by:

$$w_e = \frac{D_v M_l p_{sat,l} (1 - RH)}{\rho R_u T} \frac{\partial \hat{p}_l}{\partial n} \sqrt{1 + \left(\frac{\partial h}{\partial r} \right)^2}, \quad (6.4)$$

where D_v is the vapor diffusivity, M_l the molar mass of the fluid, $p_{sat,l}$ the saturation pressure of the fluid and RH the relative humidity. Furthermore, $\frac{\partial \tilde{p}_l}{\partial n}$ is the non-dimensional normal derivative of the vapor pressure and is obtained by solving the integral in Equation (2.71).

Pressure p is given by the Laplace pressure:

$$p = -\frac{1}{r} \frac{\partial}{\partial r} \left(\sigma_{lg} \frac{r \partial_r h}{\sqrt{1 + (\partial_r h)^2}} \right). \quad (6.5)$$

The corresponding boundary and initial conditions are:

$$\left(\frac{\partial h}{\partial r} \right)_{r=0} = 0, \quad (6.6)$$

$$\left(\frac{\partial^3 h}{\partial r^3} \right)_{r=0} = 0, \quad (6.7)$$

$$h(R, t) = 0, \quad (6.8)$$

$$h(r, 0) = h_0(r), \quad (6.9)$$

which denote the symmetry condition at the origin, the position of the contact line and the initial drop shape $h_0(r)$, which is a spherical cap with height H .

6.2.2. Surfactant evolution

Both at the interface and in the bulk there is a surfactant present with concentration $\Gamma(r, t)$ and $\phi(r, t)$, respectively. The evolution of interfacial concentration $\Gamma(r, t)$ is given by:

$$\frac{\partial \Gamma}{\partial t} = -\vec{\nabla}_s \cdot (\Gamma \vec{u}_t) - \Gamma U_n \vec{\nabla}_s \cdot \vec{n} + D_\Gamma \vec{\nabla}_s^2 \Gamma + \frac{\partial h}{\partial t} \frac{\partial_r h}{1 + (\partial_r h)^2} \frac{\partial \Gamma}{\partial r} + J_{\Gamma \phi}. \quad (6.10)$$

Here, $\vec{\nabla}_s$ is the surface gradient operator, \vec{u}_t the velocity vector tangential to the liquid-air interface, U_n the magnitude of the velocity normal to the interface, \vec{n} the normal of the interface, D_Γ the interfacial diffusion coefficient and $J_{\Gamma \phi}$ the adsorption from the bulk, which will be defined later on. The surface gradient operator in cylindrical coordinates is $\vec{\nabla}_s = \frac{1}{1 + (\partial_r h)^2} \vec{e}_r \frac{\partial}{\partial r} + \frac{\partial_r h}{1 + (\partial_r h)^2} \vec{e}_z \frac{\partial}{\partial r} + \frac{1}{r} \vec{e}_\alpha \frac{\partial}{\partial \alpha}$. Any dependency of z is dropped here, since $\vec{\nabla}_s$ will only be applied to variables that depend on r and t . The tangential velocity vector is given by $\vec{u}_t = \vec{u} \cdot (I - \vec{n} \vec{n})$, the normal velocity magnitude is given by $U_n = \frac{\partial_t h}{\sqrt{1 + (\partial_r h)^2}}$ and the surface normal is $\vec{n} = -\frac{\partial_r h}{\sqrt{1 + (\partial_r h)^2}} \vec{e}_r + \frac{1}{\sqrt{1 + (\partial_r h)^2}} \vec{e}_z$.

Interfacial concentration $\Gamma(r, t)$ is subject to the following boundary and initial condi-

tions:

$$\left(\frac{\partial\Gamma}{\partial r}\right)_{r=0} = 0; \quad (6.11)$$

$$\left(\frac{\partial\Gamma}{\partial r}\right)_{r=R} = 0; \quad (6.12)$$

$$\Gamma(r, 0) = \Gamma_0. \quad (6.13)$$

These denote the symmetry condition at the origin, the no-flux condition at the contact line and the initially homogeneous surfactant distribution, respectively.

The presence of surfactant at the interface will reduce the interfacial surface tension σ_{lg} . In this work, the Szyszkowski/Frumkin equation of state is used for this purpose, which takes into account the finite space surfactants occupy at the interface:

$$\sigma_{lg} = \sigma_{lg,0} + R_u T \Gamma_\infty \ln \left(1 - \frac{\Gamma}{\Gamma_\infty}\right). \quad (6.14)$$

Here, $\sigma_{lg,0}$ is the surfactant-free surface tension, R_u is the ideal gas constant, T the temperature and Γ_∞ the maximum concentration (which is the inverse of the space a single surfactant monomer requires).

Regarding the bulk concentration $\phi(r, t)$ it is more convenient to express the evolution in terms of $\psi(r, t) \equiv \phi(r, t)/h(r, t)$. The corresponding evolution equation is then given by:

$$\frac{\partial\psi}{\partial t} = \frac{1}{r} \frac{\partial}{\partial r} \left(\frac{rh^2\psi}{3\mu} \frac{\partial p}{\partial r} - \frac{rh\psi}{2\mu} \frac{\partial\sigma_{lg}}{\partial r} + D_\phi rh \frac{\partial\phi}{\partial r} \right) - J_{\Gamma\phi} \sqrt{1 + (\partial_r h)^2}. \quad (6.15)$$

Here, D_ϕ is the bulk diffusion coefficient of the surfactant.

Similar to $\Gamma(r, t)$, the bulk concentration $\psi(r, t)$ is subject to the boundary and initial conditions:

$$\left(\frac{\partial\psi}{\partial r}\right)_{r=0} = 0; \quad (6.16)$$

$$\left(\frac{\partial\psi}{\partial r}\right)_{r=R} = 0; \quad (6.17)$$

$$\psi(r, 0) = \phi_0 h(r, 0). \quad (6.18)$$

The surfactant adsorption rate $J_{\Gamma\phi}$ is given by:

$$J_{\Gamma\phi} = k_a^\Gamma \phi \left(1 - \frac{\Gamma}{\Gamma_\infty}\right) - k_d^\Gamma \Gamma, \quad (6.19)$$

where the adsorption rate is limited by the bulk concentration $\phi(r, t)$ and the available space at the interface, while the desorption rate is limited by the interfacial concentration $\Gamma(r, t)$.

6.2.3. Solute transport

In many applications there is a nonvolatile solute present in the droplet that remains on the substrate after complete evaporation [35, 73]. In order to model this deposition pattern accurately, it is required to track the transport of the solute during the drying process. In this subsection two different models are introduced: one that considers the particles as a concentration without volume, which is called the ‘tracer particle model’, and one that considers the particles as a distinct phase, which is called the ‘two-phase model’.

Tracer particle model

Perhaps the simplest way to model a solute is to consider it as a passive, massless tracer particle concentration that does not influence the fluid flow in any way. In that case, the evolution of the solute concentration $C(r, z, t)$ can be described by a simple 2D convection-diffusion equation:

$$\frac{\partial C}{\partial t} = -\frac{1}{r} \frac{\partial}{\partial r}(rCu) - \frac{\partial}{\partial z}(Cw) + D_C \frac{1}{r} \frac{\partial}{\partial r} \left(r \frac{\partial C}{\partial r} \right) + D_C \frac{\partial^2 C}{\partial z^2}. \quad (6.20)$$

Here, D_C is the bulk diffusion coefficient of the solute. The following boundary and initial conditions hold:

$$\frac{\partial C}{\partial r} \Big|_{r=0} = 0; \quad (6.21)$$

$$\frac{\partial C}{\partial z} \Big|_{z=0} = 0; \quad (6.22)$$

$$-\frac{\partial h}{\partial r} \frac{\partial C}{\partial r} \Big|_{z=h} + \frac{\partial C}{\partial z} \Big|_{z=h} = 0; \quad (6.23)$$

$$C(r, z, 0) = C_0. \quad (6.24)$$

These denote the symmetry condition at the center of the droplet, the no-penetration condition at the substrate surface, the no-penetration condition at the liquid-air interface and the initially homogeneous solute distribution C_0 , respectively.

In several practical applications, such as DNA micro arrays [44], the solute adsorbs onto the substrate over time. This process is also taken into account in this work, one reason being that it offers a useful validation for the final deposition pattern. In this work the model proposed by Kurrat et al. [95, 96, 164] is employed, which is typically valid for biomolecules such as proteins. Here, the adsorbed mass per unit area $M(r, t)$ is split in a reversible portion $M_r(r, t)$ and an irreversible portion $M_i(r, t)$. The adsorption process of these two portions is modeled as:

$$\frac{\partial M_r}{\partial t} = k_a^C C \Phi - k_d^C M_r / \sqrt{\Phi}; \quad (6.25)$$

$$\frac{\partial M_i}{\partial t} = k_s^C C \Phi. \quad (6.26)$$

Here, k_a^C and k_d^C denote the reversible adsorption and desorption coefficients, respectively, and k_s^C is the irreversible adsorption coefficient. The parameter Φ is defined as

the fraction of the surface that can be occupied by solute particles and it is given by the Langmuir expression $\Phi = 1 - \Theta$. In this expression, Θ is a function of the total adsorbed mass per unit area $M(r, t)$ and is given by $\Theta = \frac{M(r, t)a}{m}$, with a the area a single biomolecule occupies and m its mass [164].

Two-phase model

The assumption that the solute acts as a passive tracer is only valid for small concentrations where the mass and volume of the particles is negligible compared to the fluid mass and volume. For higher concentrations it is required to consider the particles as a distinct, solid phase. In that case, both the fluid and the particles are assigned a mass fraction $y_w(r, z, t)$ and $y_s(r, z, t)$, respectively, and they can be described by the following evolution equation (e.g. see [39, 143]):

$$\rho \left(\frac{\partial y_a}{\partial t} + \vec{U} \cdot \nabla y_a \right) = \nabla \cdot (\rho D_{ls} \nabla y_a) - \dot{m}_a \delta_h. \quad (6.27)$$

In this equation, y_a is the mass fraction of phase a (either liquid w or solid s), D_{ls} the mutual diffusion coefficient between the phases, \dot{m}_a the evaporative mass flux of phase a and δ_h the interface delta function. The evaporation \dot{m}_w of the fluid phase is given by Equation (2.56) and the evaporation \dot{m}_s of the solid phase is zero.

The boundary and initial conditions are the same for $y_a(r, z, t)$ as for $C(r, z, t)$ and therefore Equations (6.21) – (6.24) are valid as well if $C(r, z, t)$ is replaced by $y_a(r, z, t)$.

Since the droplet now consists of two components, the average fluid properties $\rho(r, z, t)$, $\mu(r, z, t)$ and $D_{ls}(r, z, t)$ are functions of time and space. In this work, the mass density $\rho(r, z, t)$ is calculated as the harmonic mean between the densities of the phases, weighted by the local mass fractions, the dynamic viscosity $\mu(r, z, t)$ is calculated by the Krieger-Dougherty relation [92] and the mutual diffusion coefficient $D_{ls}(r, z, t)$ is estimated through Einsteinian diffusion [52] (and is thus inversely proportional to $\mu(r, z, t)$). Note that, $\sigma_{lg}(r, t)$ is not considered a function of y_a , because the solid phase does not have a surface tension of itself. Therefore, only the surface tension of the fluid is used (although it can still change due to the presence of surfactants).

Given that these fluid properties are no longer constant, a more generalized form for the velocity field should be employed. This can be derived as [39]:

$$u(r, z, t) = \int_0^z \frac{(-\partial_r p(r, t))(h(r, t) - z') + \partial_r \sigma_{lg}(r, t)}{\mu(r, z', t)} dz'; \quad (6.28)$$

$$w(r, z, t) = \frac{1}{\rho(r, z, t)} \int_0^z \left(\frac{1}{r} \frac{\partial}{\partial r} (r \rho(r, z', t) u(r, z', t)) - \frac{\partial \rho(r, z', t)}{\partial t} \right) dz'. \quad (6.29)$$

Furthermore, the evolution equations for $h(r, t)$, $\Gamma(r, t)$ and $\psi(r, t)$ also need to be

modified accordingly:

$$\frac{\partial h}{\partial t} = \frac{1}{\rho|_{z=h}} \left(-\frac{1}{r} \frac{\partial}{\partial r} \int_0^h r \rho u dz - \int_0^h \frac{\partial \rho}{\partial t} dz \right) + w_e; \quad (6.30)$$

$$\frac{\partial \Gamma}{\partial t} = -\vec{\nabla}_s \cdot (\Gamma \vec{u}_t) - \Gamma U_n \vec{\nabla}_s \cdot \vec{n} + D_\Gamma \vec{\nabla}_s^2 \Gamma + \frac{\partial h}{\partial t} \frac{\partial_r h}{1 + (\partial_r h)^2} \frac{\partial \Gamma}{\partial r}; \quad (6.31)$$

$$\frac{\partial \psi}{\partial t} = \frac{1}{r} \frac{\partial}{\partial r} \left(-\frac{r\psi}{h} \int_0^h u dz + D_\phi r h \frac{\partial \phi}{\partial r} \right). \quad (6.32)$$

This transport model in its current form holds for higher concentrations, but breaks down when the solid mass fraction $y_s(r, z, t)$ approaches its maximum packing fraction $y_{s,max}$. In that case additional modifications are required, which will be discussed in Section 6.3.

An outline of the numerical solution procedure is given in Section 2.9.

6.3. Results and discussion

In this section the two particle models presented in the previous section are tested. First, the tracer particle model is applied to a pure droplet case and to a surfactant-laden droplet case. After that, it is examined how the two-phase model can be employed for concentrations up to and including the maximum packing fraction.

6.3.1. Tracer particle model

The first solute model, the tracer particle model, is tested for two different cases. The first case is a pure droplet, where there is an outward, capillary flow due to evaporation being fastest at the contact line (see Figure 6.1a). Here, the coffee-ring effect should occur [35] and thus the thickness of the deposition layer predicted by the model should increase towards the contact line with a maximum at $r = R$. The second case is a droplet with soluble surfactants, where there is, besides the outward capillary flow, also an inward, surfactant-induced Marangoni flow [59] (see Figure 6.1b). This results in a circulating flow and thus the model should yield a more homogeneous deposition pattern compared to the pure droplet case [73, 112].

However, running the two cases for the tracer particle model yields nearly identical deposition patterns. As can be seen in Figure 6.2 in both cases a coffee-stain pattern is formed. For the surfactant case the peak is even slightly sharper than for the pure case, although the peak of the pure case is broader resulting in approximately the same deposited mass close to the contact line.

Also, for both cases the concentration plots in Figure 6.3 show that the solute accumulates at the contact line. This holds also for the surfactant case (in Figure 6.3b) despite the backflow that was observed in Figure 6.1b.

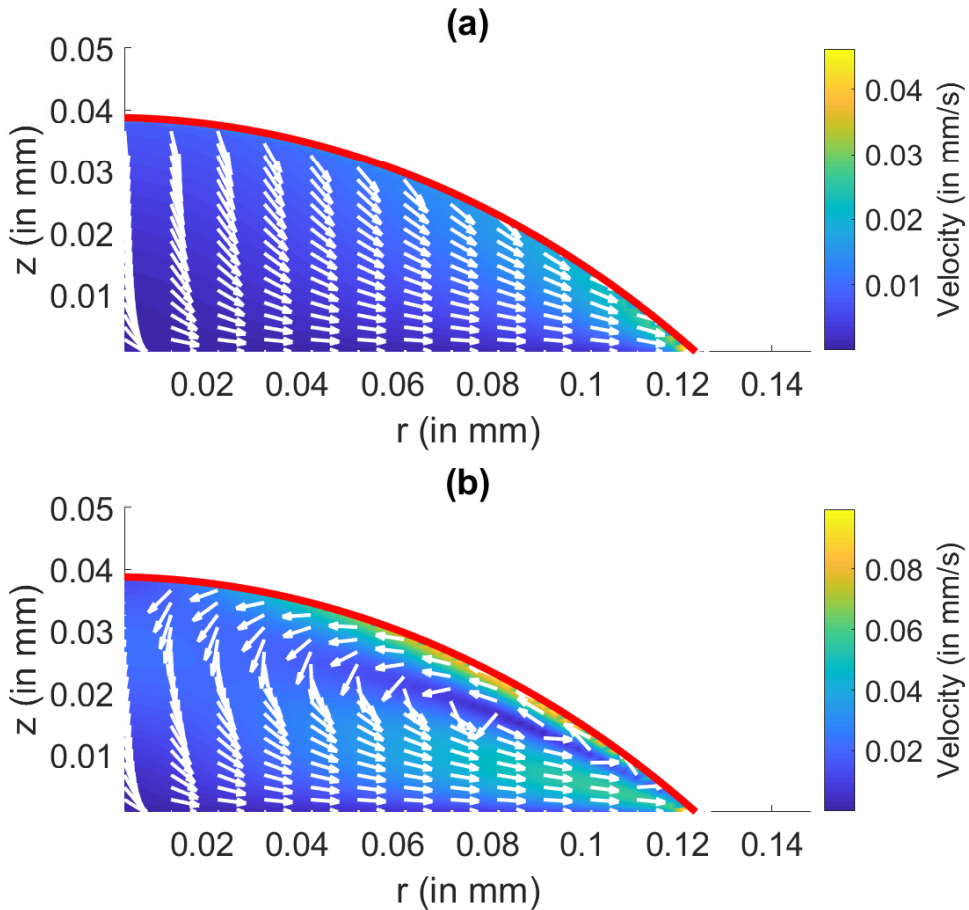


Figure 6.1.: Two different flow patterns: (a) Outward capillary flow, (b) Surfactant-induced Marangoni circulation. The red line indicates the position of the interface, given by $h(r)$.

Inspecting the flow field around the contact line for the surfactant case, reveals that in the region closest to R all velocity vectors have a positive radial component (see Figure 6.4). This explains why the solute cannot really escape from the contact line region: as soon as it comes close to the contact line, it can only flow further towards R . Several numerical tests show that this behavior is independent of the grid resolution in both the radial direction and the axial direction.

A potential, although ad-hoc, solution for this issue lies in simply cutting off the considered velocity field close to the contact line, so the solute does not get ‘trapped’ there. However, this will only move the adsorption peak from Figure 6.2 closer to the drop center, because solute still accumulates close to the contact line, but now at the location of the cut-off. This happens because the solute is not transported upwards to the interface after it arrives at the cut-off location. The axial velocity $w(r, z, t)$ is negli-

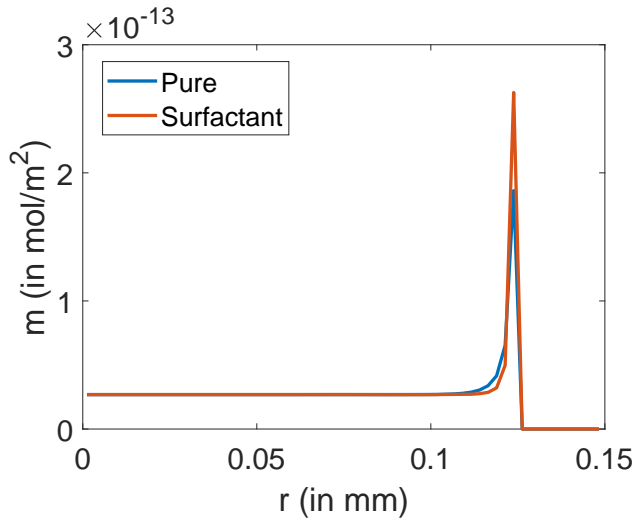


Figure 6.2.: Typical deposition pattern $m(r, t)$ for the pure droplet case and the surfactant case.

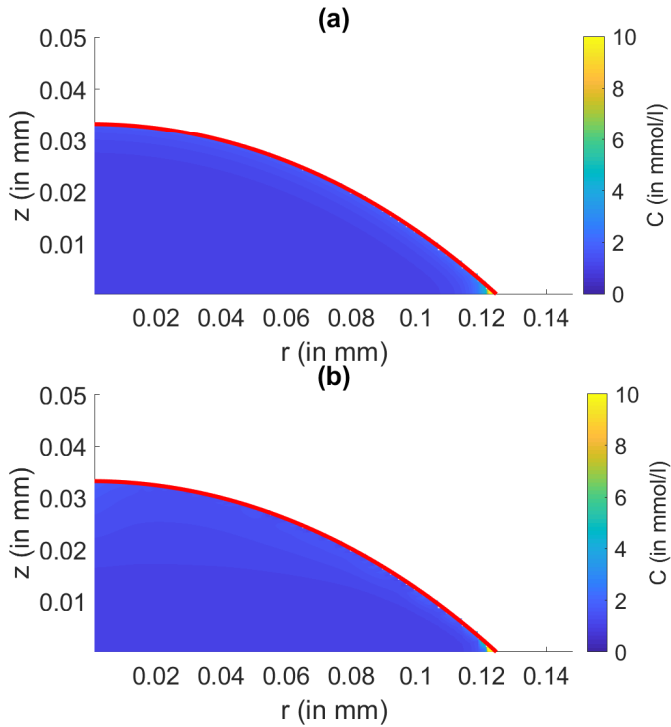


Figure 6.3.: Typical solute distribution $C(r, z, t)$ for (a) the pure droplet case and (b) the surfactant case.

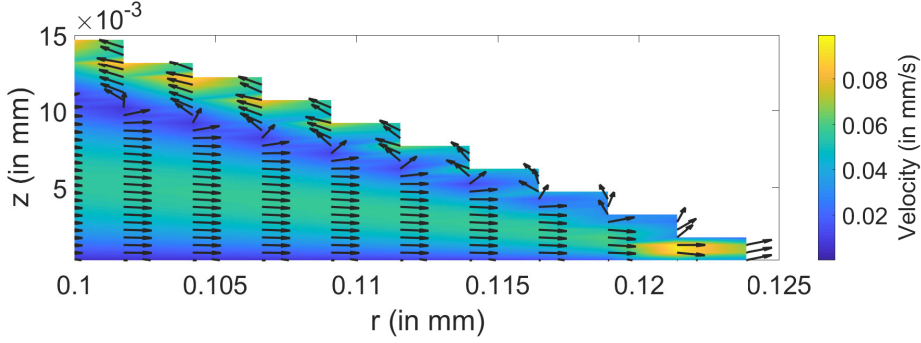


Figure 6.4.: Close up of the velocity field close to the contact line for a case with surfactants.

gible there compared to the radial velocity $u(r, z, t)$ and diffusion is also not significant enough.

This implies that more sophisticated solutions should be considered in order to solve this problem. Hu and Larson indicate that the standard formulation for the interfacial shear stress $\tau_{rz}|_{z=h(r,t)}$ in lubrication theory tends to be less accurate close to the contact line, because the $\partial w/\partial r|_{z=h(r,t)}$ term is dropped [71, 72]. Instead, they use the entire interfacial shear stress in their calculations:

$$\tau_{rz}|_{z=h(r,t)} = \mu \left(\frac{\partial u}{\partial z}|_{z=h(r,t)} + \frac{\partial w}{\partial r}|_{z=h(r,t)} \right) = \frac{\partial \sigma_{lg}}{\partial r}. \quad (6.33)$$

This will introduce an additional unknown variable $w|_{z=h}$, changing the system of equations to:

$$\frac{\partial h}{\partial t} = \frac{1}{r\mu} \frac{\partial}{\partial r} \left(\frac{rh^3}{3} \frac{\partial p}{\partial r} - \frac{rh^2}{2} \frac{\partial \sigma_{lg}}{\partial r} \right) + \frac{1}{r} \frac{\partial}{\partial r} \left(\frac{1}{2} rh^2 \frac{\partial w}{\partial r} \Big|_{z=h} \right) + w_e; \quad (6.34)$$

$$\frac{\partial \Gamma}{\partial t} = -\vec{\nabla}_s \cdot (\Gamma \vec{u}_t) - \Gamma U_n \vec{\nabla}_s \cdot \vec{n} + D_\Gamma \vec{\nabla}_s^2 \Gamma + \frac{\partial h}{\partial t} \frac{\partial_r h}{1 + (\partial_r h)^2} \frac{\partial \Gamma}{\partial r} + J_{\Gamma\psi}; \quad (6.35)$$

$$\begin{aligned} \frac{\partial \psi}{\partial t} = & \frac{1}{r} \frac{\partial}{\partial r} \left(\frac{rh^2\psi}{3\mu} \frac{\partial p}{\partial r} - \frac{rh\psi}{2\mu} \frac{\partial \sigma_{lg}}{\partial r} + \frac{1}{2} rh\psi \frac{\partial w}{\partial r} \Big|_{z=h} + D_\phi rh \frac{\partial \phi}{\partial r} \right) \\ & - J_{\Gamma\psi} \sqrt{1 + (\partial_r h)^2}; \end{aligned} \quad (6.36)$$

$$\begin{aligned} w|_{z=h} = & \frac{1}{2} \frac{1}{r} \frac{\partial}{\partial r} \left(\frac{rh}{\mu} \frac{\partial p}{\partial r} \right) h^2 - \frac{1}{6} \frac{1}{r} \frac{\partial}{\partial r} \left(\frac{r}{\mu} \frac{\partial p}{\partial r} \right) h^3 - \frac{1}{2} \frac{1}{r} \frac{\partial}{\partial r} \left(\frac{r}{\mu} \frac{\partial \sigma_{lg}}{\partial r} \right) h^2 \\ & + \frac{1}{2} \frac{1}{r} \frac{\partial}{\partial r} \left(r \frac{\partial w}{\partial r} \Big|_{z=h} \right) h^2. \end{aligned} \quad (6.37)$$

Here it is assumed that $\frac{\partial w|_{z=h}}{\partial r} \approx \frac{\partial w}{\partial r}|_{z=h}$. Implementing this shear stress correction however, does not result in an improved flow field in the contact line region as can be seen in Figure 6.5. Although with the stress correction included (Figure 6.5b) there are more velocity vectors with a negative radial velocity, there is still a point where particles accumulate (around $r \approx 1.2 \cdot 10^{-4}$ m).

Besides, the velocity field itself is much more erratic and seemingly unphysical with

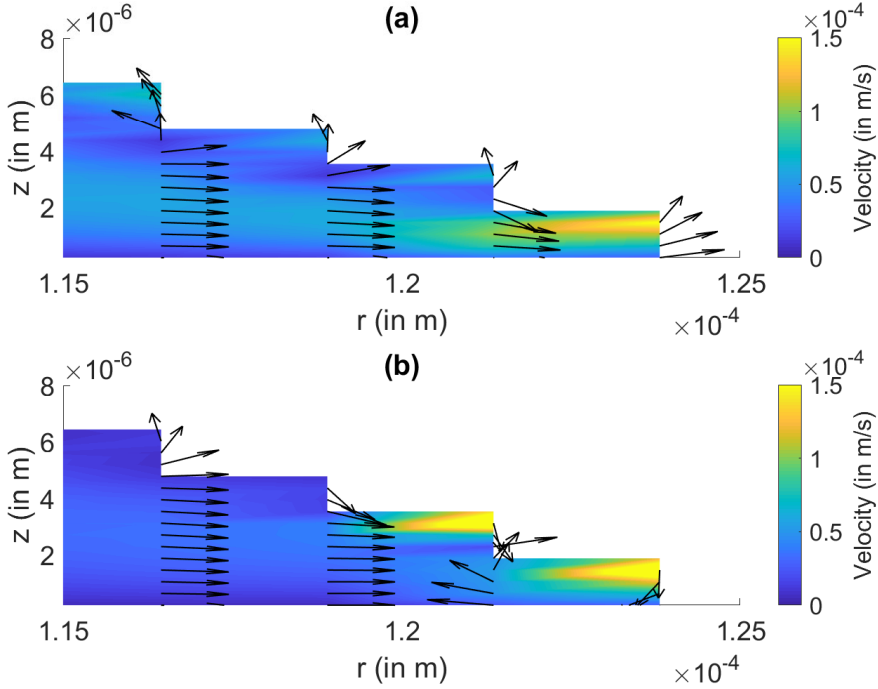


Figure 6.5.: Velocity field in the contact line region (a) without stress correction term and (b) with stress correction term.

the stress correction (Figure 6.5b) than without it (Figure 6.5a), which would imply that the correction does not actually improve the accuracy. A possible explanation for this is that the equations may not be independent of each other. The simulations in which the stress correction was added, were rather unstable and the results diverged if a fully coupled solution method was used. Only using an iterative method, where the original system of equations of $h(r, t)$, $\Gamma(r, t)$ and $\psi(r, t)$ and the equation for $w|_{z=h}$ were solved in an alternating way, results could be obtained.

In the work by Hu and Larson [71, 72], where they do implement the stress correction, this problem with instability and an erratic flow field is not encountered, because they prescribe the height evolution $\partial_t h$ and the surface tension gradient $\partial_r \sigma_{lg}$. This allows them to derive an analytical solution, which cannot be done in our case, because both the height evolution $\partial_t h$ and the surface tension gradient $\partial_r \sigma_{lg}$ are unknown.

Nevertheless, it is doubtful that neglecting the $\frac{\partial w}{\partial r}|_{z=h(r,t)}$ term in the interfacial shear stress $\tau_{rz}|_{z=h(r,t)}$ is the cause of the inaccuracy of the velocity field calculation. Computing both terms of the interfacial shear stress (see Equation (6.33)) reveals that the neglected term $\frac{\partial w}{\partial r}|_{z=h(r,t)}$ tends to be two decades smaller than the $\frac{\partial u}{\partial z}|_{z=h(r,t)}$ term, even in the contact line region. Therefore, it is justified to indeed neglect $\frac{\partial w}{\partial r}|_{z=h(r,t)}$.

As a final solution, it would be possible to impose a prescribed velocity field close to the contact line or for the droplet in its entirety. This could be done, for example, by

assuming or fitting a surface tension gradient and/or pressure gradient from which the velocity field can be calculated. This would be nontrivial however, because the velocity field is extremely sensitive to deviations in surface tension and pressure, which could be a reason why the velocity field close to the contact line does not recirculate particles properly. Furthermore, when imposing some ad-hoc velocity field it is not clear whether it is still related to the situation that we attempt to simulate. Therefore, this direction is not pursued any further in this work.

Based on all this, it is concluded that the lubrication model in its current form is not suitable for describing Marangoni circulation close to the contact line. This is probably due to certain terms in the Navier-Stokes equations being not negligible anymore close to the contact line, while being neglected in the lubrication model. Any method that is required to describe the flow field close to the contact line, should be able to deal with this issue. It is certainly possible that methods that calculate the droplet evolution in a 2D or 3D manner (rather than the 1D height profile $h(r, t)$ in lubrication theory) would perform better, since these can better adapt the mesh to the shape of the droplet and can also calculate the pressure field without neglecting terms. Alternatively, the neglected terms can be added as correction terms in the lubrication model, although this can cause several issues due to the 2D nature of these terms.

As an illustration of the effect of neglecting certain terms, calculations show that in the lubrication model the radial derivative $\frac{\mu}{r} \frac{\partial}{\partial r} (r \frac{\partial u}{\partial r})$, that is neglected in Equation (2.3), tends to be significant compared to the axial derivative $\mu \frac{\partial^2 u}{\partial z^2}$ term close to the contact line. This is shown Figure 6.6a, where the height-averaged ratio between these two derivatives is given in the two last grid points as a function of the initial contact angle. The ratio in the last grid point is here estimated by calculating the ratio in the second last grid point with double the number of grid cells. There is no straightforward way to calculate this directly, because the numerical second derivative in the last point cannot be calculated without introducing additional boundary conditions. Similar ratios can be found between $\frac{\partial p}{\partial r}$ and $\frac{\partial p}{\partial z}$ when calculated numerically, as seen in Figure 6.6b. Note that in all these cases the height-averaged values are considered. Locally, the ratios can have even higher values.

If one wishes to understand particle dynamics in the context of Marangoni circulation to suppress the coffee-stain effect, it should be known that there are likely more effective methods of doing this suppression. In experiments performed by Marin et al. the authors did not find any correlation between the presence of Marangoni circulation and the reduction of the coffee-stain effect [115]. The reason for this is that particles are always transported towards the contact line at the end of the evaporation process, due to the capillary flow overcoming the Marangoni flow (the so-called ‘rush-hour effect’ [114]). This could also be an explanation why it is observed that even for lower contact angles, where according to Figure 6.6 the error should be of an order of 10%, there is still no circulation close to the contact line.

Although there are several methods to reduce the coffee-stain effect [124, 125, 132, 194], probably the most efficient way is by mobilizing the contact line so that it retracts during evaporation. This way, particles do not accumulate as a single ring on the substrate (e.g. see [165]).

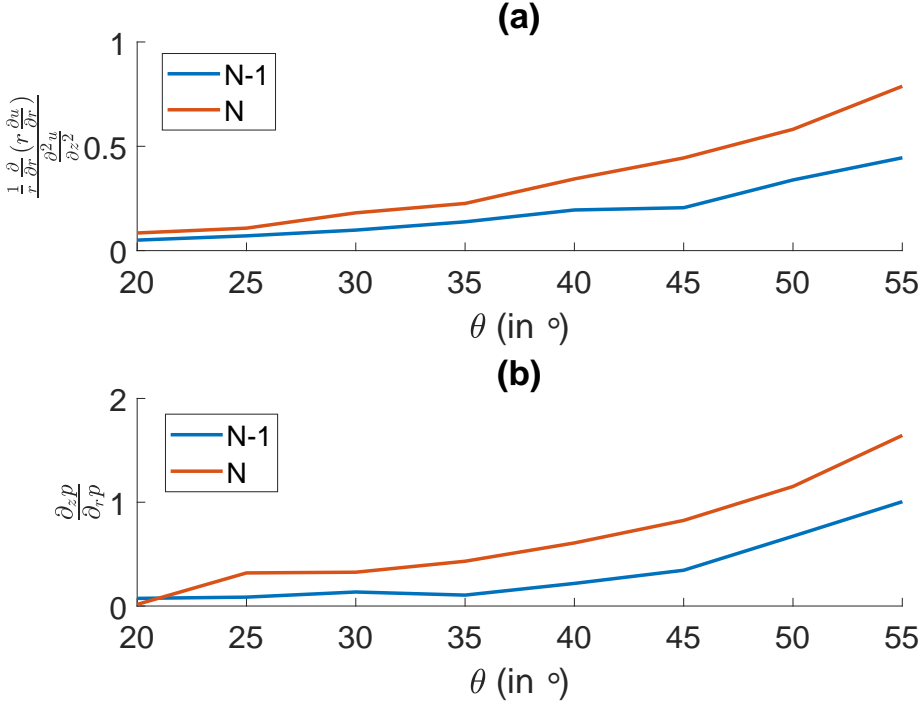


Figure 6.6.: Ratio between height-averaged derivatives as a function of initial contact angle in the last two grid points. (a) shows the ratio between the two viscous terms in the equation for $\frac{\partial^3 p}{\partial r^3}$ and (b) the ratio between $\frac{\partial p}{\partial z}$ and $\frac{\partial p}{\partial r}$. The red lines are in the last grid point in radial direction, the blue lines in the one but last grid point.

6.3.2. Two-phase particle model

In this subsection, the two-phase particle model is considered and methods are explored to implement it for concentrations up to and including the maximum packing fraction $y_{s,max}$. This is only done for pure droplet cases, because this makes the analysis simpler and clearer and because it was previously shown that the lubrication model does not describe Marangoni circulation in the contact line region well.

A simulation for a pure droplet with an initial (homogeneous) particle mass fraction of $y_{s,0} = 0.01$ shows that it reaches its maximum packing fraction $y_{s,max}$ (corresponding to a volumetric fraction of 0.64) quite soon after the start of the simulation (typically before 5% of the evaporation time). This maximum packing predictably occurs close to the contact line, where particles accumulate. Since water can still evaporate at that point, meaning that y_l can decrease, while the particle fraction y_s cannot increase any further (given that air is not considered as a phase), a contradiction occurs. This implies that in order to model particle-laden droplet evaporation, even at initially low colloidal concentrations, one needs to include a void fraction as well.

In literature, this has previously been tackled by modeling a transition from the Stokes regime to the Darcy regime as $y_s \rightarrow y_{s,max}$. While this method gives reasonable results [83, 84] it has two major issues in the context of lubrication theory. First, it requires the assumption of an arbitrary linear relationship between the fluid velocity and the particle velocity. Second, and more importantly, it can only be applied for a z-averaged particle concentration, which is undesirable if one wants to model particle circulation (e.g. in the context of Marangoni circulation [59]).

A realistic particle model at high concentrations should – in the view of the author – at least take into account the following:

1. The particle concentration cannot exceed the maximum packing density (assuming air is not considered as a phase);
2. At maximum packing, particles remain on the substrate (or on a solid mass of particles) if fluid evaporates;
3. At maximum packing, the particle flow stagnates if it is blocked by other particles, while fluid can still move through;
4. However, at maximum packing, particles should still be able to flow as a cluster that is transported by fluid. This also depends on the degree in which particles adhere to the substrate.

Unfortunately, no such model currently exists in the framework of lubrication theory. Therefore, the author suggests to either develop such a model or to only consider particle dynamics below the maximum packing density, which unfortunately has a very limited scope of application. Alternatively, corrections can be set that modify the particle concentration if appropriate conditions are met.

As an example of such a correction, if fluid evaporates from a region that is at maximum packing, one could displace a proportional amount of solid phase to the region below if that region is not at maximum packing yet. Then, if the entire region below is also at maximum packing, one could consider an amount of solid phase, proportional to the evaporated fluid, as removed from the system and leave it as a solid layer on top of the droplet.

Alternatively, if the fractions are expressed as mass fractions, one could allow for the solid mass fraction to go to 1 at the interface, because the rest of the region can be assumed to be filled with air, which has a negligible mass. The volume fraction still has a maximum smaller than 1 in that case, but the mass fraction has not. This will not work in the bulk of the droplet, however, because there will be no air there and thus the volume only consists of liquid and solid.

Regarding the flow behavior in the bulk, one could allow for a net flux of particles through a maximally packed region, while blocking particles upstream if they would cause the local solid fraction to exceed the maximum packing fraction.

Although these possible corrections are rather ad-hoc and do not fully take into account the underlying physics, such as porous flow behavior, they yield qualitatively reasonable results as illustrated in Figure 6.7. Here, the first and the third of the previously suggested corrections are used.

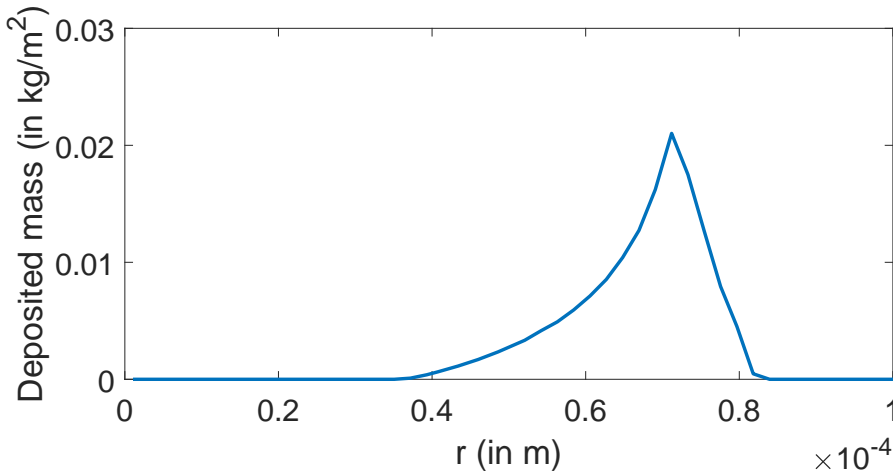


Figure 6.7.: Typical deposited solid mass after evaporation in the two-phase model.

Very similar to the results of the tracer particle model, as seen in Figure 6.2, there is a clear peak close to the contact line. A major difference however, is that the peak for the two-phase model is much wider than the peak for the tracer particle model. This is expected, because for the two-phase model not all particles can accumulate in the last few cells, but they are blocked by other particles as a ‘porous plug’ is formed [83, 84]. For the tracer particle model, on the other hand, all particles can freely flow to the contact line. Both models will increasingly converge as the initial particle concentration of the two-phase model is decreased.

Another difference between the two models is that the peak in Figure 6.7 is not centered at the contact line, like for the tracer model in Figure 6.2, but slightly shifted towards the center. The reason for this is that as particles approach the contact line the vertical available space decreases as the drop height $h(r, t)$ becomes smaller. Therefore, the deposition pattern cannot peak at $r = R$, but will do that closer to the center. This mechanism is not taken into account in the tracer model and thus the peak is at $r = R$ in that case.

Thus, to conclude, a start has been made in developing a two-phase particle model in the context of lubrication theory, and already some qualitatively reasonable results are obtained. However, before it can be used, it needs to be improved by better considering the underlying physics and making the implementation less ad-hoc than it currently is.

The most viable solution lies in developing a model that takes into account the transition from the Stokes regime at low particle concentrations to the Darcy regime at higher concentrations. As mentioned before, this was partly done by Kaplan et al. [83, 84], but with severe limitations, most prominent the requirement of a height averaged particle concentration. If the axial component is also taken into account, as for example was done for binary droplets by Diddens et al. [39], only then particle dynamics can be modeled at higher concentrations in a sufficiently physical way. This involves several challenges, because it requires a more complex derivation of the

height evolution equation and velocity field in the lubrication limit and because it needs a model for evaporation through a porous layer.

6.4. Conclusion

In this chapter a numerical model was proposed to describe particle dynamics in an evaporating, surfactant-laden droplet. The droplet dynamics were modeled using lubrication theory and the surfactant transport using several convection-diffusion-adsorption equations. Two different particle models were considered: a ‘tracer particle model’, where the solute is considered as passive, massless and without volume, and the ‘two-phase model’, where the particles make up a distinct phase beside the fluid phase and have a maximum packing fraction that is taken into account.

The tracer particle model was tested first for two different cases: a pure droplet and a droplet with surfactants. In case of the pure droplet a capillary flow towards the contact line arises due to preferential evaporation, while in case of the surfactant-laden droplet there is, besides the capillary flow towards the contact line, also a Marangoni flow towards the apex of the droplet. Therefore, it was expected that the pure droplet would result in a coffee-stain like deposition pattern, while for the surfactant-laden droplet a more homogeneous deposition pattern was expected.

The tracer particle model, however, resulted for both cases in a coffee-stain-like peak at the contact line. This is caused by the velocity field not circulating in the contact line region for the surfactant case. Therefore, particles accumulate at the contact line, similar to the pure droplet case.

Several methods were proposed to solve this problem, of which adding a correction term to the interfacial shear stress was the most important one. Unfortunately, none of these methods improved the accuracy of the velocity in any way in the contact line region.

Therefore, it was concluded that the lubrication model in its current form is not suitable to describe circulation in the contact line region. It is likely that models that consider droplet dynamics in a 2D or 3D way (rather than a 1D height profile $h(r, t)$) can perform better in the contact line region, because these methods can probably approximate the pressure field more accurately there by neglecting fewer terms. Also, these methods allow for a mesh that conforms to the drop shape and flow field.

Regarding the two-phase model, it was shown that any model that takes into account the space that particles occupy in an evaporating sessile droplet, should also consider the maximum packing fraction, since this maximum fraction is often already locally reached in the initial stages of the drying process. However, this raises several issues regarding how the particles and the fluid flow behave when the maximum fraction is reached and what happens when fluid evaporates from a maximally packed region.

An initial step was made to deal with these issues by implementing several corrections to the particle fraction $y_s(r, z, t)$ that are triggered if the maximum packing fraction is reached. Although ad-hoc and not fully considering the underlying physics, this method did yield qualitatively reasonable results. However, before the model can be

used in practice, it should be improved in such a way that these corrections follow naturally from the considered physics. This can be done by treating the transition from lower to higher particle concentrations as the transition from a Stokes regime flow to a Darcy regime flow [83, 84].

7. Conclusions

The goal of this thesis was to give insight into the effects of surfactants on the dynamics of inkjet printed droplet in the presence of evaporation and absorption.

In Chapter 2 the relevant differential equations were introduced that describe the physical model. The droplet dynamics are given by lubrication theory, which regards the contact radius as having a significantly larger magnitude than the drop height, allowing one to describe the evolution in terms of a height profile $h(r, t)$. The surfactant dynamics are modeled with several convection-diffusion-adsorption equations, both in the bulk of the fluid and on the interfaces. Furthermore, the evaporation field is solved analytically using the assumption of a spherical cap shape and the absorption into the porous medium using Darcy's law.

In Chapter 3 two models – a slip model and a precursor film model – were compared for the contact line motion of the drop during evaporation. For pure droplets these models performed comparably, but in the presence of insoluble surfactants several problems were encountered with the precursor film model. Because the precursor film model does not inherently distinguish between the droplet and the precursor film, all surfactant can freely flow between these two, yielding unphysical results. The slip model, on the other hand, showed that even if there is no real pinning force present, surfactants can still keep the contact line nearly pinned. This is caused by the fact that as the available interface shrinks due to evaporation, the surfactant concentration increases, which results in a decreasing surface tension and thus a decreasing equilibrium contact angle.

In Chapter 4 the flow field inside evaporating droplets in the presence of surfactants was investigated. It was shown that there are typically two flow regimes in drying surfactant-laden droplets: a circulatory regime, where there is the combination of a capillary flow towards the contact line and an interfacial Marangoni flow towards the drop apex, and a coffee-ring regime, where there is only a capillary flow towards the contact line, while the interfacial flow nearly halts due to the Marangoni effect. Which of these two regimes will be dominant can be predicted based on the surfactant, the fluid and the environmental conditions. Factors that were found to typically promote the circulatory regime over the coffee-ring regime are relatively high surfactant solubility, fast adsorption kinetics and slow diffusion. These results were found to be consistent with literature data [82, 115]. Also, for surfactant concentrations beyond the critical micelle concentration (CMC) simulations were carried out, but these data points are not in agreement with experimental literature [115, 157]. The differences are probably a result of underlying micelle kinetics that were not taken into account in the model.

In Chapter 5 the absorption dynamics of surfactant-laden droplets were examined. First, it was shown that for pure droplets the penetration depth, being the deepest point of the wetting front, evolves in time according to a square root relation. However, for a pinned contact line the droplet absorbs much faster than for a moving contact line, because of the differences in contact area over time. Also, the final shape of the wetted region is more pointed for a moving contact line case than for a pinned

contact line case. When surfactants are involved, the absorption rate tends to accelerate under certain conditions. If the adsorption kinetics of the surfactant are not too fast compared to the absorption dynamics, surfactant will reach the wetting front and adsorb there onto the pore walls, increasing the magnitude of the suction pressure. If the adsorption kinetics of the surfactant are too fast, however, all surfactant will already adsorb onto the pore walls before reaching the wetting front. In that case the absorption rate will be the same as for a pure case. These results are in accordance with literature [169].

In Chapter 6 the dynamics of particles were investigated in the presence of surfactants. Two different particle models were introduced: a tracer particle model, which considers the particles as massless and passive, and a two-phase model, which considers particles as a distinct solid phase. First, the tracer model was tested for a pure droplet case, where there is only a capillary flow towards the contact line, and for a surfactant case, where there is also an interfacial Marangoni flow towards the drop apex. It was expected that for the pure case a ring-like deposition pattern would form and for the surfactant case a more homogeneous pattern. However, both yielded a ring-like residue. A likely reason for this is that the assumptions of lubrication theory no longer hold in the contact line region, resulting in an inaccurate velocity field. After the tracer particle model was tested in this way, the two-phase model was considered. It was shown that quite soon in the drying process the maximum packing fraction of the particles is reached, which requires several amendments to this model. It was shown that by making certain ad-hoc corrections reasonable results can be found. However, a better physicality of the model is required.

Recommendations

There are several options available to extend the research presented in this thesis. The options that are expected to lead to the most significant improvements are the following:

- Develop a mechanism that keeps surfactants from flowing freely out of the droplet into a precursor film. This allows one to also use the precursor film model in combination with surfactants, especially in the case of evaporation-driven dynamics and partial wetting. Some methods already exist for this, but these tend to have low stability (see e.g. [180]).
- Create a micelle kinetics and transport model that incorporates the full richness of micelle dynamics. This way, experimental results from literature (see e.g. [115, 157]) can be explained and reliable predictions can be made. Possible additions to the model presented in this thesis are multi-step micelle formation and micelle formation/adsorption at the interfaces.
- Develop a 2D interface tracking method for the evolution of the wetted region in the porous medium. This has the potential to make the method more stable where the wetting front touches the surface of the substrate, allowing for a spatially variable suction pressure. In the current method a variable suction results in instabilities that are too severe to solve. Furthermore, an extension

to the Darcy model (e.g. the Brinkman extension [17]) could also improve the method.

- Increase the accuracy of the velocity field in the contact line region. This is required for the modeling of particle transport if there is a circulatory flow. It may be possible to improve the velocity field by adding correction terms that are neglected in standard lubrication theory.
- Create a lubrication model that includes the transition from the Stokes regime to the Darcy regime at high particle fractions (e.g. see [83, 84]). This is necessary for any two-phase particle model, since in many cases the maximum packing fraction is already reached locally in the initial stages of the drying process.
- Further topics of interest that can be considered using the models from this thesis include: the presence of multiple surfactant types in a single droplet, temperature effects and nonaxisymmetric behavior (such as fingering instabilities).

A. Input parameters

In this appendix the input parameters are given for several simulations that were carried out.

A.1. Input values in Chapter 4

All relevant parameters that were used for the results of Chapter 4 and their typical values are given by Table A.1. In order to vary the dimensionless numbers (see Table 4.1), any of these parameters can be changed if required. It is ensured that the same results are found if the same dimensionless numbers are obtained by varying different parameters.

Name	Symbol	Value
Critical micelle concentration	CMC	1.0 mol/m^3
Micelle diffusivity	D_M	$7.2 \cdot 10^{-12} \text{ m}^2/\text{s}$
Vapor diffusivity	D_v	$2.7 \cdot 10^{-5} \text{ m}^2/\text{s}$
Interfacial diffusivity	D_Γ	$4.3 \cdot 10^{-10} \text{ m}^2/\text{s}$
Bulk diffusivity	D_ϕ	$2.9 \cdot 10^{-10} \text{ m}^2/\text{s}$
Typical initial drop height	H	0.36 mm
Micelle aggregation factor factor	k_a^M	$1.0 \cdot 10^{-2} \text{ m}^{3N-2}/\text{s}/\text{mol}^{N-1}$
Interfacial adsorption factor	k_a^Γ	$5.0 \cdot 10^{-7} \text{ m/s}$
Micelle decomposition factor	k_d^M	1.0 s^{-1}
Interfacial desorption factor	k_d^Γ	$9.5 \cdot 10^{-1} \text{ s}^{-1}$
Liquid molar mass	M_l	0.018 kg/mol
Initial micelle concentration	M_0	$1.0 \cdot 10^{-2} \text{ mol/m}^3$
Preferred micelle size	N	12
Liquid saturation pressure	$p_{sat,l}$	3158 Pa
Typical initial drop radius	R	1.6 mm
Relative humidity	RH	0.55
Universal gas constant	R_u	8.314 J/K/mol
Temperature	T	298 K
Initial interfacial surfactant concentration	Γ_0	$5.0 \cdot 10^{-7}$
Maximal interfacial surfactant concentration	Γ_∞	$1.0 \cdot 10^{-5}$
Initial contact angle	θ_0	25°
Dynamic viscosity	μ	$0.89 \text{ mPa}\cdot\text{s}$
Liquid mass density	ρ	997 kg/m^3
Pure surface tension	σ_0	0.072 N/m
Initial bulk surfactant concentration	ϕ_0	1.0 mol/m^3

Table A.1.: Relevant parameters in Chapter 4.

A.2. Input values in Chapter 5

The simulations that were performed for Figures 5.1, 5.2 and 5.3 had the following input parameters:

Parameter	Symbol	Value	Unit
Advancing contact angle	θ_{adv}	70	deg
Contact line sensitivity	k	0.12	$\text{m}\cdot\text{s}^{-1}$
Drop volume	V	1.51 for the constant V_0 cases, 0.83 for the constant R_0 case	μL
Dynamic viscosity	μ	0.89	$\text{mPa}\cdot\text{s}$
Initial contact angle	θ_0	20 - 35	deg
Liquid-gas surface tension	γ_{lg}	72	$\text{mN}\cdot\text{m}^{-1}$
Mass density	ρ	997	$\text{kg}\cdot\text{m}^{-3}$
Pore diameter	d	0.22	μm
Porosity	η	0.67	-
Radius	R	14.3 for the constant R_0 cases, 17.5 for the constant V_0 case	mm
Receding contact angle	θ_{rec}	20 - 35	deg
Slip length	β	0 for the pinned case, 100 for the unpinned cases	nm

Table A.2.: Input values for Figures 5.1, 5.2 and 5.3.

The simulations that were performed for the experimental comparison in Figure 5.4a had the following input parameters: These input parameters and the experimental

Parameter	Symbol	Value	Unit
Advancing contact angle	θ_{adv}	80	deg
Contact line sensitivity	k	6.61	$\text{m}\cdot\text{s}^{-1}$
Drop volume	V	10.4	μL
Dynamic viscosity	μ	0.955	$\text{mPa}\cdot\text{s}$
Height	H	0.849	mm
Initial contact angle	θ_0	35	deg
Liquid-gas surface tension	γ_{lg}	73	$\text{mN}\cdot\text{m}^{-1}$
Mass density	ρ	1000	$\text{kg}\cdot\text{m}^{-3}$
Permeability	κ_p	3.46×10^{-11}	m^2
Pore diameter	d	90	μm
Porosity	η	0.351	-
Radius	R	2.69	mm
Receding contact angle	θ_{rec}	35	deg
Slip length	β	100	nm

Table A.3.: Input values for Figure 5.4a.

results were obtained from the Center of Smart Interfaces at Darmstadt University of Technology [130], with the exception of the initial and receding contact angle,

the slip length and the contact angle sensitivity, which were estimated based on the experimental results.

The simulations that were performed for the experimental comparison in Figure 5.4b had the following input parameters: These input parameters and the experimental

Parameter	Symbol	Value	Unit
Advancing contact angle	θ_{adv}	70	deg
Drop volume	V	1.51	mL
Dynamic viscosity	μ	0.89	mPa·s
Height	H	4.52	mm
Initial contact angle	θ_0	35	deg
Liquid-gas surface tension	γ_{lg}	72	mN·m ⁻¹
Mass density	ρ	997	kg·m ⁻³
Pore diameter	d	0.22	μm
Porosity	η	0.67	-
Radius	R	14.3	mm
Receding contact angle	θ_{rec}	35	deg

Table A.4.: Input values for Figure 5.4b.

results were given by Starov et al. (2004) [169]. Not all parameters were given in that article, so some have been estimated (like θ_e and η by a typical contact angle and porosity of nitrocellulose [1, 56, 94, 196]). Furthermore, Starov et al. use a liquid container rather than a droplet. Therefore, arbitrary droplet dimensions were chosen since it was shown in Section 3.1 that the evolution of H_p is not influenced by the shape of the fluid reservoir.

Lastly, the simulations that were performed for the results in Figure 5.7 had the input parameters that are given in Table A.5. Several of these parameters have been estimated, given that no literature data exists, and primarily serve to illustrate that the principle that was experimentally discovered by Starov et al. can also be analyzed numerically.

Note that the initial contact angle θ_0 has for surfactant cases the same value as for pure cases ($\theta_0 = 35^\circ$). This is consistent, because for the surfactant cases only pinned contact lines are considered (since the evolution of H_p is independent of the droplet shape). The surfactants therefore have no direct influence on the (equilibrium) contact angle, since the latter does not follow Young's equation: $\gamma_{sg} - \gamma_{sl} - \gamma_{lg} \cos \theta_e = 0$.

Parameter	Symbol	Value	Unit
Advancing contact angle	θ_{adv}	70	deg
Bulk diffusivity	D_C	2.88×10^{-10}	$\text{m}^2 \cdot \text{s}^{-1}$
Drop volume	V	1.51	mL
Dynamic viscosity	μ	0.89	$\text{mPa} \cdot \text{s}$
Height	H	4.52	mm
Initial bulk surfactant concentration	C_0	0 - 50	mM
Initial contact angle	θ_0	35	deg
Initial interfacial surfactant concentration	Γ_0	5.0×10^{-7}	$\text{mol} \cdot \text{m}^{-2}$
Mass density	ρ	997	$\text{kg} \cdot \text{m}^{-3}$
Maximum interfacial surfactant concentration (liquid-air)	Γ_∞	1.0×10^{-5}	$\text{mol} \cdot \text{m}^{-2}$
Maximum interfacial surfactant concentration (solid-liquid)	$c_\infty = \frac{4}{d} S_\infty$	5.0×10^{-6}	$\text{mol} \cdot \text{m}^{-2}$
Minimum solid-liquid surface tension	$\gamma_{sl,\infty}$	3.6	$\text{mN} \cdot \text{m}^{-1}$
Pore diameter	d	0.22 - 3.0	μm
Porosity	η	0.67	-
Pure liquid-gas surface tension	γ_{lg}	72	$\text{mN} \cdot \text{m}^{-1}$
Pure solid-liquid surface tension	γ_{sl}	36	$\text{mN} \cdot \text{m}^{-1}$
Radius	R	14.3	mm
Receding contact angle	θ_{rec}	35	deg
Surface adsorption factor (liquid-air)	k_a^Γ	1.0×10^{-9}	$\text{m} \cdot \text{s}^{-1}$
Surface adsorption factor (liquid-solid)	k_a^S	1.0×10^{-6}	$\text{m} \cdot \text{s}^{-1}$
Surface desorption factor (liquid-air)	k_d^Γ	9.5×10^{-2}	s^{-1}
Surface desorption factor (liquid-solid)	k_d^S	1.0×10^{-4}	s^{-1}
Surface diffusivity	D_Γ	4.33×10^{-9}	$\text{m}^2 \cdot \text{s}^{-1}$

Table A.5.: Input values for Figure 5.7.

Bibliography

- [1] A.L. Ahmad, S.C. Lova, S.R. Abd Shukora, A. Ismailb, and A.R. Sunartia. Development of lateral flow membranes for immunoassay separation. *Desalin. Water Treat.*, 5:99–105, 2009.
- [2] G. Ahmed and M. Sellier. Modeling the effects of absorption on spreading dynamics. *Transp. Porous Med.*, 112:637–663, 2016.
- [3] G. Ahmed, O. Arjmandi Tash, J. Cook, A. Trybala, and V. Starov. Biological applications of kinetics of wetting and spreading. *Adv. Colloid Interface Sci.*, 249:17–36, 2017.
- [4] N. Alleborn and H. Raszillier. Spreading and sorption of a droplet on a porous substrate. *Chem. Eng. Sci.*, 59:2071–2088, 2004.
- [5] N. Alleborn and H. Raszillier. spreading and sorption of droplets on layered porous substrates. *J. Colloid Interface Sci.*, 280:449–464, 2004.
- [6] P. Atkins and J. de Paula. *Atkins' Physical Chemistry*. Oxford University Press, Oxford, 2010.
- [7] M.R. Barmi and C.D. Meinhardt. Convective flows in evaporating sessile droplets. *J. Phys. Chem. B*, 118:2414–2421, 2014.
- [8] H.A. Barnes. The yield stress - a review or 'παντα ρει' - everything flows? *J. Non-Newtonian Fluid Mech.*, 81:133–178, 1999.
- [9] G.K. Batchelor. *An Introduction to Fluid Dynamics*. Cambridge University Press, 2000.
- [10] I. Bazhlekov and D. Vasileva. Numerical modeling of drop coalescence in the presence of soluble surfactants. *J. Comput. appl. Math.*, 293:7–19, 2016.
- [11] D.R. Beacham, O.K. Matar, and R.V. Craster. Surfactant-enhanced rapid spreading of drops on solid surfaces. *Langmuir*, 25:14174–14181, 2009.
- [12] S.W. Benintendi and M. K. Smith. The spreading of a non-isothermal liquid droplet. *Phys. Fluids*, 11:982, 1999.
- [13] E. Bormashenko and M. Zinigrad A. Musin. Evaporation of droplets on strongly and weakly pinning surfaces and dynamics of the triple line. *Colloids Surf. A*, 385:235–240, 2011.
- [14] E. Bormashenko. Surface instabilities and patterning at liquid/vapor interfaces: Exemplifications of the "hairy ball theorem". *Colloids and Interface Sci. Commun.*, 5:5–7, 2015.
- [15] N. Bowden, F. Arias, T. Deng, and G.M. Whitesides. Self-assembly of microscale objects at a liquid/liquid interface through lateral capillary forces. *Langmuir*, 17:1757–1765, 2001.

-
- [16] N. Brielles, F. Chantraine, M. Viana, D. Chulia, P. Branlard, G. Rubinstenn, F. Lequeux, and O. Mondain-Monvala. Dissolution of a surfactant-containing active porous material. *J. Colloid Interface Sci.*, 328:344–352, 2008.
- [17] H.C. Brinkman. A calculation of the viscous force exerted by a flowing fluid on a dense swarm of particles. *Appl. Sci. Res. A*, 1:27–34, 1947.
- [18] C.E. Brown, N.J. Jones, and E.L. Neustadter. Interfacial flow during immiscible displacement. *J. Colloid Interface Sci.*, 76:582, 1980.
- [19] A.B.D. Brown, C.G. Smith, and A.R. Rennie. Fabricating colloidal particles with photolithography and their interactions at an air-water interface. *Phys. Rev. E*, 62:951, 2000.
- [20] P.C. Carman. *Flow of gases through porous media*. Butterworths, London, 1956.
- [21] K.Y. Chan and A. Borhan. Surfactant-assisted spreading of a liquid drop on a smooth solid surface. *J. Colloid Interface Sci.*, 287:233–248, 2005.
- [22] C. Chang and E.I. Franses. Adsorption dynamics of surfactants at the air/water interface: a critical review of mathematical models, data, and mechanisms. *Colloids Surfaces A Physicochem Eng Asp*, 100:1–45, 1995.
- [23] G. Chaniel, M. Frenkel, V. Multanen, and E. Bormashenko. Paradoxical coffee-stain effect driven by the marangoni flow observed on oil-infused surfaces. *Colloids Surf, A*, 522:355–360, 2017.
- [24] Y. Chen, B. Jiang, L. Liu, Y. Du, T. Zhang, L. Zhao, and Y. Huang. High ink absorption performance of inkjet printing based on sio₂@al₁₃ core-shell composites. *Appl. Surf. Sci.*, 436:995–1002, 2018.
- [25] R.P. Chilcott, J. Jenner, W. Carrick, S.A.M. Hotchkiss, and P. Rice. Human skin absorption of bis-2-(chloroethyl)sulphide (sulphur mustard) in vitro. *J. Appl. Toxicol.*, 20:349–355, 2000.
- [26] D.K. Chou, R. Krishnamurthy, T.W. Randolph, J.F. Carpenter, and M.C. Manning. Effects of tween 20 and tween 80 on the stability of albutropin during agitation. *J. Pharm. Sci.*, 94:1368–1381, 2005.
- [27] N.V. Churaev, G.A. Martynov, V.M. Starov, and Z.M. Zorin. Some features of capillary imbibition of surfactant solutions. *Colloid Polym. Sci.*, 259:747, 1981.
- [28] M.A. Clay and M.J. Miksis. Effects of surfactant on droplet spreading. *Phys. Fluids*, 16:3070, 2004.
- [29] P. Colinet and A. Rednikov. On integrable singularities and apparent contact angles within a classical paradigm: partial and complete wetting regimes with or without phase change. *Eur. Phys. J. Spec. Top.*, 197:89–113, 2011.
- [30] A. Crivoi and F. Duan. Amplifying and attenuating the coffee-ring effect in drying sessile nanofluid droplets. *Phys. Rev. E*, 87:042303, 2013.
- [31] A. Crivoi and F. Duan. Effect of surfactant on the drying patterns of graphite nanofluid droplets. *J. Phys. Chem. B*, 117:5932–5938, 2013.
-

-
- [32] D.B. van Dam and J.G.M. Kuerten. Modeling the drying of ink-jet-printed structures and experimental verification. *Langmuir*, 24:582–589, 2008.
- [33] S.H. Davis and L.M. Hocking. Spreading and imbibition of viscous liquid on a porous base. *Phys. Fluids*, 11:48, 1999.
- [34] S.H. Davis and L.M. Hocking. Spreading and imbibition of viscous liquid on a porous base. ii. *Phys. Fluids*, 12:1646, 2000.
- [35] R.D. Deegan, O. Bakajin, T.F. Dupont, G. Huber, S.R. Nagel, and T.A. Witten. Capillary flow as the cause of ring stains from dried liquid drops. *Nature*, 389:827–829, 1997.
- [36] R.D. Deegan. Pattern formation in drying drops. *Phys. Rev. E*, 61:475–485, 2000.
- [37] R.D. Deegan, O. Bakajin, T.F. Dupont, G. Huber, S.R. Nagel, and T.A. Witten. Contact line deposits in an evaporating drop. *Phys. Rev. E*, 62:756–765, 2000.
- [38] B.V. Derjaguin, N.V. Churaev, and V.M. Muller. *Surface Forces*. Plenum Press, New York, 1987.
- [39] C. Diddens, J.G.M. Kuerten, C.W.M. van der Geld, and H.M.A. Wijshoff. Modeling the evaporation of sessile multi-component droplets. *J. Colloid Interface Sci.*, 487:426–436, 2017.
- [40] C. Diddens, H. Tan, P. Lv, M. Versluis, J.G.M. Kuerten, X. Zhang, and D. Lohse. Evaporating pure, binary and ternary droplets: thermal effects and axial symmetry, breaking. *J. Fluid Mech.*, 823:470–497, 2017.
- [41] C. Diddens. Detailed finite element method modeling of evaporating multi-component droplets. *J. Comput. Phys.*, 340:670–687, 2017.
- [42] R. de Dier, W. Sempels, J. Hofkens, and J. Vermant. Thermocapillary fingering in surfactant-laden water droplets. *Langmuir*, 30:13338–13344, 2014.
- [43] J.A. Diez, L. Kondic, and A. Bertozzi. Global models for moving contact lines. *Phys. Rev. E*, 63:011208, 2000.
- [44] J.F. Dijksman and A. Pierik. Fluid dynamical analysis of the distribution of ink jet printed biomolecules in microarray substrates for genotyping applications. *Biomicrofluidics*, 2(4):044101, 2008.
- [45] M.D. Doganci, B.U. Sesli, and H.Y. Erbil. Diffusion-controlled evaporation of sodium dodecyl sulfate solution drops placed on a hydrophobic substrate. *J. Colloid Interface Sci.*, 362:524–531, 2011.
- [46] V. Dugas, J. Broutin, and E. Souteyrand. Droplet evaporation study applied to dna chip manufacturing. *Langmuir*, 21:9130–9136, 2005.
- [47] A.D. Dussaud, O.K. Matar, and S.M. Troian. Spreading characteristics of an insoluble surfactant film on a thin liquid layer: comparison between theory and experiment. *J. Fluid Mech.*, 544:23–51, 2005.
- [48] B.D. Edmonstone, R.V. Craster, and O.K. Matar. Surfactant-induced fingering
-

-
- phenomena beyond the critical micelle concentration. *J. Fluid Mech.*, 564:105–138, 2006.
- [49] A.M.J. Edwards, P.S. Atkinson, C.S. Cheung, H. Liang, D.J. Fairhurst, and F.F. Ouali. Density-driven flows in evaporating binary liquid droplets. *Phys. Rev. Lett.*, 121:184501, 2018.
- [50] J. Eggers and L.M. Pismen. Nonlocal description of evaporating drops. *Phys. Fluids*, 22(11):112101, 2010.
- [51] P. Ehrhard and S.H. Davis. Non-isothermal spreading of liquid drops on horizontal plates. *J. Fluid Mech.*, 229:365–388, 1991.
- [52] A. Einstein. Über die von der molekularkinetischen theorie der wärme geforderte bewegung von in ruhenden flüssigkeiten suspendierten teilchen. *Annalen der Physik*, 322:549–560, 1905.
- [53] H.Y. Erbil. Control of stain geometry by drop evaporation of surfactant containing dispersions. *Adv. Colloid Interface Sci.*, 222:275–290, 2015.
- [54] D.P. Faasen, A. Jarray, H.J.W. Zandvliet, E.S. Kooij, and W. Kwiecinski. Hansen solubility parameters obtained via molecular dynamics simulations as a route to predict siloxane surfactant adsorption. *J. Colloid Interface Sci.*, 575:326–336, 2020.
- [55] B.J. Fischer. Particle convection in an evaporating colloidal droplet. *Langmuir*, 18:60–67, 2002.
- [56] G.E. Fridley, C.A. Holstein, S.B. Oza, and P. Yager. The evolution of nitrocellulose as a material for bioassays. *MRS Bull.*, 38:326–330, 2013.
- [57] F. Fu, P. Li, K. Wang, and R. Wu. Numerical simulation of sessile droplet spreading and penetration on porous substrates. *Langmuir*, 35:2917–2924, 2019.
- [58] R.T. van Gaalen, C. Diddens, H.M.A. Wijshoff, and J.G.M. Kuerten. The evaporation of surfactant-laden droplets: a comparison between contact line models. *J. Colloid Interface Sci.*, 579:888–897, 2020.
- [59] R.T. van Gaalen, C. Diddens, H.M.A. Wijshoff, and J.G.M. Kuerten. Marangoni circulation in evaporating droplets in the presence of soluble surfactants. *J. Colloid Interface Sci.*, 584:622–633, 2021.
- [60] R.T. van Gaalen, C. Diddens, D.P. Siregar, H.M.A. Wijshoff, and J.G.M. Kuerten. Absorption of surfactant-laden droplets into porous media: a numerical study. *J. Colloid Interface Sci.*, 597:149–159, 2021.
- [61] P.G. de Gennes, F. Brochard-Wyart, and D. Quere. *Capillarity and Wetting Phenomena*. Springer, New York, 2004.
- [62] F. Girard, M. Antoni, and K. Sefiane. On the effect of marangoni flow on evaporation rates of heated water drops. *Langmuir*, 24:9207–9210, 2008.
- [63] C. Giroto, B.P. Rand, J. Genoe, and P. Heremans. Exploring spray coating as a deposition technique for the fabrication of solution-processed solar cells. *Sol.*
-

Energy Mater. Sol. Cells, 93:454–458, 2009.

- [64] C.R. Glass, K.F.A. Walters, P.H. Gaskell, Y.C. Lee, H.M. Thompson, D.R. Emerson, and X. Gu. Recent advances in computational fluid dynamics relevant to the modelling of pesticide flow on leaf surfaces. *Pest Manag. Sci.*, 66:2–9, 2010.
- [65] R. Goodwin and G.M. Homsy. Viscous-flow down a slope in the vicinity of a contact line. *Phys. Fluids A*, 3:515, 1991.
- [66] P.J. Haley and M.J. Miksis. The effect of the contact line on droplet spreading. *J. Fluid Mech.*, 223:57–81, 1991.
- [67] W. Han and Z. Lin. Learning from “coffee rings”: Ordered structures enabled by controlled evaporative self-assembly. *J. Am. Chem. Soc.*, 130:6076, 2008.
- [68] W.B. Hardy. The spreading of fluids on glass. *Philos. Mag.*, 38:49–55, 1919.
- [69] G.S. Hartley and I.J. Graham-Bryce. *Physical principles of pesticide behaviour*. Academic Press, London/New York, 1980.
- [70] H. Hu and R.G. Larson. Evaporation of a sessile droplet on a substrate. *J. Phys. Chem. B*, 106:1334–1344, 2002.
- [71] H. Hu and R.G. Larson. Analysis of the microfluidic flow in an evaporating sessile droplet. *Langmuir*, 21:3963–3971, 2005.
- [72] H. Hu and R.G. Larson. Analysis of the effects of marangoni stresses on the microflow in an evaporating sessile droplet. *Langmuir*, 21:3972–3980, 2005.
- [73] H. Hu and R.G. Larson. Marangoni effect reverses coffee-ring depositions. *J. Phys. Chem. B*, 110:7090–7094, 2006.
- [74] C. Huh and L.E. Scriven. Hydrodynamic model of steady movement of a solid/liquid/fluid contact line. *J. Colloid Interface Sci.*, 35:85–101, 1971.
- [75] R.J. Hunter. *Foundations of Colloid Science*. Oxford University Press, Oxford, 1991.
- [76] Mordor Intelligence. Commercial printing market – growth, trends, covid-19 impact, and forecasts (2021 – 2026). <https://www.mordorintelligence.com/industry-reports/commercial-printing-market>, 2020.
- [77] J.N. Israelachvili. *Intermolecular and Surface Forces*. Elsevier inc., London, 2011.
- [78] O.E. Jensen and J.B. Grotberg. The spreading of heat or soluble surfactant along a thin film. *Phys. Fluids A*, 5:58–68, 1993.
- [79] O.E. Jensen and S. Naire. The spreading and stability of a surfactant-laden drop on a prewetted substrate. *J. Fluid Mech.*, 554:5–24, 2006.
- [80] P. Johnson, T. Routledge, A. Trybala, M. Vaccaro, and V. Starov. Wetting and spreading of commercially available aqueous surfactants on porous materials. *Colloids Interfaces*, 3:14, 2019.

-
- [81] P. Johnson, A. Trybala, M. Vaccaro, and V. Starov. Kinetics of spreading over porous substrates. *Colloids Interfaces*, 3:38, 2019.
- [82] N. Jung, H.W. Seo, P.H. Leo, J. Kim, P. Kim, and C.S. Yoo. Surfactant effects on droplet dynamics and deposition patterns: a lattice gas model. *Soft Matter*, 13:6529, 2017.
- [83] C.N. Kaplan and L. Mahadevan. Evaporation-driven ring and film deposition from colloidal droplets. *J. Fluid Mech.*, 781:R2, 2015.
- [84] C.N. Kaplan, N. Wu, S. Mandre, J. Aizenberg, and L. Mahadevan. Dynamics of evaporative colloidal patterning. *Phys. Fluids*, 27:092105, 2015.
- [85] G. Karapetsas, R.V. Craster, and O.K. Matar. On surfactant-enhanced spreading and superspreading of liquid drops on solid surfaces. *J. Fluid Mech.*, 670:5–37, 2011.
- [86] G. Karapetsas, K.C. Sahu, and O.K. Matar. Evaporation of sessile droplets laden with particles and insoluble surfactants. *Langmuir*, 32:6871–6881, 2016.
- [87] S. Karpitschka, F. Liebig, and H. Riegler. Marangoni contraction of evaporating sessile droplets of binary mixtures. *Langmuir*, 33:4682–4687, 2017.
- [88] S. Kezic and J.B. Nielsen. Absorption of chemicals through compromised skin. *Int. Arch. Occup. Environ. Health*, 82:677–688, 2009.
- [89] J. Kim. Spray cooling heat transfer: The state of the art. *Int. J. Heat Fluid Flow*, 28(4):753–767, 2007.
- [90] J. Kozeny. Über kapillare leitung des wassers im boden. *Sitzungsber Akad. Wiss.*, 136:271–306, 1927.
- [91] R. Krechetnikov. On application of lubrication approximations to nonuni-directional coating flows with clean and surfactant interfaces. *Phys. Fluids*, 22:092102, 2010.
- [92] I.M. Krieger and T.J. Dougherty. A mechanism for non-newtonian flow in suspensions of rigid spheres. *J. Rheol.*, 3:137–152, 1959.
- [93] R. Krishna and J.A. Wesselingh. The maxwell-stefan approach to mass transfer. *Chem. Eng. Sci.*, 52:861–911, 1997.
- [94] A. Ksiazczak, A. Radomski, and T. Zielenkiewicz. Nitrocellulose porosity - thermoporometry. *J. Therm. Anal. Cal.*, 74:559–568, 2003.
- [95] R. Kurrat, J.J. Ramsden, and J.E. Prenosil. Kinetic model for serum albumin adsorption : experimental verification. *J. Chem. Soc., Faraday Trans.*, 90:587–590, 1994.
- [96] R. Kurrat, J.E. Prenosil, and J.J. Ramsden. Kinetics of human and bovine serum albumin adsorption at silica–titania surfaces. *J. Colloid Interface Sci.*, 185:1–8, 1997.
- [97] W. Kwieciński, T. Segers, S. van der Werf, A. van Houselt, D. Lohse, H.J.W. Zandvliet, and S. Kooij. Evaporation of dilute sodium dodecyl sulfate droplets
-

on a hydrophobic substrate. *Langmuir*, 35:10453–10460, 2019.

- [98] T.A. Roose K.Y. Wertheim. Mathematical model of lymphangiogenesis in a zebrafish embryo. *Bull Math Biol*, 79:693–737, 2017.
- [99] L. Labajos-Broncano, J.A. Antequera-Barroso, M.L. González-Martín, and J.M. Bruque. An experimental study about the imbibition of aqueous solutions of low concentration of a non-adsorbable surfactant in a hydrophilic porous medium. *J. Colloid Interface Sci.*, 301:323–328, 2006.
- [100] L. Labajos-Broncano, J.A. Antequera-Barroso, M.L. González-Martín, and J.M. Bruque. Influence of the interfacial adsorptions on the imbibition of aqueous solutions of low concentration of the non-ionic surfactant triton x-100 into calcium fluoride porous medium. *J. Colloid Interface Sci.*, 295:578–582, 2006.
- [101] T.T. Lamminmäki, J.P. Kettle, and P.A.C. Gane. Absorption and adsorption of dye-based inkjet inks by coating layer components and the implications for print quality. *Colloids Surfaces A Physicochem. Eng. Asp.*, 380:79–88, 2011.
- [102] N. N. Lebedev. *Special functions and their applications*. Dover Publications, New York, 1972.
- [103] A.F.M. Leenaars, J.A.M. Huethorst, and J.J. van Oekel. Marangoni drying: a new extremely clean drying process. *Langmuir*, 6:1701–1703, 1990.
- [104] R. Levy and M. Shearer. Comparison of two dynamic contact line models for driven thin liquid films. *J. Eng. Math.*, 15:625–642, 2004.
- [105] Y. Li, C. Diddens, P. Lv, H.M.A. Wijshoff, M. Versluis, and D. Lohse. Gravitational effect in evaporating binary microdroplets. *Phys. Rev. Lett.*, 122:114501, 2019.
- [106] Y. Li, C. Diddens, T. Segers, H.M.A. Wijshoff, M. Versluis, and D. Lohse. Evaporating droplets on oil-wetted surfaces: Suppression of the coffee-stain effect. *PNAS*, 117:16756–16763, 2020.
- [107] A. Liemert. Explicit solution for the electrostatic potential of the conducting double sphere. *J. Appl. Phys.*, 115:164907, 2014.
- [108] J.C. Loudet, A.M. Alsayed, J. Zhang, and A.G. Yodh. Capillary interactions between anisotropic colloidal particles. *Phys. Rev. Lett.*, 94:018301, 2005.
- [109] J.C. Loudet, A.G. Yodh, and B. Pouligny. Wetting and contact lines of micrometer-sized ellipsoids. *Phys. Rev. Lett.*, 97:018304, 2006.
- [110] J. Lowndes. The numerical simulation of the steady movement of a fluid meniscus in a capillary tube. *J. Fluid Mech.*, 101:631–646, 1980.
- [111] B. Madivala, J. Fransaer, and J. Vermant. Self-assembly and rheology of ellipsoidal particles at interfaces. *Langmuir*, 25:2718–2728, 2009.
- [112] M. Majumder, C.S. Rendall, J.A. Eukel, J.Y.L. Wang, N. Behabtu, C.L. Pint, T. Liu, A.W. Orbaek, F. Mirri, J. Nam, A.R. Barron, R.H. Hauge, H.K. Schmidt, and M. Pasquali. Overcoming the ‘coffee-stain’ effect by compositional marangoni-flow-assisted drop-drying. *J. Phys. Chem. B*, 116:6536–6542,

2012.

- [113] X. Man and M. Doi. Ring to mountain transition in deposition pattern of drying droplets. *Phys. Rev. Lett.*, 116:066101, 2016.
- [114] A. Marin, H. Gelderblom, D. Lohse, and J.H. Snoeijer. Rush-hour in evaporating coffee drops. *Phys. Fluids*, 23:1111, 2011.
- [115] A. Marin, R. Liepelt, M. Rossi, and C.J. Kähler. Surfactant-driven flow transitions in evaporating droplets. *Soft Matter*, 12:1593–1600, 2016.
- [116] G. Martic, F. Gentner, D. Seveno, D. Coulon, J. De Coninck, and T.D. Blake. A molecular dynamics simulation of capillary imbibition. *Langmuir*, 18:7971–7976, 2002.
- [117] E. Marusic-Paloka, I. Pazanin, and S. Marusic. Comparison between darcy and brinkman laws in a fracture. *Appl. Math. Comput.*, 218:7538–7545, 2012.
- [118] R. Masoodi and K.M. Pillai. Darcy’s law-based model for wicking in paper-like swelling porous media. *AIChE Journal*, 56:2257–2267, 2010.
- [119] R. Masoodi, H. Tan, and K.M. Pillai. Darcy’s law-based numerical simulation for modeling 3d liquid absorption into porous wicks. *AIChE Journal*, 57:1132–1143, 2011.
- [120] R. Masoodi, H. Tan, and K.M. Pillai. Numerical simulation of liquid absorption in paper-like swelling porous media. *AIChE Journal*, 58:2536–2544, 2011.
- [121] A. Mazouchi and G. M. Homsy. Free surface stokes flow over topography. *Phys. Fluids*, 13:2751, 2001.
- [122] S. Mishra, K.L.Barton, A.G. Alleyne, P.M. Ferreira, and J.A. Rogers. High-speed and drop-on-demand printing with a pulsed electrohydrodynamic jet. *J. Microtech. Microeng.*, 20:095026, 2010.
- [123] M. Mohajeri, M. Hemmati, and A.S. Shekarabi. An experimental study on using a nanosurfactant in an eor process of heavy oil in a fractured micromodel. *J. Petrol. Sci. Eng.*, 126:162–173, 2015.
- [124] C.L. Moraila-Martínez, F.J.M. Ruiz-Cabello, M.A. Cabrerizo-Vílchez, and M.A. Rodríguez-Valverde. The effect of contact line dynamics and drop formation on measured values of receding contact angle at very low capillary numbers. *Colloids Surf.*, 404:63–69, 2012.
- [125] C.L. Moraila-Martínez, M.A. Cabrerizo-Vílchez, and M.A. Rodríguez-Valverde. The role of the electrostatic double layer interactions in the formation of nanoparticle ring-like deposits at driven receding contact lines. *Soft Matter*, 90:1664–1673, 2013.
- [126] Y. Moroi, M. Rusdi, and I. Kubo. Difference in surface properties between insoluble monolayer and adsorbed film from kinetics of water evaporation and bam image. *J. Phys. Chem. B*, 108:6351–6358, 2004.
- [127] P. Mukerjee and K.J. Mysels. Critical micelle concentration of aqueous surfac-

-
- tant systems. Technical report, Natl. Stand. Ref. Data. Ser., Natl. Bur. Stand., Washington, DC, 1971.
- [128] N. Murisic and L. Kondic. On evaporation of sessile drops with moving contact lines. *J. Fluid Mech.*, 679:219–246, 2011.
- [129] S. Najimi, I. Nowrouzi, A.K. Manshad, and A.H. Mohammadi. Experimental study of the performances of commercial surfactants in reducing interfacial tension and wettability alteration in the process of chemical water injection into carbonate reservoirs. *J. Pet. Explor. Prod. Technol.*, 10:1551–1563, 2020.
- [130] A. Nees. Experimentelle untersuchung des eindringverhaltens von fluessigkeit in poroese medien durch tropfenaufprall. Master’s thesis, Darmstadt University of Technology, Darmstadt, Germany, 2011.
- [131] T.A.H. Nguyen, A.V. Nguyen, M.A. Hampton, Z.P. Xu, L. Huang, and V. Rudolph. Theoretical and experimental analysis of droplet evaporation on solid surfaces. *Chem. Eng. Sci.*, 69:522–529, 2012.
- [132] D. Noguera-Marín, C.L. Moraila-Martínez, M.A. Cabrerizo-Vílchez, and M.A. Rodríguez-Valverde. The role of the electrostatic double layer interactions in the formation of nanoparticle ring-like deposits at driven receding contact lines. *Soft Matter*, 11:987–993, 2015.
- [133] B.A. Noskov. Kinetics of adsorption from micellar solutions. *Adv. Colloid Interface Sci.*, 95:237–293, 2002.
- [134] E. Nourafkan, Z. Hu, and D. Wen. Nanoparticle-enabled delivery of surfactants in porous media. *J. Colloid Interface Sci.*, 519:44–57, 2018.
- [135] D. Orejon, K. Sefiane, and M. Shanahan. Stick–slip of evaporating droplets: substrate hydrophobicity and nanoparticle concentration. *Langmuir*, 27:12834–12843, 2011.
- [136] A. Oron and S.G. Bankoff. Long-scale evolution of thin liquid films. *Rev. Mod. Phys.*, 69:931–980, 1997.
- [137] R. Pandit, M. Schick, and M. Wortis. Systematics of multilayer adsorption phenomena on attractive substrates. *Phys. Rev. B*, 26:5112–5140, 1982.
- [138] J. Park and J. Moon. Control of colloidal particle deposit patterns within picoliter droplets ejected by ink-jet printing. *Langmuir*, 22:3506–3513, 2006.
- [139] A. Pereira and S. Kalliadasis. On the transport equation for an interfacial quantity. *Eur. Phys. J. Appl. Phys.*, 44:211–214, 2008.
- [140] M.C. Pirrung. How to make a dna chip. *Angew. Chem., Int. Ed.*, 41:1276–1289, 2002.
- [141] M.N. Popescu, G. Oshanin, S. Dietrich, and A. Cazabat. Precursor films in wetting phenomenon. *J. Phys.: Condens. Matter*, 24:243103, 2012.
- [142] Y.O. Popov. Evaporative deposition patterns: Spatial dimensions of the deposit. *Phys. Rev. E*, 71:036313, 2005.
-

-
- [143] E.N. Lightfoot R. Bird, W.E. Stewart. *Transport Phenomena*. J. Wiley, 2007.
- [144] N.C. Reis, R.F. Griffiths, and J.M. Santos. Numerical simulation of the impact of liquid droplets on porous surfaces. *J. Comput. Phys.*, 198:747–770, 2004.
- [145] N.C. Reis, R.F. Griffiths, and J.M. Santos. Parametric study of liquid droplets impinging on porous surfaces. *Appl. Math. Model.*, 32:341–361, 2008.
- [146] O. Reynolds. On the theory of lubrication and its application to mr. beauchamp tower’s experiments, including an experimental determination of the viscosity of olive oil. *Philos. Trans. R. Soc. London*, 157:177, 1886.
- [147] E. Roumpea, N.M. Kovalchuk, M. Chinaud, E. Nowak, M.J.H. Simmons, and P. Angeli. Experimental studies on droplet formation in a flow-focusing microchannel in the presence of surfactants. *Chem. Eng. Sci.*, 195:507–518, 2019.
- [148] P. Sáenz, K. Sefiane, J. Kim, O. Matar, and P. Valluri. Evaporation of sessile drops: a three-dimensional approach. *J. Fluid Mech.*, 772:705–739, 2015.
- [149] A.G. Salinger, R. Aris, and J.J. Derby. Finite element formulations for large-scale coupled flows in adjacent porous and open fluid domains. *Int. J. Numer. Meth. Fluids*, 18:1185–1209, 1994.
- [150] R. Savino, D. Paterna, and N. Favaloro. Buoyancy and marangoni effects in an evaporating drop. *J. Thermophys. Heat Transfer*, 16:562–574, 2002.
- [151] N. Savva and S. Kalliadasis. Dynamics of moving contact lines: A comparison between slip and precursor film models. *EPL*, 94:64004, 2011.
- [152] L.W. Schwarts and R.R. Eley. Simulation of droplet motion on low-energy and heterogeneous surfaces. *J. Colloid Interface Sci.*, 202:1730–188, 1998.
- [153] L.E. Scriven and C.V. Sternling. The marangoni effects. *Nature*, 187:186–188, 1960.
- [154] K. Sefiane. The coupling between evaporation and adsorbed surfactant accumulation and its effect on the wetting and spreading behaviour of volatile drops on a hot surface. *J. Petrol. Sci. Eng.*, 51:238–252, 2006.
- [155] S. Semenov, V.M. Starov, R.G. Rubio, H. Agogo, and M.G. Velarde. Evaporation of sessile water droplets: Universal behaviour in presence of contact angle hysteresis. *Colloids Surf. A*, 391:135–144, 2011.
- [156] S. Semenov, A. Trybala, H. Agogo, N. Kovalchuk, F. Ortega, R.G. Rubio, V.M. Starov, and M.G. Velarde. Evaporation of droplets of surfactant solutions. *Langmuir*, 29:10028–10036, 2013.
- [157] W. Sempels, R. de Dier, H. Mizuno, J. Hofkens, and J. Vermant. Auto-production of biosurfactants reverses the coffee ring effect in a bacterial system. *Nat Commun*, 4:1757, 2013.
- [158] M.E.R. Shanahan. Simple theory of “stick-slip” wetting hysteresis. *Langmuir*, 11:1041–1043, 1995.
- [159] Y. Shapira. *Matrix-based Multigrid Theory and Applications*. Springer, New York,
-

2008.

- [160] A. Sheludko. Thin liquid films. *Adv. Colloid Interface Sci.*, 1:391–464, 1967.
- [161] W. Shi, K. Tang, J. Ma, Y. Jia, H. Li, and L. Feng. Marangoni convection instability in a sessile droplet with low volatility on heated substrate. *Int. J. Heat Mass Transfer*, 117:274–286, 2017.
- [162] D.N. Sibley, A. Nold, N. Savva, and S. Kalliadasis. A comparison of slip, disjoining pressure, and interface formation models for contact line motion through asymptotic analysis of thin two-dimensional droplet spreading. *J. Eng. Math.*, 94:19–41, 2015.
- [163] M. Singh, H.M. Haverinen, P. Dhagat, and G.E. Jabbour. Inkjet printing-process and its applications. *Adv. Mater.*, 22:673–685, 2010.
- [164] D.P. Siregar. *Numerical simulation of evaporation and absorption of inkjet printed droplets*. PhD thesis, Eindhoven University of Technology, Eindhoven, the Netherlands, 2012.
- [165] D.P. Siregar, J.G.M. Kuerten, and C.W.M. van der Geld. Numerical simulation of the drying of inkjet-printed droplets. *J. Colloid Interface Sci.*, 392:388–395, 2013.
- [166] M.K. Smith. Thermocapillary migration of a two-dimensional liquid droplet on a solid surface. *J. Fluid Mech.*, 294:209–230, 1995.
- [167] J.H. Snoeijer, E. Rio, N.L. Grand, and L. Limat. Self-similar flow and contact line geometry at the rear of cornered drops. *Phys. Fluids*, 17:072101, 2005.
- [168] J.H. Snoeijer and B. Andreotti. Moving contact lines: Scales, regimes and dynamical transitions. *Annu. Rev. Fluid Mech.*, 45:269–292, 2013.
- [169] V.M. Starov, S.A. Zhdanov, and M.G. Velarde. Capillary imbibition of surfactant solutions in porous media and thin capillaries: partial wetting case. *J. Colloid Interface Sci.*, 273:589–595, 2004.
- [170] V.M. Starov, M.G. Velarde, and C.J. Radke. *Wetting and Spreading Dynamics*. Taylor and Francis/CRC, New York, 2007.
- [171] V.M. Starov and M.G. Velarde. Surface forces and wetting phenomena. *J. Phys.: Condens. Matter*, 21(46):464121, 2009.
- [172] T. Still, P.J. Yunker, and A.G. Yodh. Surfactant-induced marangoni eddies alter the coffee-rings of evaporating colloidal drops. *Langmuir*, 28(11):4984–4988, 2012.
- [173] H.A. Stone. A simple derivation of the time-dependent convective-diffusion equation for surfactant transport along a deforming interface. *Phys. Fluids*, 2:111, 1990.
- [174] B.A. Suleimanov, F.S. Ismailov, and E.F. Veliyev. Nanofluid for enhanced oil recovery. *J. Petrol. Sci. Eng.*, 78:431–437, 2011.
- [175] S. Supple and N. Quirke. Molecular dynamics of transient oil flows in-

-
- nanopores i: Imbibition speeds for single wallcarbon nanotubes. *J. Chem. Phys.*, 121:8571–8579, 2004.
- [176] S. Supple and N. Quirke. Molecular dynamics of transient oil flows in nanopores. ii. density profiles and molecular structure for decane in carbon nanotubes. *J. Chem. Phys.*, 122:104706, 2005.
- [177] H. Tan, C. Diddens, P. Lv, J.G.M. Kuerten, X. Zhang, and D. Lohse. Evaporation-triggered microdroplet nucleation and the four life phases of an evaporating ouzo drop. *Proc. Natl. Acad. Sci. U.S.A.*, 113:8642–8647, 2016.
- [178] U. Thiele, A.J. Archer, and M. Plapp. Thermodynamically consistent description of the hydrodynamics of free surfaces covered by insoluble surfactants of high concentration. *Phys. Fluids*, 24:102107, 2012.
- [179] U. Thiele, A.J. Archer, and M. Plapp. Gradient dynamics models for liquid films with soluble surfactant. *Phys. Rev. Fluids*, 1:083903, 2016.
- [180] U. Thiele, J.H. Snoeijer, S. Trinschek, and K. John. Equilibrium contact angle and adsorption layer properties with surfactants. *Langmuir*, 34:7210–7221, 2018.
- [181] J. Tian and W.D. Philpot. Relationship between surface soil water content, evaporation rate, and water absorption band depths in swir reflectance spectra. *Remote Sens. Environ.*, 169:280–289, 2015.
- [182] M. Tomoaia-Cotișel, J. Zsakó, A. Mocanu, M. Lupea, and E. Chifu. Insoluble mixed monolayers: iii. the ionization characteristics of some fatty acids at the air/water interface. *J. Colloid Interface Sci.*, 117:464–476, 1987.
- [183] V.N. Truskett and K.J. Stebe. Influence of surfactants on an evaporating drop: Fluorescence images and particle deposition patterns. *Langmuir*, 19:8271–8279, 2003.
- [184] N.R. Tummala, L. Shi, and A. Striolo. Molecular dynamics simulations of surfactants at the silica–water interface: Anionic vs nonionic headgroups. *J. Colloid Interface Sci.*, 362:135–143, 2011.
- [185] H.A.E. Benson V. Sarveiya, S. Risk. Liquid chromatographic assay for common sunscreen agents: application to in vivo assessment of skin penetration and systemic absorption in human volunteers. *J. Chromatogr. B*, 803:225–231, 2004.
- [186] F. Wang and H. Wu. Molecular origin of contact line stick-slip motion during droplet evaporation. *Sci Rep*, 5:17521, 2015.
- [187] Z. Wang, Y. Chen, X. Sun, R. Duddu, and S. Lin. Mechanism of pore wetting in membrane distillation with alcohol vs. surfactant. *J. Membr. Sci.*, 559:183–195, 2018.
- [188] D.E. Weidner. The effect of surfactant convection and diffusion on the evolution of an axisymmetric pendant droplet. *Phys. Fluids*, 24:062104, 2012.
- [189] H. Wong, D. Rumschitzki, and C. Maldarelli. On the surfactant mass balance at a deforming fluid interface. *Phys. Fluids*, 8:3203, 1996.
-

-
- [190] L. Xu, H. Zhu, H.E. Ozkan, and H.W. Thistle. Evaporation rate and development of wetted area of water droplets with and without surfactant at different locations on waxy leaf surfaces. *Biosystems Engineering*, 106:58–67, 2010.
- [191] L.Y. Yeo, O.K. Matar, E.S. Perez de Ortiz, and G.F. Hewitt. Film drainage between two surfactant-coated drops colliding at constant approach velocity. *J. Colloid Interface Sci.*, 257:93–107, 2003.
- [192] X. Yin and S. Kumar. Two-dimensional simulations of flow near a cavity and a flexible solid boundary. *Phys. Fluids*, 18:063103, 2006.
- [193] H. Yu, G. Son, and W. Shim. Numerical simulation of droplet merging and chemical reaction in a porous medium. *Int. Commun. Heat Mass Transfer*, 89:154–164, 2017.
- [194] P. Yunker, T. Still, and M. Lohr. Suppression of the coffee-ring effect by shape-dependent capillary interactions. *Nature*, 476:308–311, 2011.
- [195] D. Zhang, Y. Xie, M.F. Mrozek, C. Ortiz, V.J. Davisson, and D. Ben-Amotz. Raman detection of proteomic analytes. *Anal. Chem.*, 75:5703–5709, 2003.
- [196] S.A. Zhdanov, V.M. Starov, V.D. Sobolev, and M.G. Velarde. Spreading of aqueous sds solutions over nitrocellulose membranes. *J. Colloid Interface Sci.*, 264:589–595, 2003.

Acknowledgements

Although a PhD project may seem a solitary activity, I can tell from experience that it definitely is not. This thesis is not something that has been created in isolation and many people have been involved either directly or indirectly.

First of all, I would like to thank Hans Kuerten. When you asked me for this project five years ago, I had not even considered doing a PhD. I am really thankful you put me on this path. It is a determining factor of who I am today. Also thank you for all your help during my project. Your patience is unlimited, you always gave great suggestions and insights and you believed in me, occasionally more than I did myself. Although I encountered tough problems during my work, I never felt like I was truly stuck because of your input. It is still a mystery to me how you almost instantaneously responded to emails and always had time for me, while at the same time having so many responsibilities and tasks.

I would also like to express my gratitude towards Christian Diddens. Especially at the start of my project your help was invaluable when I was still figuring out the brilliant numerical program you largely created. Also, later on we had several technical discussions which were really helpful in my work. I am truly amazed by your expertise in modeling physical problems and programming numerical code.

Another thanks goes to Herman Wijshoff. You gave useful, critical feedback on my manuscripts and your connection with industry was of great value. It was always a joy hearing you talk about the newest developments and insights regarding inkjet printing. It is of no surprise to me that so many students want to do their internship or graduation project at Canon in Venlo.

I am also grateful for the other committee members: Federico Toschi, Jacco Snoeijer, Doris Vollmer and Harald van Brummelen. Thank you for critically examining my research. Quality is of utmost importance and your work is therefore crucial.

My gratitude also goes out to my colleagues of the Power and Flow group. First of all, thank you Rahul for all the nice coffee breaks in which we had all kinds of philosophical and societal discussions. It is great how we solved all world problems, when we were not talking about games ;-). I specifically want to thank Giel Priems for introducing me to our group and answering all kinds of practical questions when I started my PhD. Also a big thanks to all of my other office mates, including but not limited to, Haiyu, Yu, Faeze, Nicole and Nick. You most definitely made my time at the TU/e more fun than it otherwise would have been. Also thank you Conrad for the nice coffee breaks and the discussions about our projects.

Another big thanks to Marjan for all practical help, funny conversations and witty comments. Your importance to the Power and Flow group can hardly be overstated.

I also want to thank my fellow participants of the FIP program. Thanks for the collaboration and the mutual exchange of ideas and knowledge. It has been an honor being part of this program and together we built up an extensive knowledge base. I specifically want to mention Tristan and Tom here. It was nice hearing from you at

the biweekly meetings and you taught me interesting things about diffusive interface methods.

I am also grateful for all students I had the pleasure to supervise during their final projects. It was an honor being part of these milestones in your education and I learned things from all of you. I especially want to thank Mirthe for her contribution to my research during her graduation project. Although at the time I am writing this you are not even halfway through your project, you already gave valuable insights, including some clarity on the mysterious Brinkman equation.

My gratitude also goes out to Sander, Elbert and Mark for all the nice coffee breaks and for working together. You are great friends and meeting you was always fun and refreshing. Elbert, I am glad we share the same weird taste in music, which makes working with you a true joy. Besides you three, I also want to thank Bob, Martijn, Peter, David, Brandon, Mark de Boer, Evie, Ivar, Karel and Bo for all game nights, D&D sessions and more. After a day of hard work, it always is a real pleasure meeting you and spending time together.

Another person I would like to thank is Egbert. You did a tremendous job designing the cover of my thesis, something which I could never have done myself with such skill. I am really glad with the result.

I also want to thank my parents for always supporting me and playing such an important role in forming me into the person I am today. Without you, I never would have gotten to this point.

Last, but definitely not least, I want to thank Ymke, my wife, for your unyielding support and for always encouraging me. I find it amazing how you always wanted to know what I was working on, despite how unintelligible my explanations were. You were there for me during hard times and you celebrated with me when I had a breakthrough. Also thank you for being the mother of our daughter, Tamar. Whenever I am unsure why I am doing this work, I just have to look at her to remember why.

Curriculum Vitae

Ruben van Gaalen was born on 16 August 1994 in Bussum, the Netherlands. From 2006 to 2008 he went to secondary school at Goois Lyceum in Bussum (VWO/gymnasium) and from 2008 to 2012 at Arcus in Lelystad (VWO/gymnasium).

In 2015 he obtained his Bachelor of Science degree in Mechanical Engineering at Eindhoven University of Technology with the predicate 'great appreciation'. His bachelor thesis entitled '*Modelling temperature differences during irreversible electroporation using Greens' functions*', became the basis for a publication.



In 2016, as part of his master program he interned at Technion in Haifa, Israel where he performed experiments regarding vortex-induced vibrations. After finishing his master thesis '*Characterization of fluid dynamics in an expandable bioreactor*' in 2017 he obtained the Master of Science degree in Mechanical Engineering at Eindhoven University of Technology with the predicate 'great appreciation'.

That same year he started his PhD track, also at the Department of Mechanical Engineering of Eindhoven University of Technology. Besides carrying out the research for this thesis, he also performed several extra educational tasks. This included the coordination of a course and the development of databases of test questions and corresponding intermediate tests for two courses.

List of Publications & Conference contributions

Publications

1. R.T. van Gaalen, C. Diddens, H.M.A. Wijshoff, J.G.M. Kuerten, The evaporation of surfactant-laden droplets: a comparison between contact line models, *J. Colloid Interface Sci.* 579 (2020) 888-897, <https://doi.org/10.1016/j.jcis.2020.06.099>.
2. R.T. van Gaalen, C. Diddens, H.M.A. Wijshoff, J.G.M. Kuerten, Marangoni circulation in evaporating droplets in the presence of soluble surfactants, *J. Colloid Interface Sci.* 584 (2021) 622-633, <https://doi.org/10.1016/j.jcis.2020.10.057>.
3. R.T. van Gaalen, C. Diddens, D.P. Siregar, H.M.A. Wijshoff, J.G.M. Kuerten, Absorption of surfactant-laden droplets into porous media: a numerical study, *J. Colloid Interface Sci.* 597 (2021) 149-159, <https://doi.org/10.1016/j.jcis.2021.03.119>.

Conference contributions

1. R.T. van Gaalen, C. Diddens, D.P. Siregar, H.M.A. Wijshoff, J.G.M. Kuerten, Absorption of surfactant-laden droplets into porous media, *Droplets 2021*, Darmstadt, Germany.
2. R.T. van Gaalen, C. Diddens, H.M.A. Wijshoff, J.G.M. Kuerten, The effect of a precursor film on evaporating inkjet droplets with surfactants, *Droplets 2019*, Durham, United Kingdom.
3. R.T. van Gaalen, C. Diddens, H.M.A. Wijshoff, J.G.M. Kuerten, Drying droplets and surfactants: a numerical study, *Burgers Symposium 2019*, Lunteren, the Netherlands.